HYBRID POLYMERIC/CERAMIC MEMBRANE FOR OXY-FUEL COMBUSTION APPLICATIONS

BY

Dia' Al-deen O. Afaneh

A Thesis Presented to the
DEANSHIP OF GRADUATE STUDIES

KING FAHD UNIVERSITY OF PETROLEUM & MINERALS

DHAHRAN, SAUDI ARABIA

In Partial Fulfillment of the
Requirements for the Degree of

MASTER OF SCIENCE

In

MECHANICAL ENGINEERING

January 2017

KING FAHD UNIVERSITY OF PETROLEUM & MINERALS

DHAHRAN- 31261, SAUDI ARABIA

DEANSHIP OF GRADUATE STUDIES

This thesis, written by **Dia' Al-deen O. Afaneh** under the direction his thesis advisor and approved by his thesis committee, has been presented and accepted by the Dean of Graduate Studies, in partial fulfillment of the requirements for the degree of **MASTER OF SCIENCE IN MECHANICAL ENGINEERING.**

Med Habib 16/1/2017

Dr. Mohamed A Habib
(Advisor)

Dr. Medhat Nemitallah
(Member)

Dr. Khaled Mezghani
(Member)

Dr. Zuhair Mattoug Gasem
Department Chairman

Dr. Salam A. Zummo
Dean of Graduate Studies

22/1/17

Date

Dedicated

To

My Beloved Parents

ACKNOWLEDGMENTS

All approbations and adorations are due to Almighty Allah, who, in His infinite mercy has made it possible for me to go this far in life. I thank Him for making it possible to conclude my Masters in King Fahd University of Petroleum and Minerals, Saudi Arabia successfully.

I acknowledge, with deep gratitude and appreciation, the inspiration, encouragement, valuable time and continuous guidance given to me by my thesis advisor, Dr. Mohamed A. Habib. I am also highly grateful to my Committee members, Dr. Medhat Nemitallah, and Dr. Khaled Mezghani, for their valuable guidance and support.

My heartfelt thanks are due to my parents, brothers, and sister for their prayers, guidance, and moral support throughout my academic life. My parents' advice, to strive for excellence has made all this work possible.

After that, acknowledgment is due to KFUPM for granting me the opportunity to pursue graduate studies and for the support extended towards my research through its remarkable facilities. Finally, special thanks are due to all friends and professors who made my study's life beautiful and comfortable.

TABLE OF CONTENTS

LIST OF TABLES

LIST OF FIGURES

ABSTRACT

Full Name : [Dia' Al-deen Omar Odeh Afaneh]

Thesis Title : [HYBRID POLYMERIC/CERAMIC MEMBRANE FOR OXY-FUEL COMBUSTION APPLICATIONS]

Major Field : [Mechanical Engineering]

Date of Degree : [January 2017]

The present work aims at developing a hybrid polymeric/ceramic membrane unit to produce high oxygen permeation flux for oxy-fuel combustion applications. The current research involves numerical investigation of air separation by polymeric membranes to produce oxygen enriched air. Polymeric membrane air separation is studied separately, to investigate the effect of several operating parameters on the air separation process.

A detailed numerical study is presented for air separation using different polymers. Effects of sweep gas flow rate, feed gas flow rate, fed pressure, and membrane polymeric material (considering TR-PBO-co-PPL-28 and TR-PI-g-CD) on permeation fluxes and concentrations of O_2 and N_2 are investigated. Targeting higher exit O_2 concentrations, multi-stage air separation polymeric membrane unit is developed. The developed unit consists of three stages and the achieved oxygen mass fraction at the stage outlet of first, second and third stages are 0.517, 0.8 and 0.914. Higher stage cut ratio is gained in the third stage as compared to first and second stages.

Ceramic oxygen transport membrane (OTM) is integrated numerically with the polymeric membrane to form a hybrid polymeric/ceramic membrane unit for oxy-fuel combustion. Oxygen enriched air out of the polymeric membrane unit is fed to a ceramic membrane oxy-fuel based reactor. Detailed numerical study of oxy-fuel combustion in a tubular Oxygen Transport Reactor (OTR) fed by oxygen enriched air. CH_4/CO_2 mixture with various concentrations is swept inside the tubular OTR, where CO_2 serves as a diluent. The model was utilized to investigate the effects of sweep gas flow rate, feed gas flow rate, fed O_2 mass fraction, and swept CH_4 mass fraction on permeation fluxes and combustion process. It is observed that stoichiometric combustion could be achieved by feeding a specific feed flow rate.

Energy and design analysis of the hybrid unit are conducted, the ratio between the required fiber polymer membranes area to the Oxygen Transport Membranes (OTM) area is investigated as a function of the sweep flow rate. The output power of the hybrid unit is calculated and compared with the air fed OTR unit, 38.57 W power output is produced from one OTM shell hybrid unit. Higher power outputs are achieved by the hybrid unit comparing to the air fed unit. FLUENT CFD software is used to conduct the numerical simulation and calculations compiled with user defined functions (UDFs) that solve for oxygen and nitrogen permeation across the membranes.

ملخص الرسالة

الاسم الكامل: ضياء الدين عمر عوده عفانه

عنوان الرسالة: استخدام اغشية سيراميكية / بلومارية هجينة في تطبيقات احتراق الأكسو وقود

التخصص: الهندسة الميكانيكة

تاريخ الدرجة العلمية: ربيع الثاني 1438

الهدف الرئيسي من هذه الأطروحة هو تطوير وحدة هجينة من الاغشية السيراميكية والبلومارية للاستخدام في فصل مكونات الهواء بتدفق اكسجين عالي لتطبيقات الأكسو وقود. هذا البحث يشمل محاكاة فصل مكونات الهواء بالأغشية البلومارية لإنتاج هواء غني بالأكسجين. تم دراسة فصل مكونات الهواء بالأغشية البلومارية بشكل منفصل، لتقصي تأثير عوامل متعددة على عملية فصل مكونات الهواء.

تم استخدام نوعيات متعددة من الاغشية البلومارية في محاكاة فصل مكونات الهواء. تأثير تدفق الغازات المغذية والمزيلة تمام دراسته، بالإضافة الى تأثير الضغط المغذي ونوعية المادة البلومارية على تدفق غازات الاكسجين والنيتروجين وتركيزها. بهدف الحصول على تركيز عالي للأكسجين، وحدة متعددة المراحل لفصل مكونات الهواء قد طورت. الوحدة المطورة تتكون من ثلاث مراحل، وتركيز الاكسجين المكتسب في مخارج هذه المراحل هو 0.517 و 0.80 و0.914 على التوالي. نسبة اعلى من (θ) تم اكتسابها في المرحلة الثالثة مقارنة بالمرحلتين الأولى والثانية.

تم دمج غشاء سيراميكي ناقل للأكسجين مع الغشاء البلوماري بشكل رقمي لتشكيل الوحدة الهجينة لاستخدامها في تطبيقات الأكسو وقود. الهواء الغني بالأكسجين والناتج عن الاغشية البلومارية تم استخدامه لتغذية مفاعل نقل الاكسجين (OTR) تم دراسة احتراق الأكسو وقود داخل ال (OTR) الأنبوبي المغذى بالهواء الغني بالأكسجين بشكل رقمي. تم استخدام خليط من غاز ثاني أكسيد الكربون والميثان في منطقة الازالة داخل ال(OTR) بتراكيز

مختلفة، حيث يخدم غاز ثاني أكسيد الكربون كملطف لعملية الاحتراق. تم دراسة تأثير تدفق الغازات المغذية والمزيلة وتركيزاتها في نموذج ال (OTR) على تدفق غاز الاكسجين وتركيزه وعلى عملية الاحتراق.

تم اجراء تحليلات للطاقة والتصميم للوحدة الهجينة، حيث تم حساب نسبة المساحة بين الأغشية البلومارية والسيراميكية كمتغير مع تدفق الغاز المزيل. تم حساب الطاقة الناتجة عن الوحدة الهجينة ومقارنتها مع الطاقة الناتجة من وحدة مغذية بالهواء، حيث تم توليد طاقة مقدارها 38.57 واط من الوحدة الهجينة المقترحة الواحدة. اظهرت النتائج ان الطاقة الناتجة من الوحدة الهجينة اعلى من الطاقة الناتجة من الوحدة المغذية بالهواء. استخدم برنامج FLUENT للقيام بعملية المحاكاة الرقمية وتم جمعه مع UDF لحل معادلات تدفق الغازات من خلال الاغشية.

CHAPTER 1

INTRODUCTION

1.1 Carbon Capture

Fossil fuels are the dominant source of the global primary energy demand, and will likely remain so for the next decades. Carbon capture is essential to enable the use of fossil fuels while reducing CO_2 emissions into the atmosphere, and thereby mitigating global climate change. Carbon capture is generally grouped into three different strategies (Figure 1). These are post-combustion decarbonization (separation of CO_2 from exhaust gas), oxy-fuel combustion and pre-combustion decarbonization (production of carbon-free fuel).

Membrane gas separation technology can be applied in both post-combustion and oxy-combustion carbon capture technologies. In post-combustion technology, CO_2 is separated from the exhaust stream using membranes with different techniques [1], [2]. One of the most common techniques for CO_2 capture is the membrane gas absorption (MGA) technique. This technique combines between membrane separation and absorption methods to provide effective removal of CO_2 [3]. Oxy-fuel combustion requires separation of air to provide high concentrations of O_2. Due to the high cost of

combustion using pure oxygen, oxygen enriched air combustion became an acceptable approach for controlling emissions [4].

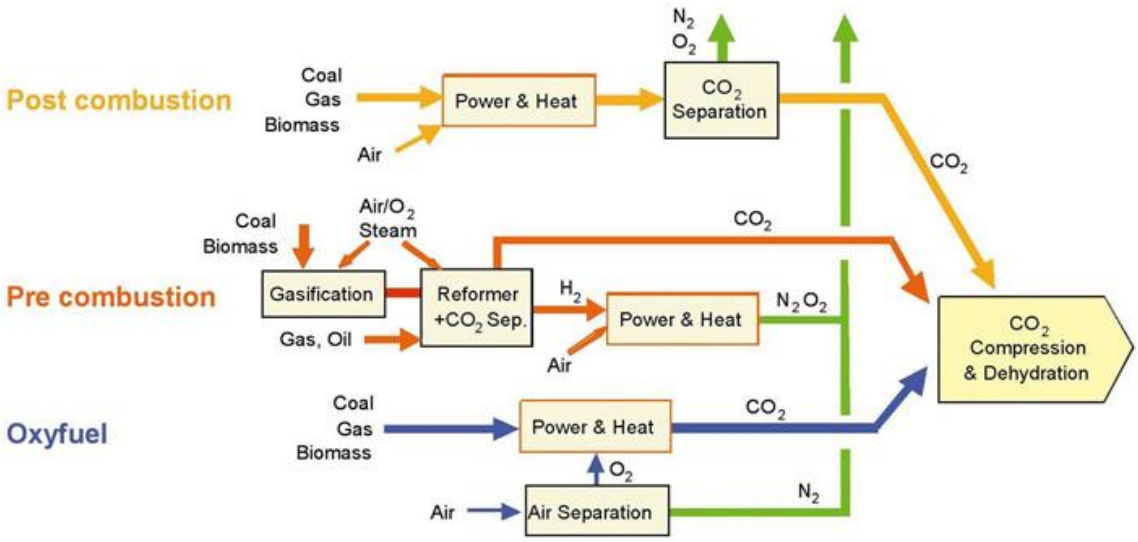

Figure 1: Carbon capture strategies [5].

1.2 Air Separation

Oxygen enriched air could be produced by three main air separation methods including; cryogenic distillation, pressure swing adsorption and membrane separation. Cryogenic distillation is the most common of these three technologies and produces high purities of oxygen (>99%) with large scale productions [6]. Pressure swing adsorption can reach up to 95% oxygen purities, but the requirement of solvents limits its size capacity, primarily due to capital costs [7], [8]. The third technology is the most recent of these three technologies, which is the membrane air separation technology through the use of high temperature ceramic ion transport membranes (ITMs) and polymeric membranes. ITMs can produce purities of close to 100% while polymeric membranes can produce different concentrations of oxygen enriched air [7].

1.3 Polymeric Membranes

In polymeric membrane gas separation, there is no need for thermal heating of the membrane or the involvement of any sorbents to separate a gas mixture, as in the cases of cryogenic distillation and adsorption. The main driving force in polymeric membrane air separation is the partial pressure gradient across the membrane. The permeability (P) of a polymeric membrane for a specific gas could be defined as follows [9]:

$$P = \frac{JL}{A(p' - p'')} \tag{1}$$

Where J is the permeation flux through the membrane for a specific gas, p′ and p″ are the gas partial pressure on the feed side and the permeate side, A is the membrane area, and L is the membrane thickness. The permeability coefficient is a specific property of a gas for a specific polymer. The present study aims at investigating the performance of polymeric membranes for oxygen enriched air combustion applications. Based on that, a polymer with high oxygen permeability and low nitrogen permeability is needed for such applications. The selectivity (α) is a commonly used parameter that characterizes the ability of a polymer to separate two gases, and it can be defined as follows:

$$\alpha_{a/b} = \frac{P_a}{P_b} \tag{2}$$

Where P_a and P_b are the permeability of the two gases, gas a and gas b. The permeability is a product of two coefficients; the solubility coefficient (S), which is the thermodynamic term, and the diffusion coefficient (D), the kinetic term. This relation can be written as follows [9]:

$$P=D*S \quad (3)$$

The values of these two terms (S and D) depend on the penetrant gas and the material of the membrane. These coefficients are also influenced by temperature, pressure, gas combustion and other parameters depending on the polymer and the penetrant gas. Park and Pual [10] predicted and reported a correlation to calculate the glassy polymers permeability using the fractional free volume (FFV), as following:

$$P = A\exp\left(\frac{-B}{FFV}\right) \quad (4)$$

Where, A and B are constants for a gas with specific conditions, and the fractional free volume (FFV) is defined by FFV= $(V-V_0)/V$, where V_0 is the dense volume and V is the measured volume. They determined the empirical factors of 105 different polymers database. However, this correlation still has a large degree of error, so the obtained experimental values of the permeability were used in the model.

A perfect polymer for air separation should have high oxygen permeability and high selectivity (α_{O_2/N_2}). However, there is a limitation getting such polymer with high selectivity and high permeability that is represented in the “upper bound” relationship for polymeric membrane separation of gases. This limit, a log-log plot of selectivity versus permeability of the more permeable gas, demonstrated that almost all the data points were below this line [11]. Figure 2 shows the revisited upper bound that was predicted by Robeson [12].

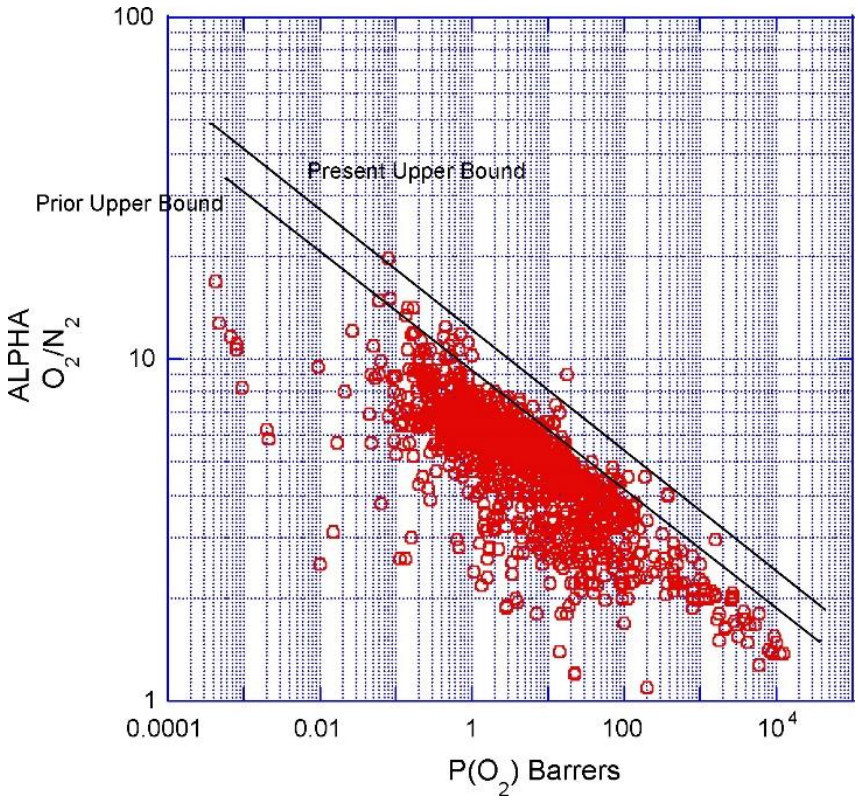

Figure 2: The upper bound for O_2/N_2 separation [12].

1.4 Ion Transport Membranes

Ceramic-ion transport membranes (ITM) technology allows for oxygen production with high purity through air separation at high temperature (more than 700^{o}C) and high pressure at low cost [13]. This impermeable ceramic membrane is an electron conducting material that ionizes the oxygen and allows it to penetrate to the permeate side; then, this ionized oxygen recombines as oxygen after relinquishing the electrons, as shown in Figure 3.

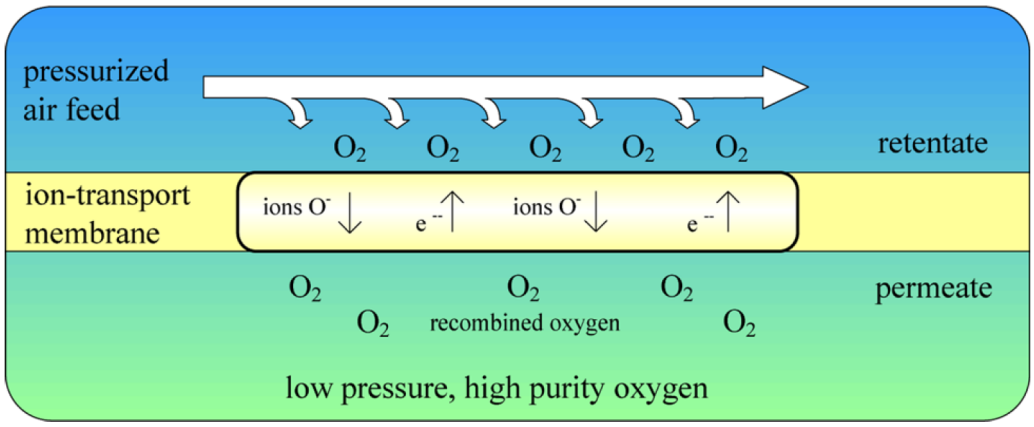

Figure 3: Mechanism of operation of an ITM membrane [13].

ITMs have high oxygen selectivity and permeability compared to polymeric membranes, but they only operate at high temperatures that can eliminate their utility for high temperature applications [14]. However, this is an excellent choice for an oxy-fuel combustion process, especially if it is used in the high temperature region near to the combustion, which will provide the required temperature for ITM air separation [15].

Like polymeric membranes, the O_2 partial pressure gradient is one of the driving forces for O_2 permeation through the ceramic membrane. Increasing the O_2 concentration on the feed side (oxygen enriched air) raises the partial pressure on the feed side, which consequently increases the permeation flux. Feeding oxygen enriched air to the ITM through polymeric membrane air separation unit is a perfect way to increase the permeation flux through the ITM [16]. Polymeric membranes can produce oxygen enriched air with more than 50% mole fraction, depending on the polymer type. Therefore, this thesis research aims at developing a hybrid polymeric/ceramic membrane unit for oxy-fuel combustion applications, where the oxygen enriched air will be fed to an oxygen transport reactor (OTR) from a polymeric membrane unit.

1.5 Objectives

The main objective of this research is to numerically develop a design for hybrid polymeric/ceramic membrane unit for air separation at high oxygen permeation flux for oxy-fuel combustion applications. The specific objectives are:

- To develop a numerical model for polymeric membrane gas separation and to study the effect of different parameters on the polymeric membrane air separation process.
- To study numerically the ion transport membrane air separation unit with oxygen enriched air in an oxy-fuel combustion reactor.
- To develop a numerical model for the hybrid system and to study the effect of different parameters on the oxygen permeation flux through the ITM.

CHAPTER 2

LITERATURE REVIEW

2.1 Oxy-Fuel Combustion Technology

Burning fuels in pure oxygen could enable the capture of carbon dioxide in the exhaust gases after H_2O condensation. Acquisition of pure O_2 with low cost is a critical issue in this process. Cryogenic distillation, the most conventional method of air separation, is an expensive method and can reduce the plant's efficiency [17]. Therefore, many research investigations were conducted to reduce the separation cost by using different techniques. Burdyny and Struchtrup [18] studied the air separation using a "hybrid membrane/cryogenic" system for small and medium oxy-fuel systems. They tested the potential to reduce the oxy-fuel process work by thermodynamic models, and they found that the process' efficiency can be improved by 0.9% in this hybrid system. Pfaff et al. [19] compared the impact of using cryogenic and ITM on the efficiency of coal-fired oxy-fuel steam power plant.

Several types of fuels were studied in the literature with oxy-fuel combustion. Yoruk et al. [20] investigated Estonian oil shale oxy-fuel combustion numerically. Gao et al. [21] studied lignite coal and microalgae oxy-fuel combustion and the emissions during this process. Niu et al. [22] evaluated and studied sewage sludge oxy-fuel combustion by a thermal analysis technique, while Anheden et al. [6] discussed the concepts of the oxy-

fuel combustion process and its applications. Chen et al. [23] reviewed and evaluated many experimental and numerical works of oxy-coal combustion technically. Habib et al. [24] examined the development of oxy-fuel power cycles, carbon capture potential, and ITM reactors.

Mardani et al. [25] investigated an oxy-fuel and moderate or intense low-oxygen dilution combustions combination numerically. They studied the reaction zone and the effect of different parameters. Bhuiyan et al. [26] conducted a numerical study of biomass co-firing with oxy-fuel combustion, and they highlighted the possible impacts of changing the combustion atmosphere and fuel ratio on the boiler performance. Adamczyk et al. [27] conducted air-fuel and oxy-fuel combustion 3D modeling of a circulating fluidized bed boiler; several parameters' influences were studied in this paper, including radiative heat transfer.

Various researchers have investigated the combustion behavior and characteristics of oxy-fuel flames. Kutne et al. [28] performed experiments to study the flame structure and stability of gas turbine oxy-fuel combustion, for equivalence ratio of 0.5 - 1.0 and oxygen at mole fractions of 20% - 40%, and powers of 10 - 30 kW. The authors pointed out that if the mole fraction of oxygen is less than 22%, the burner will be impossible to operate, as it will result in unstable operation and blow out even if the equivalence ratio is 1.0 and at powers of 20 and 30kW. The results of Nemitallah and Habib [29] also indicated extinction of the flame if the oxygen in the mixture is less than 21%. Hence, flame stability will only be possible if the mole fraction of oxygen is more than 21%. The authors also found that heat loss in the CH_4/ oxy-fuel combustion was more as compared to CH_4/air flames when operated in the same burner.

Oxy-fuel combustion will not be possible if oxygen, fuel, and diluent are not supplied properly [30]. Increase in the initial O_2 percentage of the oxidizer mixture (which implies a reduction in the concentration of CO_2) improves combustion stability, increases H_2O concentration of the exhaust gas [29]. Also, at a certain ratio of oxygen/diluent of oxyfuel combustion, flames will be stable and low emissions will be made [30].

The equivalence ratio on effect H_2O concentration and the oxidizers is very significant. The increasing of the equivalence ratio, while keeping the ratio of O_2/CO_2 and fuel volume flow rate constant, the concentration of H_2O increases, whereas the availability of oxygen is reduced [29]. The effects of pressure on the combustion products are also significant. At high pressure, it was realized that the CO emissions and O_2 level in the flue gases were higher than at lower pressure [30]. This emissions level is due to incomplete combustion, which also leads to lower combustion temperature.

2.2 Polymeric Membranes

Many research works were carried out to develop high performance gas separation polymeric membranes. One of the recently developed groups of membranes is the thermally rearranged (TR) polymeric membranes group by Park et al. [31]. These polymeric membranes have high selectivity and high permeability for different gases. Various studies were conducted to develop polymers from this family and to explore the gas separation process through this type of membranes [32, 33, 34, 35]. Sanders et al. [36] placed the TR polymers and other recent polymers in the upper bound in their review. As shown in Figure 4, TR polymers show the best permselectivity for O_2/N_2 separation.

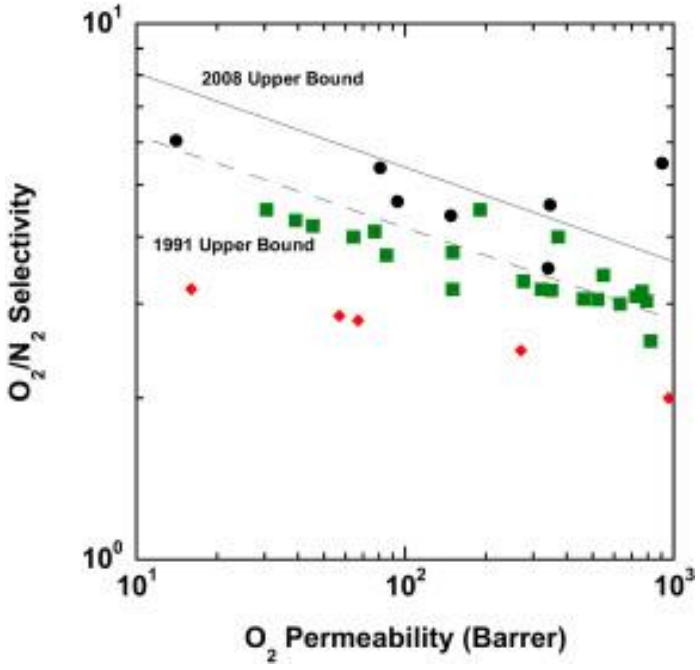

Figure 4: O_2/N_2 separation performance for some recent polymers plotted on the 1991 and 2008 upper bound. ● (TR polymers). ■ (PIMs). ◆ (Perfluoropolymers).

As a matter of fact, different parameters can affect the permeability of the polymers. Jiang and Kumar [37] conducted experiments to study the performance of hydrocarbons and nitrogen mixtures separation through silicone-coated polymeric membranes. It was found that permeability and selectivity are significantly lower in gas mixtures as compared to pure gases. Coombe and Nieh [38] measured the performance of perfluorodioxole polymeric membranes air separation and investigated the relationship between combustion parameters and membrane performance by experimentation.

Pressure and temperature can also affect the permeability of the polymers, and the permeability can exhibit different behaviors with changes in the pressure. Alsari et al. [39] studied the effect of membrane thickness and pressure on the gases permeability in dense polyphenylene oxide (PPO) membranes experimentally. They used a sweep gas on the permeate side and air on the feed side; they found that the selectivity of O_2 (α_{O_2/N_2})

increased with the feed pressure, as shown in Figure 5. This can be attributed to the increase in O_2 permeability and the decrease in N_2 permeability with the pressure. Similarly, different behavior was recorded for the temperature effect on the permeability. Feng et al. [40] found that the permeability is increased with the temperature, following the Arrhenius type relationship, and the selectivity (α_{O_2/N_2}) decreased. Dixon-Garrett [41] found that the ethylbenzene permeability decreased with increase in temperature and pressure.

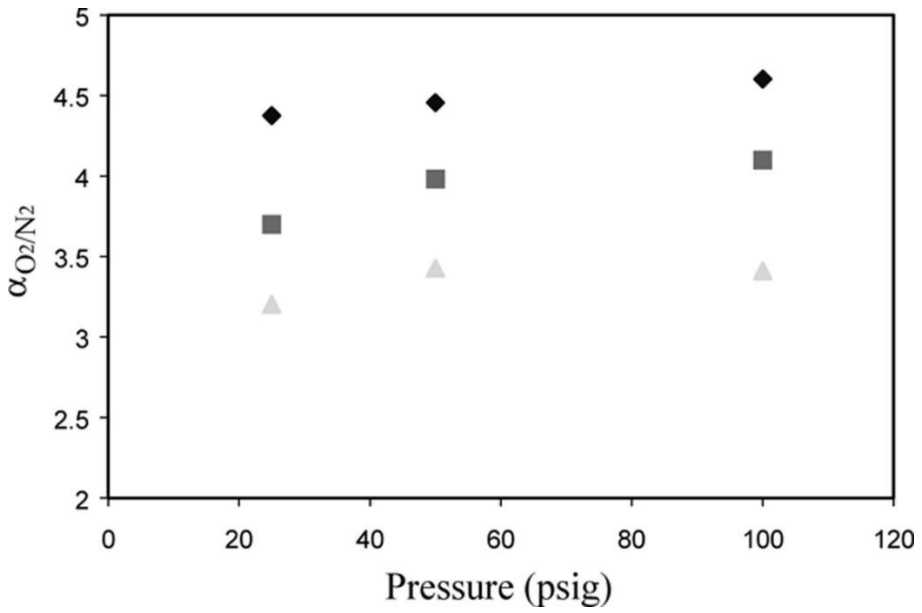

Figure 5: O_2 selectivity ($\alpha_{O2/N2}$) against feed pressure for different membranes thickness ♦ 6.7 μm, ▪ 10.6 μm and ▲ 12.4 μm. [39].

Numerical investigations through computer software became a very convenient method to study air separation. Commercial and energy studies were conducted to compare different techniques of gas separation. Ahmad et al. [42] simulated CO_2 capture from natural gas to find the optimal design of the separation using Aspen HYSYS. They found that the minimum cost for the gas process can be achieved by the double stage separation

with a permeate recycle system. A numerical parametric study of energy and mass balances for a single membrane process was carried out by Zhao et al. [43]. They used PRO II software to build a model for CO_2/N_2 mixture separation by cardo polyimide membrane. Kawachale et al. [44] used the Fluent program to study the mixing behavior of gases near the membrane, and the fluxes through it using 2D and 3D models. Binns et al. [45] used ASPEN HYSYS software to simulate gas separation by a multi-stage hollow fiber membrane. They compared different connections and arrangements of the separation system.

Dong et al. [46] solved their model of gas separation in MATLAB using a TR-PBO hollow fiber membrane in a carbon capture application, and they proposed to include the shell-side pressure drop in the gas separation models. Zhang et al. [47] studied numerically the effect of membrane module design on the removal rate of SO_2. The results showed better permeation rates while increasing the number of fibers and decreasing the membrane thickness. Choi et al. [48] performed a study on O_2 removal from exhaust gas stream using polymeric membrane for complete capture of CO_2. They evaluated the convinced changes in polymer morphology and separation performance data considering single gas permeation. In the present study, Fluent 12.1 code is utilized to perform a detailed numerical study on the characteristics of air separation using polymeric membranes for oxygen enriched air combustion applications [49].

2.3 Ion Transport Membranes

Developing and enhancing ITM is one of the most commonly researched subjects in air separation in the past decade; new materials and modifications in this type of membranes

continuously being created [50, 51, 52, 53]. Chen et al. [54] proposed a modified SCF ITM integrated oxy-fuel combustion process. Based on their experiment, this modification can prevent the membrane from degradation by adding 5% of O_2 with the swept CO_2.

Further, several experimental studies were conducted to investigate the separation stability with different combinations, and to find the separation process effectivity. Wang et al. [55] investigated the stability of BBCN ceramic hollow fiber membranes using a CH_4 sweep gas and the usage of He to recover the permeation of O_2. Wang et al. used steam sweep gas [56] in a BCFZ membrane and by Runze [53] in an LSCF membrane. Kirchen et al. [57] developed an experimental ITM reactor to investigate the coupling between oxygen permeation and fuel conversion.

In-transport membrane (ITM) is an air separation method that needs to be investigated to be compiled with oxy-fuel combustion process. Yantovski et al. [58] used ITM to feed oxygen for an oxy-fuel combustion power plant; they found that the corresponding turbine inlet temperatures ranged between 1300 to 1500^oC and the thermal efficiencies ranged from 46 to 55%. Chen et al. [59] designed and simulated an oxy-fuel combustion process integrated with ITM separation cell, and they found lower efficiency in this process than that using cryogenic distillation air separation. They used two heating stages for the fed air and another two stages for the swept CO_2. Habib et al. [60] investigated syngas oxy-fuel combustion numerically using oxygen transport reactor (OTR), air was fed to provide the oxygen into the sweep side through the ion transport membrane permeating.

Hong et al. [61] established a numerical model to resolve the oxygen transport through the ITM. While Habib et al. [15] modeled an isothermal multi-channel reactor numerically for oxy-fuel combustion to study the permeation and combustion behavior at different operation conditions. CH_4/CO_2 mixture was swept to react with the permeated oxygen, the reaction has increased oxygen partial pressure gradient across the membrane as well as the membrane temperature, thereby the increase of the oxygen permeation.

A numerical and experimental study was investigated by Habib et al. [62] for La_2NiO_4 membrane in oxygen separation with different combinations. Nemitallah et al. [63] initiated a numerical study to understand the performance of an oxy-combustion ITM reactor and the effect of various parameters on the reactor operation. Ahmed et al. [64] proposed using a three-channel configuration reactor based on their results from a CFD study. Coroneo et al. [65] performed a numerical study to investigate the transport mechanism effect on the permeation rate. Hong et al. [66] numerically investigated laminar oxy-fuel diffusion flames on the permeate side of an ITM; they found that the flame location impacts the heat transfer and species diffusion from the reaction zone to the ITM, which affects the flame temperature and the oxygen permeation.

CHAPTER 3

MODEL DEVELOPMENT AND SOLUTION METHODOLOGY

3.1 Polymeric Membrane Modeling

3.1.1 Description of Polymeric Membrane Unit and Ranges of Parameters

The geometry and membrane properties of polymeric membrane model were made with reference to Feng et al. [40] shell-and-tube unit. A total number of 368 hollow fiber membranes were encased in a copper tubing of a shell and tube configuration. The current model utilizes an asymmetric hollow fiber polymeric membrane unit for air separation to perform the numerical simulations. This configuration of a single hollow fiber membrane unit and its shell is represented by the 2D schematic shown in Figure 6. Counter-current flow bore-side feed configuration was considered in this model to give better separation results [40].

Air (20.5 % and 79.5%, by volume) is fed to the fiber membrane cell in the bore-side and oxygen depleted air leaves as retentate at the end of this side. At the shell-side, methane is used as the sweep gas that has large molecular size to ensure no blocking in the membrane permeation [39]. As a matter of fact, the present study could also be useful for the application of oxygen enriched air combustion technology, which could take advantage of the swept CH_4 for combustion applications. Oxygen enriched air-methane

mixture leaves in the permeate outlet in the sweep cases, while oxygen enriched air leaves in the non-sweeping flow cases, the produced oxygen enriched air will be used to feed the oxygen transport reactor in the hybrid system. Pressure outlet conditions have been specified at the sweep and feed outlets (atmospheric pressure at the sweep side and specific pressure at the feed side as shown in Table 1), while mass flow rate inlets boundary conditions have been assigned for the sweep and the feed entries.

The membrane is modeled as a wall with coupled heat transfer mechanism to calculate its temperature based on the surrounding flows from both sides. The base case of this study has the same operating conditions as in Feng et al. [40] (no sweep flow, air is fed with varying flow rate at 23^{o}C, 100 psig feed pressure, and 0 psig permeate pressure). The effect of sweep flow was investigated by feeding 100% CH_4 at the shell side inlet with flow rate range from zero to 1.15×10^{-7} kg/s. Feed air with flow rate ranging from 3.3×10^{-9} to 5.89×10^{-8} kg/s was included with feed pressure ranging from 2 to 10 atm. Oxygen enriched air was used as a feed gas in the multi-stage configuration with oxygen mass fraction ranging from 0.228 to 0.8. Table 1 shows a summary of all operating conditions and ranges of parameters.

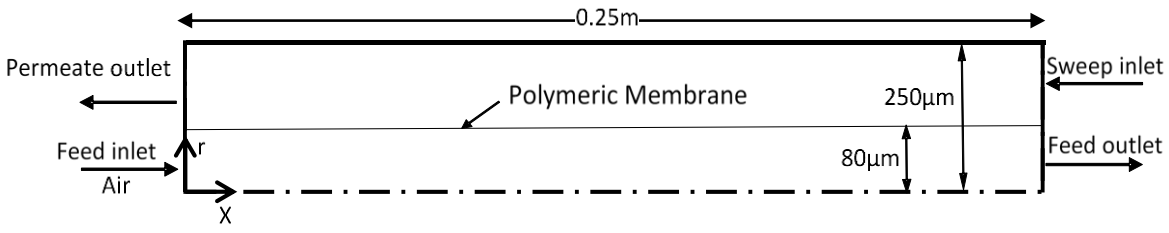

Figure 6: Hollow fiber membrane cell computational domain.

Table 1: Summary of the operating conditions of the polymeric membrane simulations.

Study	parameter	Range
Base case	Fed O_2 mass fraction	22.8%
	Feed flow rate	5.89×10^{-8} kg/s
	Sweep flow rate	Zero
	Feed pressure	6.8 atm
Multi-stage configuration	Fed O_2 mass fraction	22.8% - 80.0%
	Feed flow rate	7.4×10^{-9} - 5.89×10^{-8} kg/s
	Sweep flow rate	zero
	Feed pressure	6.8 atm
Effect of sweep flow rate	Fed O_2 mass fraction	22.8%
	Feed flow rate	5.89×10^{-8} kg/s
	Sweep flow rate	0 - 1.15×10^{-7} kg/s
	Feed pressure	6.8 atm
Effect of feed flow rate	Fed O_2 mass fraction	22.8%
	Feed flow rate	3.3×10^{-9} - 5.89×10^{-8} kg/s
	Sweep flow rate	zero
	Feed pressure	6.8 atm
Effect of feed pressure	Fed O_2 mass fraction	22.8%
	Feed flow rate	5.89×10^{-8} kg/s
	Sweep flow rate	1.15×10^{-9} kg/s
	Feed pressure	2 atm – 10 atm

3.1.2 CFD Modeling

The numerical model of the polymeric membrane gas separation unit was built and validated using Fluent software. The hollow fiber membrane cell, including the bore and shell sides, was simulated using 2D axisymmetric geometry due to the symmetry of this separation unit around its axis. Gambit software mesh builder software was used to develop the mesh to be introduced to the Fluent 12.1 software [49]. Fluent software is a built-in code that's available commercially, which contains the immense physical modeling competence required to model flow, heat transfer, and reactions [49]. The code solves the flow field through the solution of conservation equations including continuity, energy, momentum, and species. The numerical solution of the flow field includes the solution of the differential equations of continuity, energy, momentum, and species transport. The equations are presented as follows:

$$\nabla \cdot (\rho U) = S_i \tag{5}$$

$$\nabla \cdot (\rho UU) = -\nabla p + \mu \nabla^2 U \tag{6}$$

$$(\rho C_p)_f U \cdot \nabla T = \nabla \cdot (k_f \nabla T) \tag{7}$$

$$\nabla \cdot (\rho U X_i) - \nabla \cdot (\rho D_{i,m} \nabla X_i) = S_i \tag{8}$$

Where V is the velocity, μ is the dynamic viscosity, ρ is the density, p is the pressure, $D_{i,m}$ is the diffusion coefficient in the mixture, T is the temperature, and X_i is the mass fraction. Source/sink term, S_i, was used to consider the transfer of O_2 and N_2 across the polymer membrane. To include this source/sink term in the governing equations as

presented above, user defined functions (UDF) were written in Visual C++ and compiled and hooked to the Fluent software to close the governing equations system [67, 68, 69]. The law that controls the flow of fluid through a porous medium which was used to solve for the permeation across the polymer membrane can be presented as following [9]:

$$J_{O_2/N_2} = \frac{P(p' - p'')}{L} \tag{9}$$

Where J is the permeation flux of O_2 or N_2 in mol/m^2/s and P is the permeability of the polymer membrane in mol.m/m^2/s/Pa. p' and p'' are the gas partial pressure on the feed side and the permeate side, and L is the membrane thickness. Based on the flux equation, the equation for the source/sink term is developed for both O_2 and N_2 at each boundary membrane cell as follows:

$$S_i = \begin{cases} + \dfrac{J_{O_2/N_2}.A_{cell}.MW_{O_2/N_2}}{V_{cell}} & \text{, at the permeate side of the polymeric membrane.} \\ - \dfrac{J_{O_2/N_2}.A_{cell}.MW_{O_2/N_2}}{V_{cell}} & \text{, at the feed side of the polymeric membrane.} \end{cases} \tag{10}$$

Where $MW_{O2/N2}$ is the molecular weight of O_2 or N_2 in kg/mol, A_{cell} is the cell area in m^2 and V_{cell} is the cell volume in m^3. This term has a positive sign on the sweep side of the membrane and a negative sign on the feed side of the membrane as the species of O_2 and N_2 transport from the feed side to the permeate side of the membrane. The term, S_i, is only calculated for the boundary cells, cells in direct contact with the membrane from both sides, and is zero elsewhere in the computational domain. Also, this term has a value of zero for species other than O_2 and N_2. In all simulations, it was assumed that membrane permeability is independent of the feed gas composition, membrane

permeability is not affected by the swept gas, and the temperature distribution is uniform along the membrane (ambient temperature).

These governing equations are discretized by the finite volume method and then solved using algebraic approximations. Steady state pressure based solver was used. The first order upwind scheme was used to discretize the convective terms in the conservation equations. Calculations the semi-implicit method for pressure-linked equations (SIMPLE) algorithm was applied to account for coupling between pressure and velocity fields [70].The calculations were performed for each running case until the summation of all residuals is less than 10^{-6}.

3.1.3 Grid Independence Study

It is important to show that the used grid in this model has enough resolution to correctly predict the results in the computational domain to make sure that the results are independent of the grid. To validate this, different grid size results were calculated and compared. Figure 7 shows the distribution of N_2 permeation flux through the membrane length for different grid sizes. The results for the three grids are plotted for the same operating conditions.

For all grids, the flux is maximum close to the feed inlet (x = 0 m), then it reduces in the axial direction as shown in the figure. This can be attributed to the reduction in the mass fraction of N_2 in the feed side due to the permeation and increase of it in the permeate side due to accumulation. This results in lower partial pressure driving force across the membrane and, thus, N_2 flux is reduced. Based on the presented results, refining the grid

above the size of 18 × 6,250 cells led to insignificant changes in N_2 permeation flux. Based on that, all calculations were performed using a grid with the size of 18 × 6,250 cells.

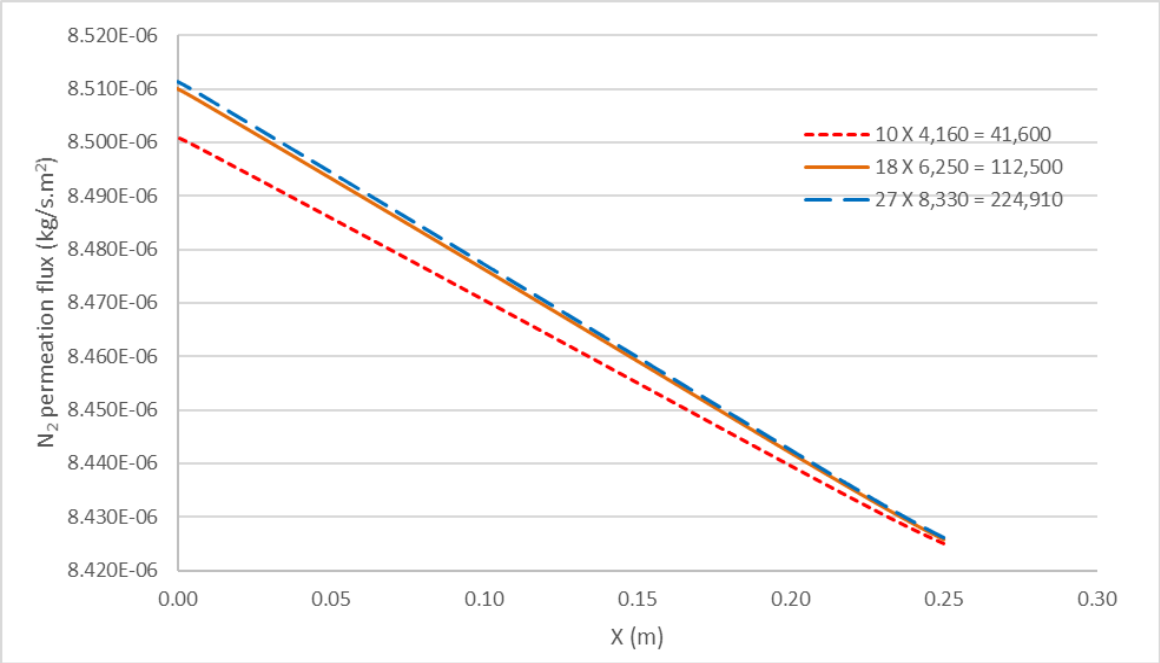

Figure 7: N_2 permeation flux through the membrane length for three different grids sizes at 6.8 atm feed pressure, 1 atm permeate pressure, 5.89×10^{-8} kg/s feed flow rate and zero sweep.

3.1.4 Model Validation

Experimental data by Feng et al. [40] were used to validate the present model for polymer membrane system. In their experiment, hollow-fiber membranes were used to separate air and produce oxygen and nitrogen. A total number of 368 hollow fiber membranes were encased in a copper tubing of a shell and tube configuration. Shell-side feed and bore-side feed with counter-current and co-current flow arrangements for different stage cuts

were tested in this study. It was found that the bore-side feed counter-current flow has the best performance. Table 2 represents the experimental data used in the validation study.

Figure 6 shows the considered polymer membrane unit in the present study which is a representation of one polymer membrane cell of the shell and tube configuration by Feng et al. [40]. So, the same mesh, details are mentioned above, is used in the validation study.

Table 2: The used experimental data for model validation.

Fiber outer diameter / length	Feed pressure	Permeate pressure	Temperature	Feed composition (% volume)		Permeance (GPU)	
				O_2	N_2	O_2	N_2
160μm / 0.25m	100 psig	0 psig	23ºC	20.5	79.5	9.3	1.8

The present model results and the experimental data by Feng et al. [40] are compared in terms of permeation flow rates of O_2 and N_2, and the gas concentrations at the permeated outlet and retentate as shown in Figures 8 and 9. The results for gas concentrations at the permeate outlet are presented as function of the stage cut (Θ) which is defined as:

$$\theta = \frac{permeate \quad flow}{Feed \quad flow} \tag{11}$$

Because of increasing the feed flow rate of air, N_2 retentate flux and O_2 permeate flux increased and the fraction of the penetrated O_2 to the fed O_2 increased. This resulted in an increase in O_2 mole fraction in the permeate side as shown in Figure 9 and reduction in N_2 mole fraction in the retentate as illustrated in Figure 8. Stage cut decreases with

increasing the feed flow rate while N_2 mole fraction decreases as presented in Figure 8. Similarly, increasing the feed flow rate resulted in an increase in the permeation flux of oxygen and increased its mole fraction in the permeate side as shown in Figure 9. This increase in the permeation flux is due to the increase in the mass fraction of O_2 on the feed side as the feed flow rate increases. The results in Figure 8 and Figure 9 show good agreement with the experimental data.

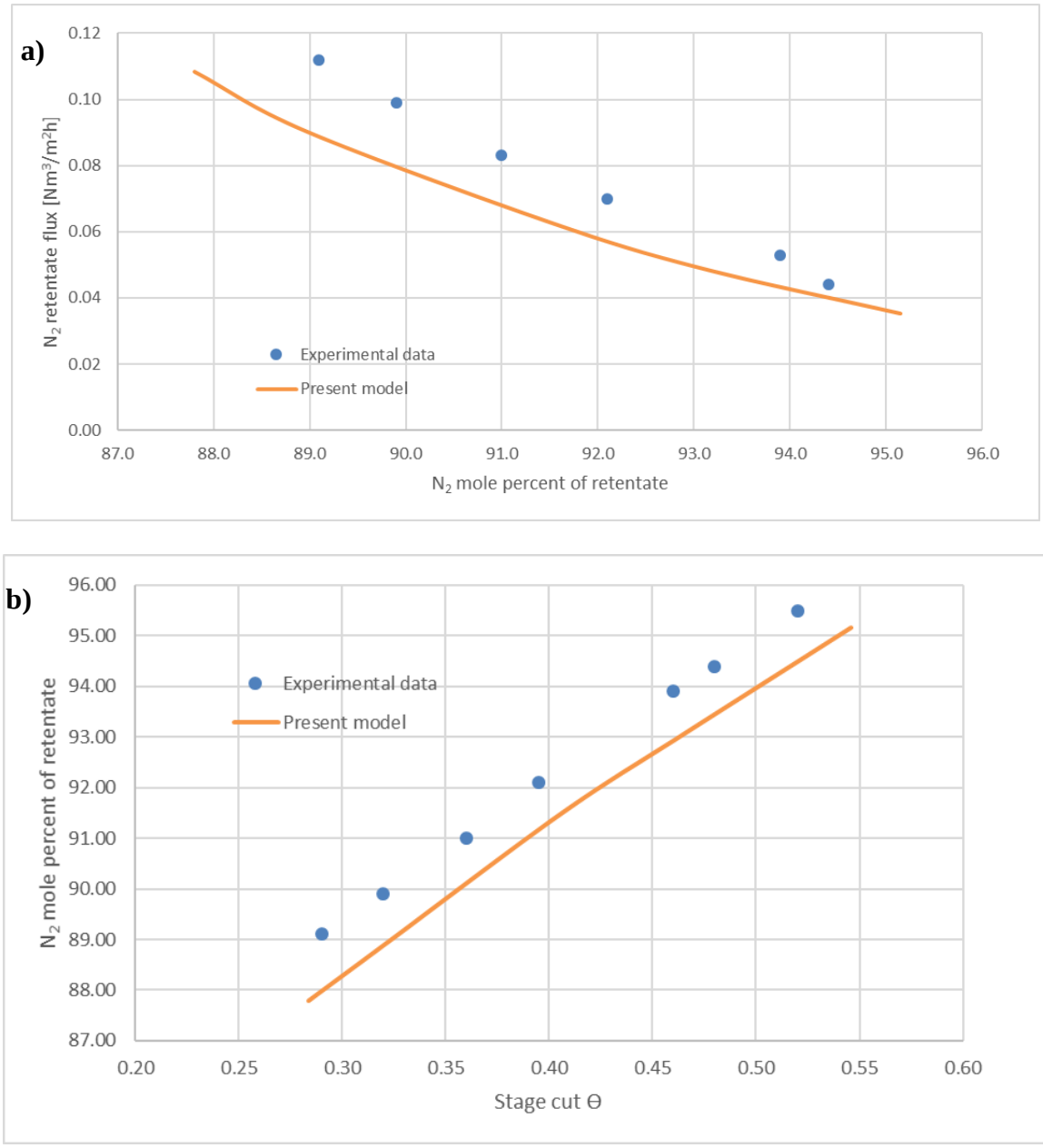

Figure 8: Present model predictions versus the experimental data by Feng et al. [40] at 6.8 atm feed pressure, 1 atm permeate pressure, varying feed flow rates and zero sweep; in terms of: a) N_2 retentate flux, and b) N_2 mole fraction of retentate.

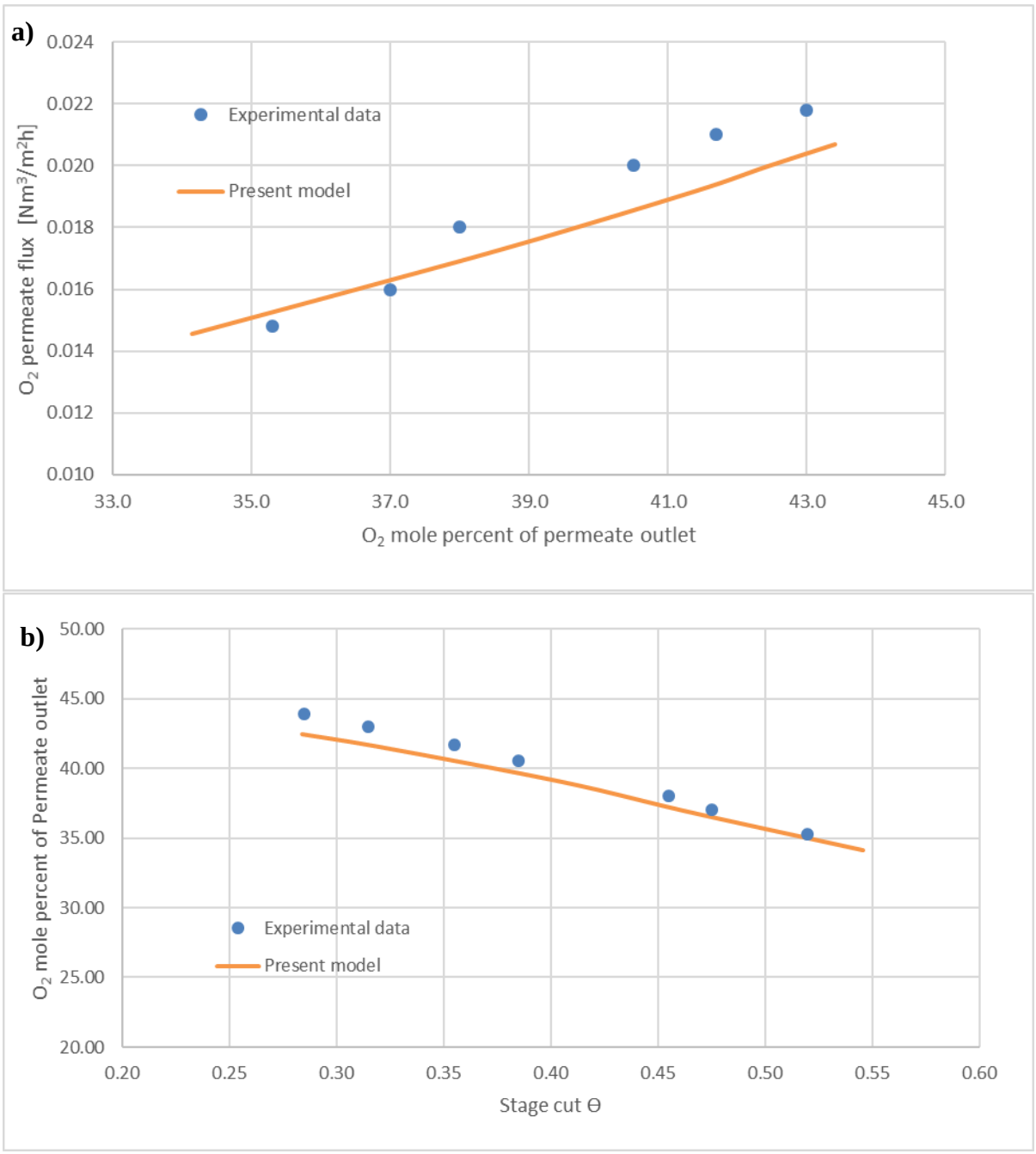

Figure 9: Present model predictions versus the experimental data by Feng et al. [40] at 6.8 atm feed pressure, 1 atm permeate pressure, varying feed flow rates and zero sweep; in terms of: a) O_2 permeate flux, and b) O_2 mole fraction of permeate outlet.

3.2 Oxygen Transport Reactor Modeling

3.2.1 Description of Membrane Unit and Ranges of Parameters

The current work utilizes an oxygen transport reactor (OTR) unit consist of tubular oxygen transport membrane (OTM) and surrounded by a shell to perform the numerical simulations. This configuration of an OTR unit is represented by the 2D schematic shown in Figure 10. The used geometry is 10 mm shell radius surround a 2 mm radius tubular OTM with 100 mm length and membrane thickness of 0.9 mm. LCF membrane is used as the OTM in this study, membrane properties of this model were made concerning Hunt et al. [71] study.

CH_4/CO_2 mixture is supplied at the sweep side (inside the OTM) as a diluted fuel by CO_2 with various CH_4/CO_2 ratio. While oxygen enriched air with different oxygen concentrations or atmospheric air (23.3 % and 76.7 % by mass) is fed at the shell side. O_2 depleted air leaves as retentate at the feed outlet due to the oxygen permeation through the OTM. While CO_2 and H_2O leave the sweep side as the exhaust in case of a stoichiometric combustion process. The sweep and feed inlet streams to be preheated before the OTR entries from the atmospheric temperature to 1173 K or 1123 K, high entrance temperature to the OTR is required to ensure the permeation process through the OTM, therefore, the combustion process. Mass flow rate inlets boundary conditions have been specified for the feed and the sweep entries, while atmospheric pressure outlet boundary conditions have been specified at the sweep and feed outlets. Co-current flow configuration was considered in this model to give better separation results, where Tan et

al. [72] was realized that the co-current flow configuration is better operating than the counter-current. Table 3 shows a summary of all operating conditions and ranges of parameters included in different studied cases.

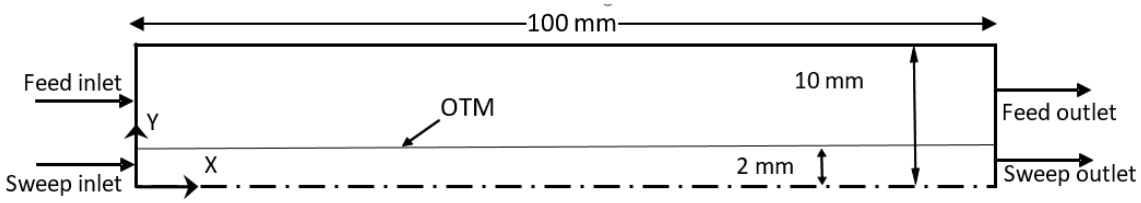

Figure 10: Computational domain of the present oxygen transport reactor (OTR).

Table 3: Summary of the operating conditions of the OTR simulations.

Study	parameter	Range
OTM Fed O_2 mass fraction effect	Fed O_2 mass fraction	23.3% - 85.0%
	Feed flow rate	5.0×10^{-6} kg/s
	Sweep flow rate	2.0×10^{-7} kg/s
	Swept CH_4 mass fraction	0.50
	Streams inlet temperature	1173
Effect of sweep flow rate	Fed O_2 mass fraction	52.25%
	Feed flow rate	5.0×10^{-6} kg/s
	Sweep flow rate	8.0×10^{-8} - 8.0×10^{-7} kg/s
	Swept CH_4 mass fraction	0.50
	Streams inlet temperature	1173
Effect of feed flow rate	Fed O_2 mass fraction	52.25%
	Feed flow rate	2.0×10^{-6} - 1.0×10^{-5} kg/s
	Sweep flow rate	2.0×10^{-7} kg/s

	Swept CH_4 mass fraction	0.50
	Streams inlet temperature	1173
Swept CH_4 mass fraction effect	Fed O_2 mass fraction	52.25%
	Feed flow rate	5.0×10^{-6} kg/s
	Sweep flow rate	2.0×10^{-7} kg/s
	Swept CH_4 mass fraction	0.05 – 1.00
	Streams inlet temperature	1173
Stoichiometric cases	Fed O2 mass fraction	52.25%
	Feed flow rate	1.14×10^{-6}– 3.81×10^{-6} kg/s
	Sweep flow rate	1.5×10^{-6} - 2.0×10^{-6} kg/s
	Swept CH4 mass fraction	0.10
	Streams inlet temperature	1123, 1173

3.2.2 CFD Modeling

Like the model of polymeric membrane, the numerical model of the OTR was built and validated using Fluent software. The OTR, including the OTM tube and shell sides, was simulated using 2D axisymmetric geometry due to the symmetry of this separation unit around its axis (Figure 10). Gambit software mesh builder software was used to develop the mesh, which will be introduced to the Fluent 16.1 software. The numerical solution of the flow field includes the solution of the differential equations of continuity, energy, momentum, and species transport (equations 5 to 8). Regarding the methane reaction

kinetics model, the study utilizes the single-step finite rate reaction kinetics model as follows:

$$CH_4 + 2O_2 \rightarrow CO_2 + 2H_2O \quad (12)$$

The complete combustion products are assumed (CO_2 and H_2O). The reaction rates calculated based on default values of the activation energy and the pre-exponential coefficient available in the fluent software, 2.027 $\times 10^8$ J/kg.mol, and 2.119×10^{11} respectively.

Radiation model is included in the computational work to avoid over-prediction of the reactor temperature. Discrete Ordinates (DO) radiation model is used in the OTR model since it has high prediction ability of oxy-fuel combustion characteristics in microchannels [49]. DO solves radiative transfer equation for absorbing, emitting, and scattering mediums. The radiative transfer equation in the direction $\vec{S}$ is given following [49].

$$\frac{dI(\vec{r},\vec{s})}{ds} + (a + \sigma_s)I(\vec{r},\vec{s}) = \frac{an^2(\sigma T^4)}{\pi} + \frac{\sigma_s}{4\pi}\int_0^{4\pi} I\,(\vec{r},\vec{s}')\phi(\vec{s}.\vec{s}')d\Omega' \quad (13)$$

Where, n is the refractive index, a is the absorption coefficient $m^{-1,}$ I is the intensity of radiation and s is the path length.

Oxygen separation through the dense non-porous LCF OTM is achieved using oxygen permeation flux equation as presented by Xu and Thomson [14].

$$J_{O_2,OTM} = \frac{D_V K_r (p'^{0.5}_{O_2} - p''^{0.5}_{O_2})}{2LK_f (p''_{O_2} p'_{O_2})^{0.5} + D_V (p'^{0.5}_{O_2} + p''^{0.5}_{O_2})} \quad (14)$$

Where D_v is the diffusion coefficient of oxygen vacancy, cm^2/s, K_r is the reverse reaction rate, $mol/cm^2/s$, K_f is the forward reaction rate, $m/atm^{0.5}/s$, p' and p'' are the gas partial pressure on the feed side and the permeate side respectively, pa, and L is the membrane thickness, mm. D_V, K_r, and K_f could be expressed as following:

$$D_V = D_V^{\,o} \exp\left(-\frac{E_D}{RT}\right) \quad (15)$$

$$K_r = K_r^{\,o} \exp\left(-\frac{E_r}{RT}\right) \quad (16)$$

$$K_f = K_f^{\,o} \exp\left(-\frac{E_f}{RT}\right) \quad (17)$$

Where E_D, E_r, and E_f are the activation energies, kJ/mol. K_r°, K_f°, and D_V° are pre-exponantioal factors. Table 4 shows the values of the activation energies and the pre-exponantioal factors that fitted experimently by Hunt et al. [71] for the LCF membrane:

Table 4: Experimentally determined material constants values by Hunt et al. [71].

Material constant	Pre-exponential factor		Activation energy (J/mol)
	Units	Value	
k_f	$cm/atm^{0.5}$ s	4.20×10^{11}	3.37×10^5
k_r	mol/cm^2 s	1.34×10^{10}	3.79×10^5
D_V	cm^2/s	4.98×10^{-3}	5.96×10^4

Based on the permeation equation (14), the equation for the source/sink term is developed for both O_2 and N_2 at each boundary membrane cell as follows:

$$S_i = \begin{cases} +\dfrac{J_{O_2,OTM}.A_{cell}.MW_{O_2}}{V_{cell}} , & \text{at the sweep side of the OTR} \\ -\dfrac{J_{O_2,OTM}.A_{cell}.MW_{O_2}}{V_{cell}} , & \text{at the feed side of the OTR} \end{cases} \quad (18)$$

Where MW_{O2} is the molecular weight of O_2, A_{cell} is the cell area in m^2 and V_{cell} is the cell volume in m^3. This term has a positive sign on the sweep side of the OTR and a negative sign on the feed side of the OTR as the species of O_2 transport from the feed side to the permeate side of the OTR. The term, S_i, is only calculated for the boundary cells, cells in direct contact with the membrane from both sides, and is zero elsewhere in the computational domain. Also, this term has a value of zero for species other than O_2. User defined functions (UDF) written in Visual C++ are coupled and hooked to the Fluent software to account for the transfer of O_2 across the OTM. UDFs are attached to the software through a source/sink term in mass and momentum equations.

3.2.3 Grid Independence Study

To ensure that the used grid in this model has enough resolution to correctly predict the results in the computational domain and make sure that the results are independent of the grid. Different grid size results were calculated and compared.

Figure 11 shows the permeation flux of the oxygen along the membrane length for four different grid sizes. The results for the four grids are plotted for the same operating conditions. For all grids, the flux is increasing at the sweep inlet, then it is reaching its maximum at ($x \approx 0.4$ m), then it reduces in the axial direction as shown in the figure. This

can be attributed to the increasing of the membrane temperature as the methane oxy-fule combustion starts at near to the sweep inlet, and the flame stretched its highest temperature at (x ≈ 0.4 m). The rapid decreasing of the permeation flux is due to the termination of the combustion, and the increase of the oxygen partial pressure at the sweep side.

Based on the presented results, refining the grid above the size of 23,600 grid led to insignificant changes in O_2 permeation flux. Based on that, all calculations were performed using a grid with the size of 23,600 cells.

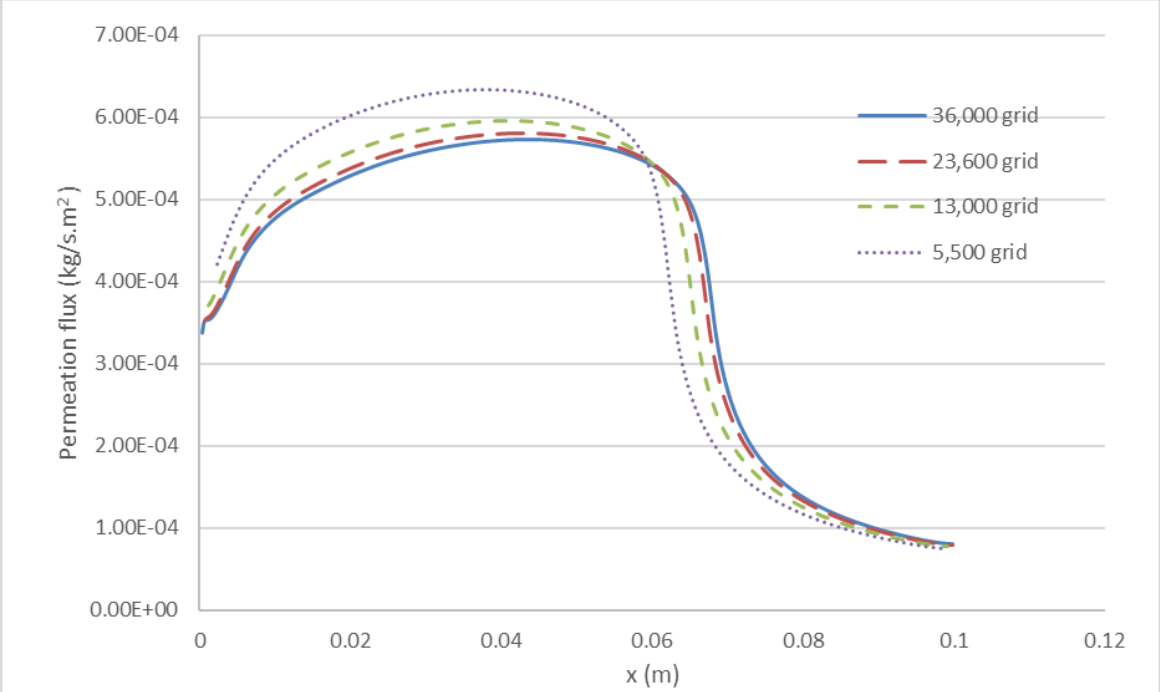

Figure 11: Permeation flux through the membrane length for four different grids sizes at (1.0×10^{-6} kg/s feed flow rate with 0.525 O_2 mass fraction, 2.0×10^{-7} kg/s sweep flow rate with 0.50 CH_4 swept mass fraction, and $\phi > 1.0$).

3.2.4 Model Validation

Experimental data by Hunt et al. [71] were used to validate the present model for the OTM permeation. In their experiment, bottom cell reactor was used to permeate the oxygen through the LCF membrane. Different membrane thicknesses were included in their study to provide higher accuracy model. Table 5 and figure 12 represent the experimental data used in the validation study.

Table 5: Experimental data were used to validate the model, Hunt et al. [71].

OTM Thickness (mm)	Feed gas	Sweep gas	Sweep gas flow rate	Feed flow rate	Configuration	Membrane effective area
0.9 – 1.4	Air	CO_2	1500 – 2400 sccm	6000 sccm	Flat membrane	4.76×10^{-3} m^2

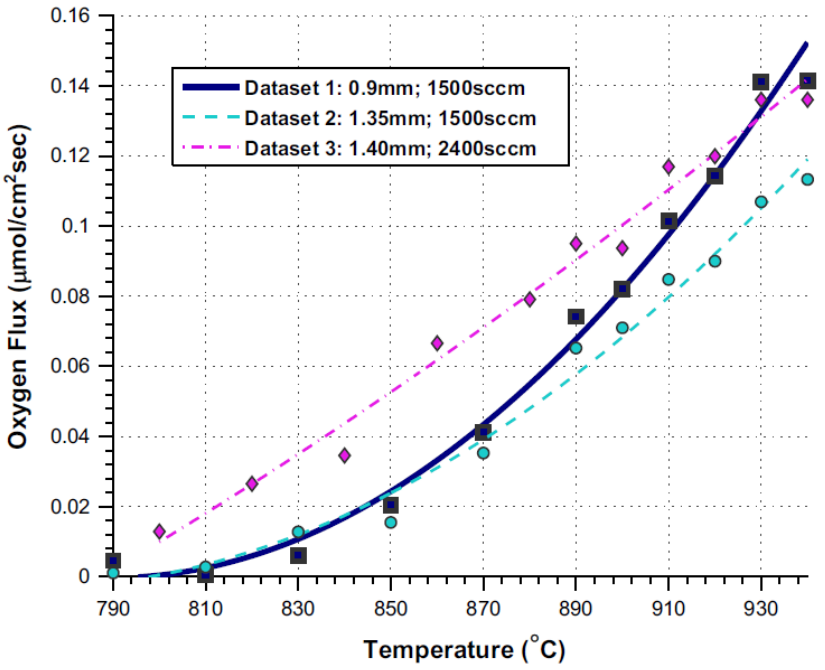

Figure 12: O_2 permeation flux against temperature datasets over a range of membrane thicknesses, Hunt et al. [71].

Figure 13 shows good agreement between the model results and the experimental data. It compares the permeation flux results from the current model with the experimental data, two different sets of experimental data of O_2 permeation over a range of membrane temperature with different membrane thickness and sweep flow rate. The results show that the total oxygen permeation is affected by the membrane temperature, the total permeation flux through the membrane is increasing as the temperature increases, which realized on the permeation equation (14).

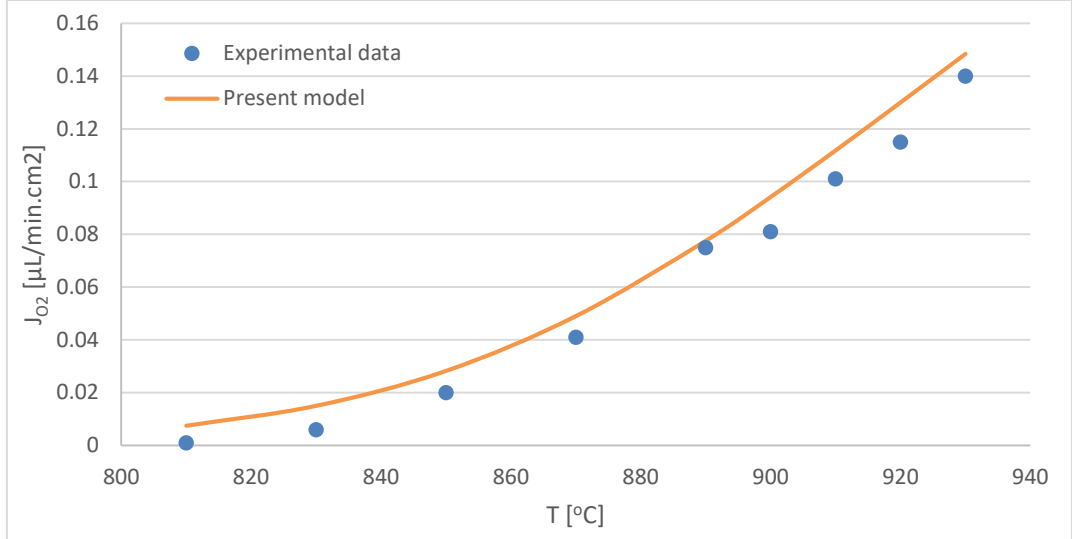

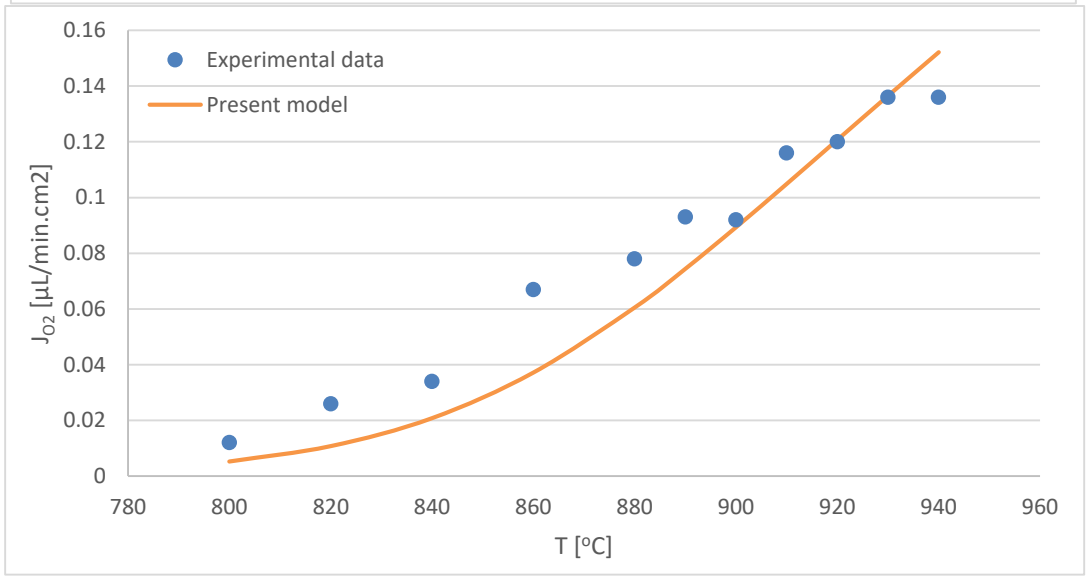

Figure 13: Present model predictions in terms of O_2 permeation flux against the experimental data by Hunt et al. [71]. a) 0.9 mm membrane thickness, and 1500 sccm sweep flow rate, and b) 1.4 mm membrane thickness, and 2400 sccm sweep flow rate.

CHAPTER 4

RESULTS AND DISCUSSION

4.1 Polymeric Membrane Simulation Results and Discussion

4.1.1 Effect of Sweep Gas Flow Rate

In this section, the effects of sweep gas flow rate on the permeation characteristics of the present polymeric membrane unit are investigated. CH_4 is used as the swept gas under atmospheric pressure. Figure 14 shows how the change in sweep gas flow rate can affect the local distributions of permeation flux of N_2 and O_2. The results are also compared with the case of zero sweep gas flow rate. The plots show increase in the fluxes of O_2 and N_2 while increasing the sweep flow rate. This can be attributed to the reduction of O_2 and N_2 partial pressures in the permeate side due to the effective purging process of the permeated gases by the sweeping gas. Reductions in O_2 partial pressure are encountered on the permeate side while increasing the sweep gas flow rate as presented in Figure 15. The improvements in the permeation fluxes of both O_2 and N_2 are significant when the flow sweep flow rate is increased from zero up to a value of 5.742×10^{-8} kg/s. Any further increase in the sweep flow rate does not result in any change neither the permeation fluxes of O_2 and N_2, as shown in Figure 14, nor in partial pressures of O_2 and N_2, as shown in Figure 15. This can be attributed to the limit of permeability of the present

membrane, i.e. the maximum permeation flux is approached depending on the material of the membrane. At sweep flow rate of 1.148×10^{-9} kg/s, the lowest considered sweep flow rate, sharp increases in the distributions of permeated oxygen and nitrogen flow rates are encountered. This may be attributed to the obtained sharp increase in oxygen and nitrogen partial pressure distributions in the permeate side as presented in Figure 15 (looking from the sweep inlet at x=0.25 to the sweep outlet x=0.0), this increase in partial pressure will reduce the partial pressure difference and decrease the permeation flux. For the considered range of sweep flow rate except for the case of zero flow rate, identical values of the permeation fluxes are obtained at sweep gas inlet section, at x=0.25 m. This can be attributed to the partial pressure driving force reduction across the membrane at that section which corresponds to the retentate exit section of the feed flow.

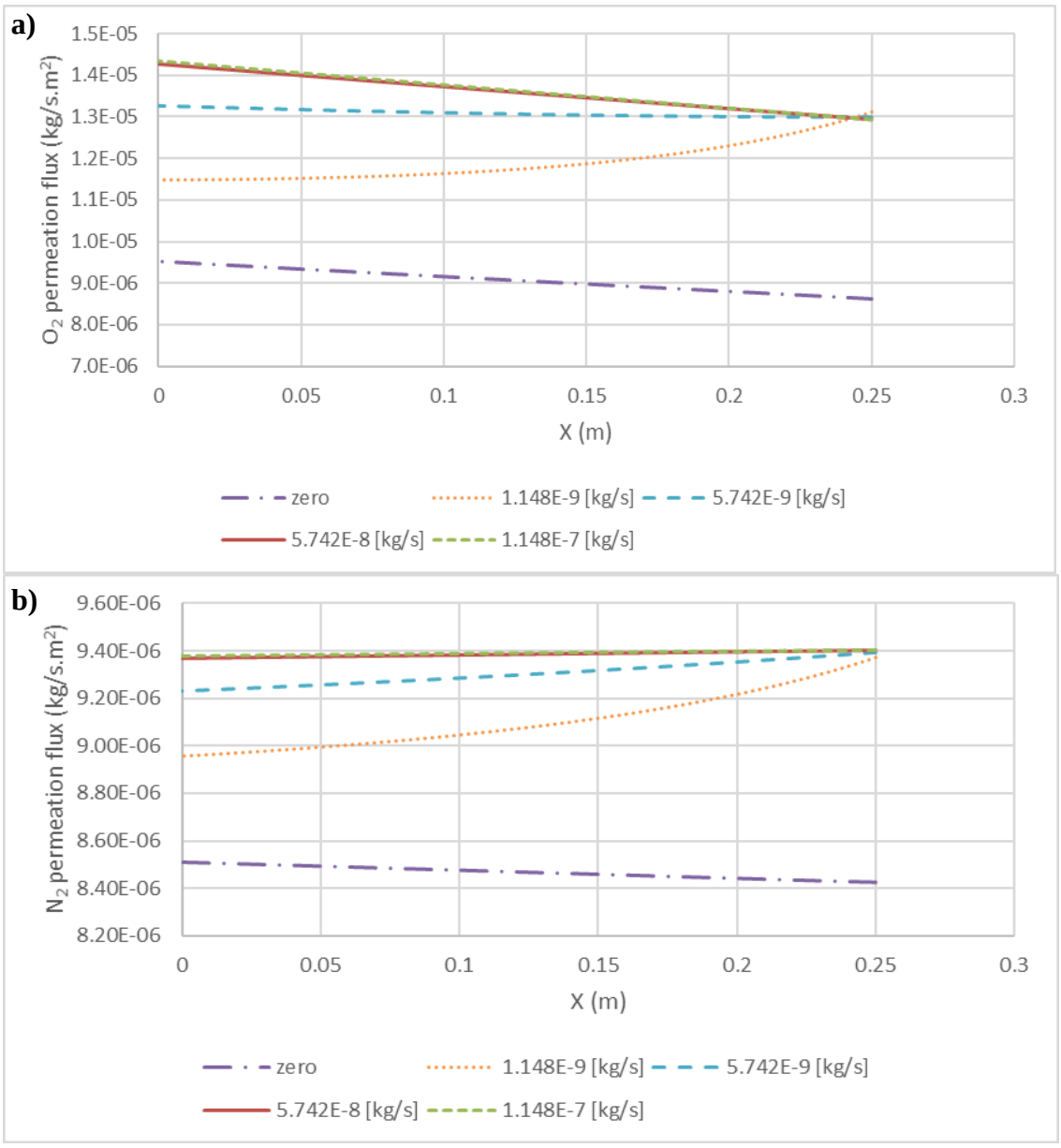

Figure 14: Distributions of: a) O_2 permeate flux rate and b) N_2 permeate flux rate, over a range of sweep gas flow rate at 6.8 atm feed pressure, 1 atm permeate pressure and 5.89×10^{-8} kg/s feed flow rate.

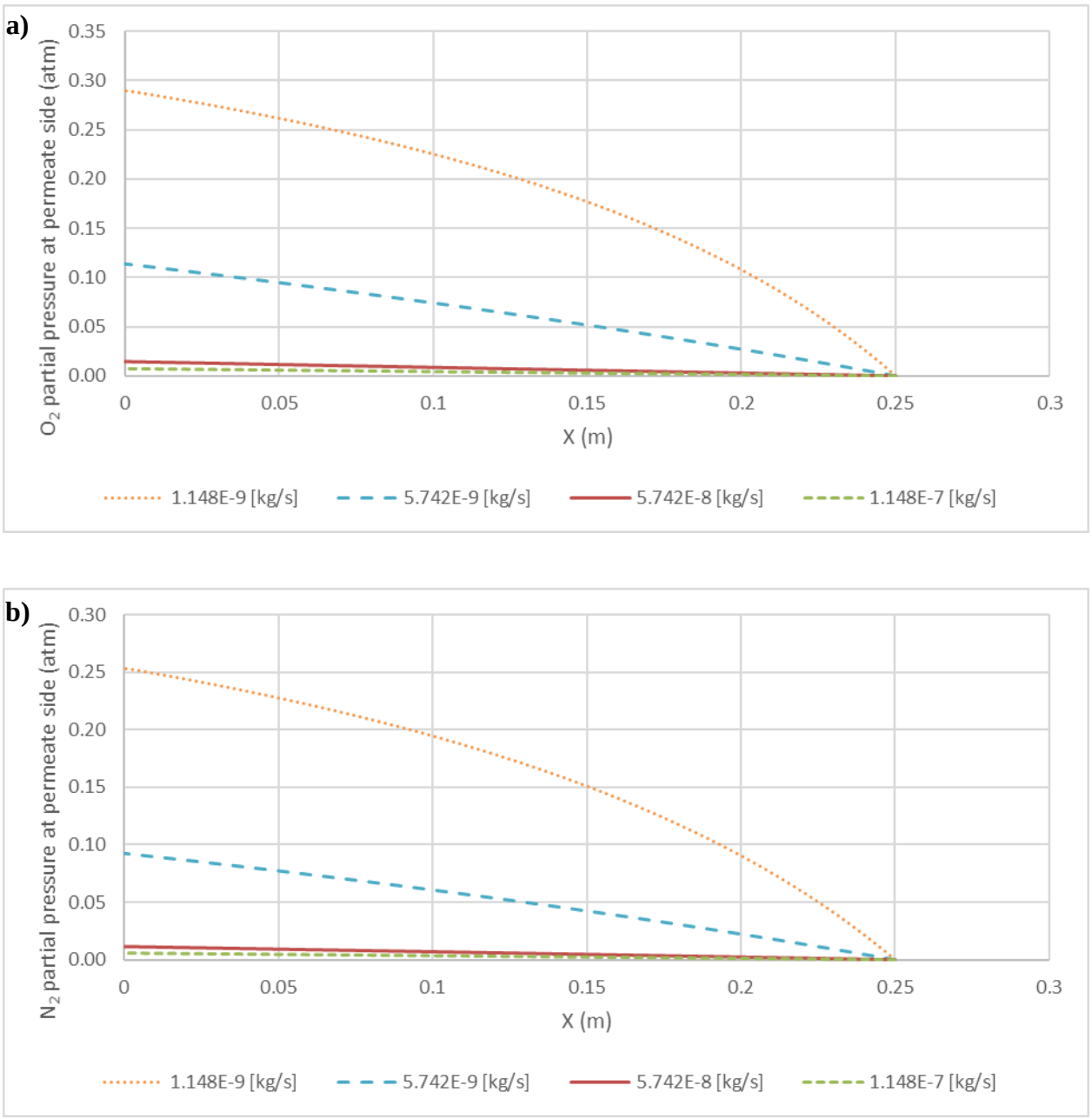

Figure 15: Distributions of: a) O_2 partial pressure and b) N_2 partial pressure, at the sweep side along the membrane surface over a range of sweep gas flow rate at 6.8 atm feed pressure, 1 atm permeate pressure, and 5.89×10^{-8} kg/s feed flow rate.

Figure 16, (a), shows the overall permeation flow rates of O_2 and N_2 through the membrane over a range of sweep gas flow rate. Also, the corresponding values of mass fractions of O_2 and N_2 calculated at permeate outlet and retentate outlet are presented in

Figure 16, (b). The optimal value of the sweep flow rate could be observed from Figure 16 where the permeation flow rates became unchanged. This optimal value could produce higher permeation and concentration of the oxygen enriched air with low energy consumption. As shown in the figure, the total permeation flow rates of O_2 and N_2 increase as the sweep flow rate increases. However, the increase in the permeation flux of O_2 is insignificant for sweep flow rates higher than 2.0×10^{-8} kg/s. The improvement in permeation flux of N_2 is insignificant at lower sweep flow rates as compared to O_2. Interestingly, at zero sweep gas flow rate, the permeation flux of N_2 is greater than that of O_2 as shown in Figure 16, (a). So, sweep gas should be used to obtain higher oxygen permeation rates and higher concentrations of O_2 at permeate outlet. The plots of mass fractions of O_2 in Figure 16, (b), show enhance in the concentrations of O_2 at the permeate exit while increasing the sweep gas flow rate, similar values of optimum sweep gas flow rate are obtained from plots in Figure 16. The concentrations of N_2 at the retentate exit section also increased while increasing the sweep flow rate up to a certain optimum value. This increase in N_2 concentrations at the exit section of the feed side may be attributed to the increase of O_2 flux across the membrane while increasing the sweep gas flow. Thus, oxygen concentrations in the feed side are reduced and, accordingly, N_2 concentrations are increased. Similar trends were observed in the experiments by Li et al. [73].

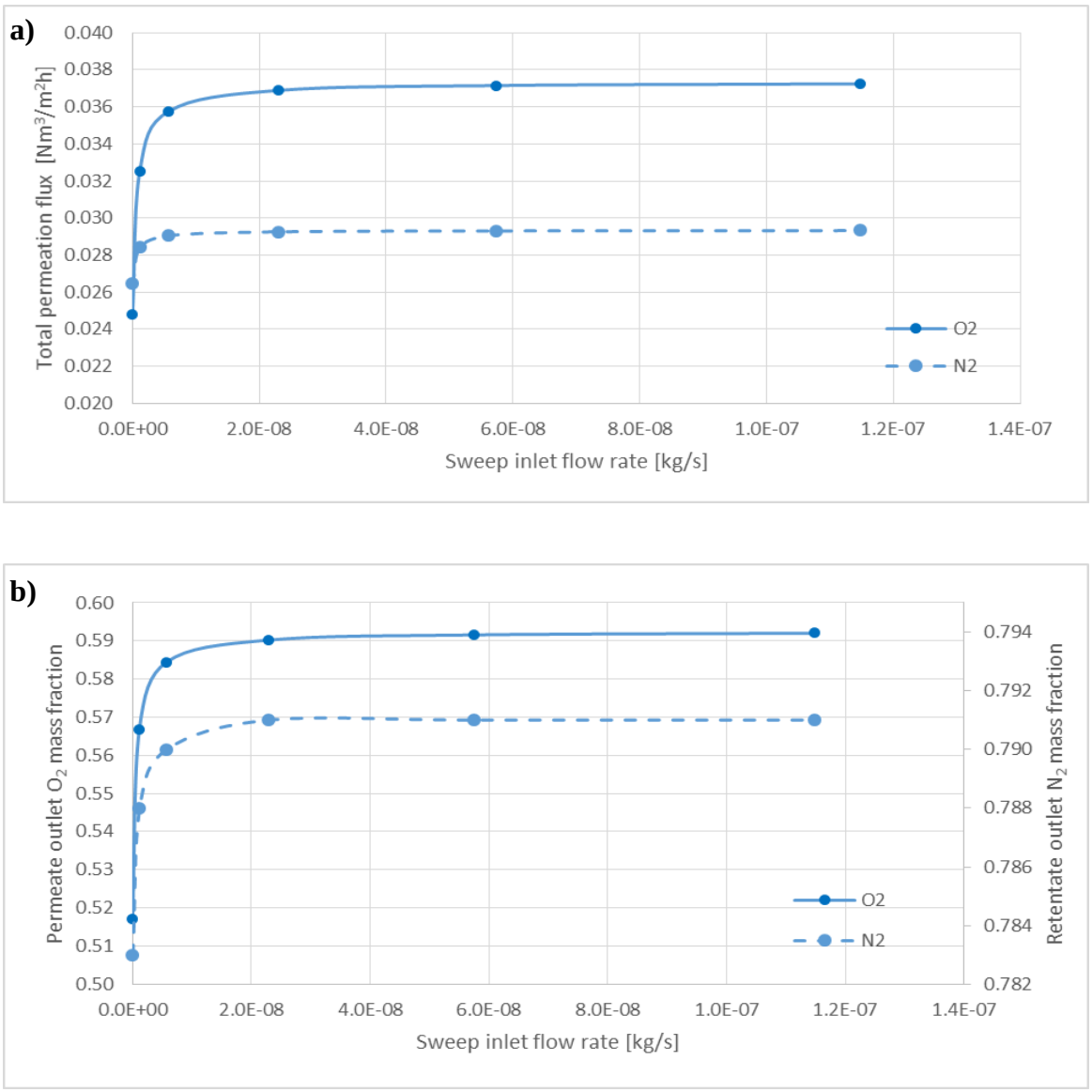

Figure 16: Distribution of: a) O_2 and N_2 total permeate fluxes, and b) mass fractions of O_2 and N_2, calculated at permeate outlet and retentate outlet over a range of sweep gas flow rates at 6.8 atm feed pressure, 1 atm permeate pressure, and 5.89×10^{-8} kg/s feed flow rate.

4.1.2 Effect of Feed Gas Flow Rate

The change in sweep or feed flow rates results in modifications in the flow field and, accordingly, change in partial pressure distributions of permeating gases on both sides of the membrane. This directly affects the rate of permeation across the membrane as it is a

direct function of the permeating gas partial pressure. Increasing the sweep flow rate resulted in purging of the permeated gases and, accordingly, their partial pressures on the permeate side are reduced resulting in higher permeation rates. This happened up to a certain flow rate at which permeation fluxes are maximum, and partial pressures on the permeate side are the lowest. Similar effects are obtained while increasing the feed gas flow rate as shown in Figure 17 at zero sweep gas flow rate. Increasing the feed flow rate resulted in an enhance in the oxygen permeation flux. This enhancement is due to the increase in flow velocity on the feed side at the membrane surface which results in purging of N_2 enriched air after O_2 and N_2 separation and, thus, the partial pressure of oxygen is increased on the feed side and, therefore, the permeation flux is increased. The increase in oxygen concentrations in the feed side near the membrane while increasing the feed gas flow rate is clearly presented in Figure 18, (a). Interestingly, increasing the feed flow rate resulted in a reduction in nitrogen permeation flux which helps to get higher oxygen concentrations at permeate outlet as shown in Figure 19. Due to the purging of N_2 enriched air after separation of O_2 and N_2 at a certain location, the fresh incoming air has lower N_2 concentrations which result in a reduction in N_2 partial pressure in the feed side. This results in a decrease in partial pressure driving force for N_2 permeation and, accordingly, N_2 permeation flux is reduced as shown in Figure 17. The distributions of N_2 mass fractions as a function of feed gas flow rate are presented in Figure 9, lower plot. Reductions in N_2 concentrations at the membrane surface in feed side are encountered while increasing the feed gas flow rate. The increase in oxygen permeation flux is insignificant for feed flow rates higher than 4.0×10^{-8} kg/s. This can be attributed to reaching the limit of oxygen permeation based on partial pressure

differences and membrane permeability. Also, increasing the feed gas flow rate more than 2.0×10^{-8} kg/s resulted in controlling the N_2 partial pressure a fixed value and no significant change in N_2 permeation flux is obtained. For the considered range of feed gas flow rate, N_2 permeation flux remained higher than that of O_2. As mentioned above (see Figure 16), at zero sweep gas flow rate, N_2 flux is greater than O_2 flux. However, the flux of oxygen approaches that of N_2 at higher feed flow rates as shown in Figure 17. The increase of O_2 permeation rate while increasing the feed flow rate resulted in higher O_2 mass fraction at permeate outlet as shown in Figure 19. Also, due to permeation of N_2 at higher flow rates than O_2 from the feed side to the permeate side, the retentate N_2 mass fraction decreases while increasing the feed gas flow rate as shown in Figure 19.

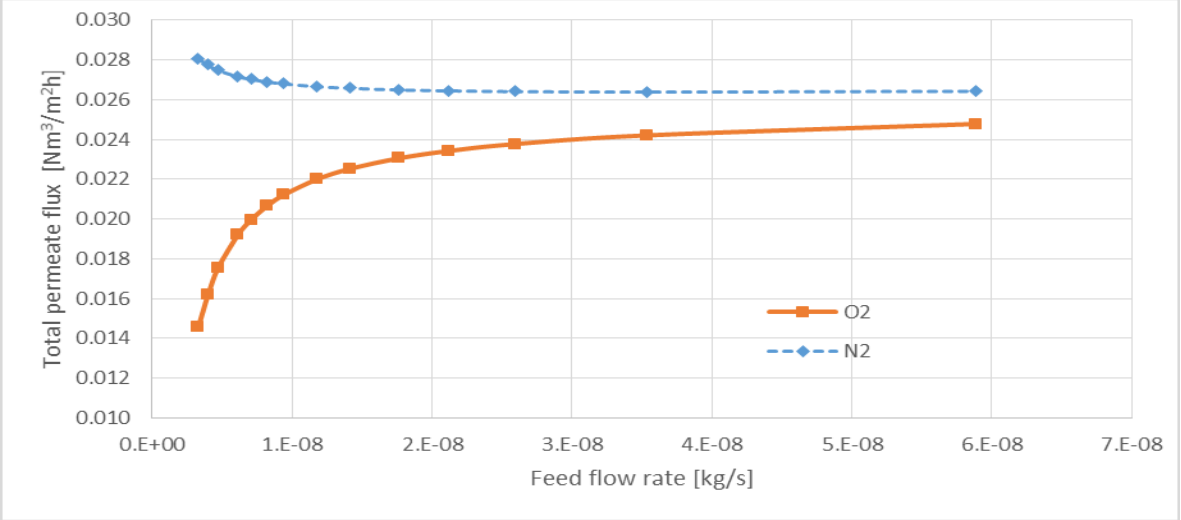

Figure 17: Effect of feed gas flow rate on the total permeate fluxes of O_2 and N_2 at 6.8 atm feed pressure, 1 atm permeate pressure, and zero sweep flow rate.

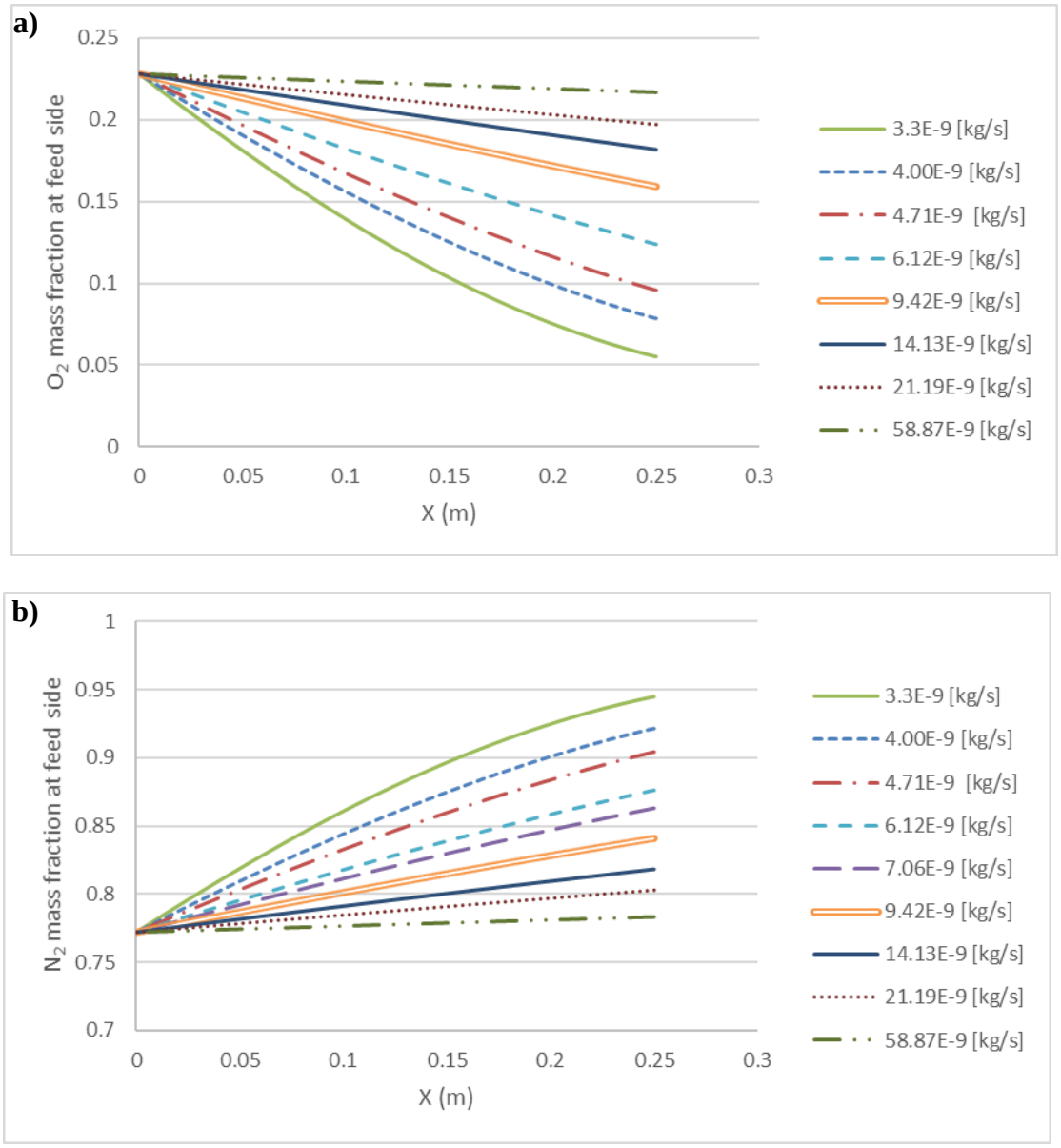

Figure 18: Distributions of: a) mass fractions of O_2 and b) mass fractions of N_2 along the membrane surface at feed side over a range of feed flow rate at 6.8 atm feed pressure, 1 atm permeate pressure, and zero sweep flow rate.

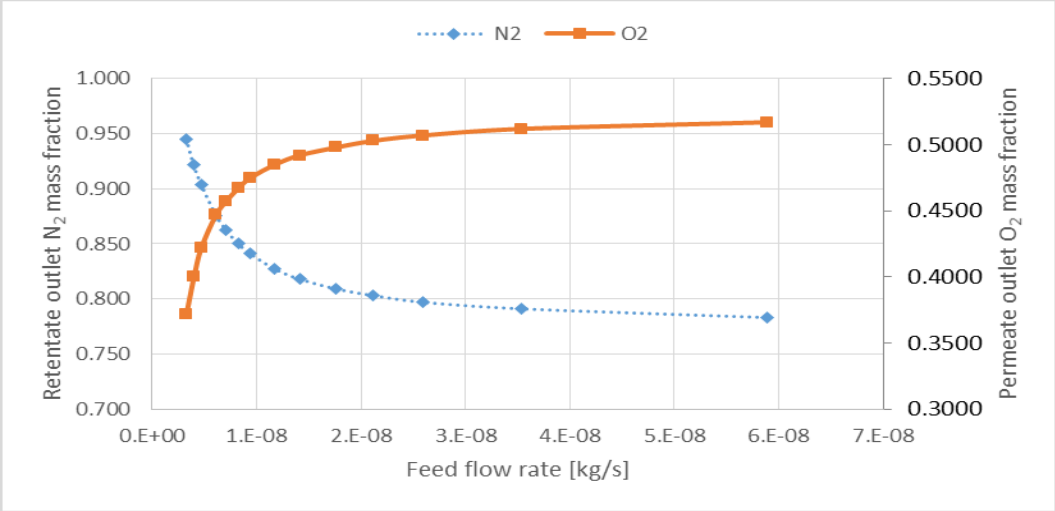

Figure 19: Distributions of mass fractions of O_2 and N_2 at permeate outlet and retentate over a range of feed flow rate at 6.8 atm feed pressure, 1 atm permeate pressure, and zero sweep flow rate.

4.1.3 Effect of Feed Pressure

One of the main advantages of polymeric membranes over ceramic membranes is that the feed pressure can be raised with respect to the permeate pressure. This helps to get higher partial pressure of oxygen in the feed side and, thus, oxygen permeation flux is increased. Figure 20 shows the effect of increasing the pressure in the feed side on permeation fluxes of O_2 and N_2 at sweep gas flow rate of 1.15×10^{-9} kg/s. As shown in the figure, the permeation fluxes of O_2 and N_2 increase as the feed pressure increases. The relation between permeation flux and feed pressure seems to be linear, as the permeability is constant with the pressure. The feed pressure governs the permeation flux relation, and this could be clear if the permeation flux equation was rewritten as follows:

$$J = \frac{P\ A\ (p_1 y_1 - p_2 y_2)}{L} \quad (19)$$

Where the partial pressures in the feed and the permeate sides are defined as $p' = y_1\, p_1$, and $p'' = y_2\, p_2$. Where p_1 is the total pressure in the feed side, and y_1 is the mole fraction of a specific gas in the feed gas while p_2 and y_2 are the pressure and the mole fraction at the permeate side. While P, A, and L are constants, and for firm pressure on the permeate side, then the permeation flux is mainly a linear function of feed pressure as presented in Figure 20. As the sweep gas flux is greater than the value at which O_2 flux exceeds that value of N_2 flux, 0.25×10^{-9} kg/s, O_2 flux is higher than N_2 flux at all pressure as shown in Figure 20. Due to the increase of O_2 permeation flux, while increasing the feed pressure, the concentrations of O_2 near membrane surface in the feed side are reduced as presented in Figure 21. Also, as shown in the figure, the concentrations of O_2 are reduced toward the retentate exit section on the fed side due to permeation of O_2 through the whole length of the membrane.

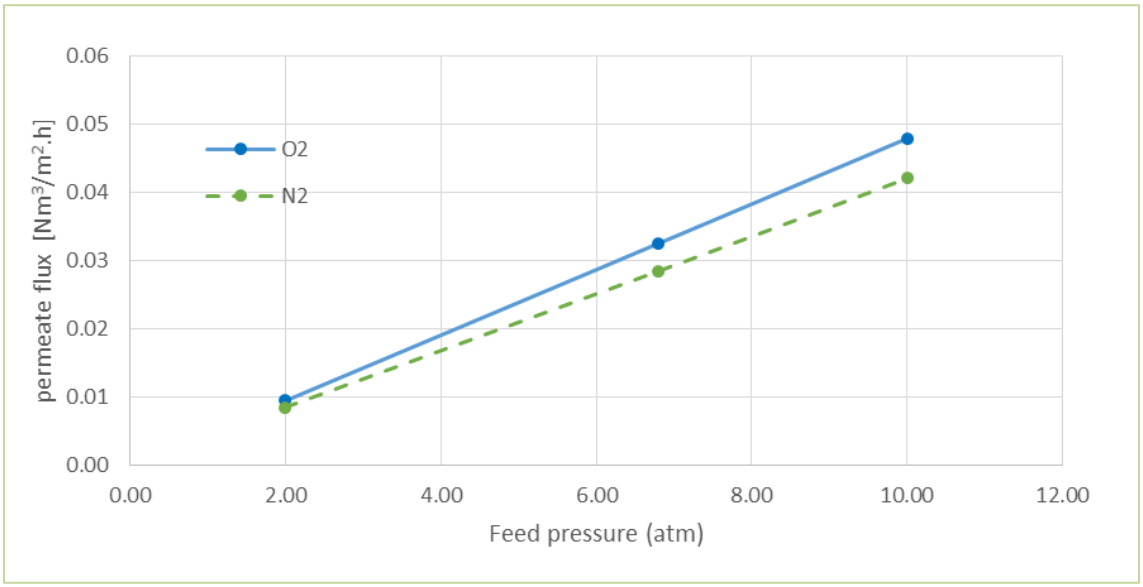

Figure 20: Total permeate flow rate for O_2 and N_2 as function of feed pressure at 1 atm permeate pressure, 5.89×10^{-8} kg/s feed flow rate and 1.15×10^{-9} kg/s sweep flow rate.

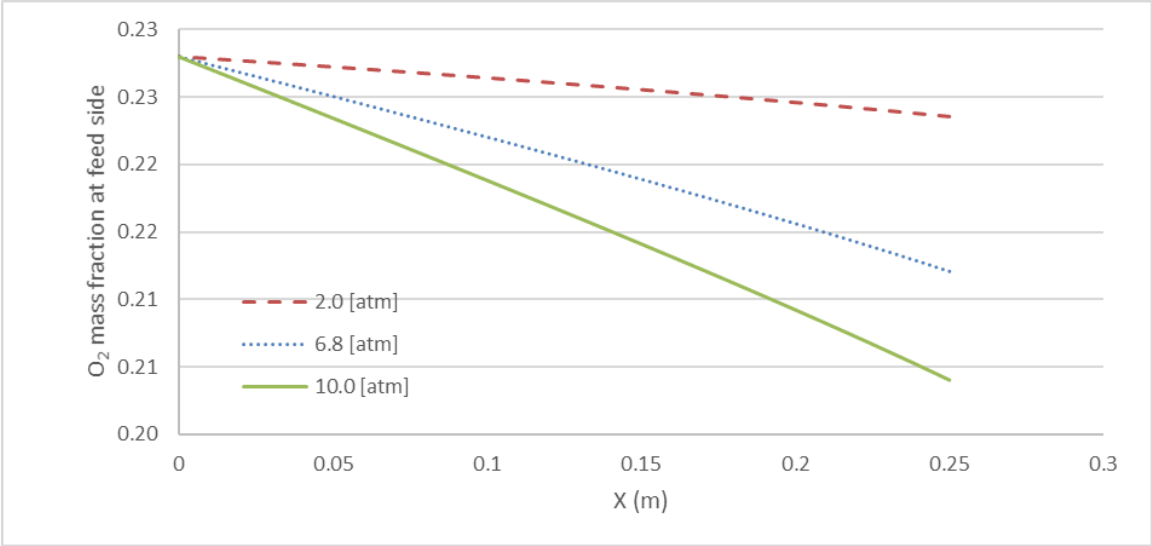

Figure 21: O_2 mass fraction at feed side along the membrane surface over a range of feed pressure at 1 atm permeate pressure, 5.89×10^{-8} kg/s feed flow rate, and 1.15×10^{-9} kg/s sweep flow rate.

4.1.4 Effect of Polymer Material

Different polymeric membranes can produce variant oxygen permeation fluxes depending on membrane material and feed gases. To study the effect of membrane material in terms of permeability and selectivity on O_2 permeation flux, three different polymeric membranes are considered in this study. The considered polymeric membrane materials s are TR- PBO-co-PPL 28, TR- PI-g-CD 450, in addition to the main studied hollow fiber membrane fabricated by Feng et al. [40]. The properties of the three polymeric membranes are presented in Table 6. For clarity, 1 GPU is equal to 3.35 x 10^{-10} mol/(m^2 s Pa) or equal to 10^{-6} cm^3 (STP)/(cm^2 s cmHg) and 1 Barrer is equal to 10^{-10} cm^3 (STP) cm /(cm^2 s cmHg). Based on that, GPU is defined as the permeability (in Barrer) per unit membrane thickness (in μm). In Ref. [40], the permeability of O_2 is equal to 132 Barrer for a membrane having a thickness of 40 μm and, based on that, the permeance in GPU is calculated to be equal to 3.3 (132/40) GPU.

Table 6: Properties of selected polymeric membranes.

Membrane	TR- PBO-co-PPL 28	TR- PI-g-CD 450	Feng et al. [21] fiber membrane
Permeance (O_2) GPU	3.3	67.67	9.3
Permeance (N_2) GPU	0.45	13.08	1.8
Selectivity (α_{O_2/N_2})	7.3	5.17	5.17
Reference	[74]	[75]	[40]

Figure 22 shows the distributions of stage cut (total permeation flow rate of O_2 plus N_2 divided by total feed flow rate) versus the separation factor, SF, (the ratio of O_2 to N_2 mass fraction in permeate-side divide by that ratio in feed-side) at zero sweep gas flow rate for the considered three polymeric membranes. Some of the results could be

expected from those inputs in Table 6; however, for a better understanding of the permeation performance of different membrane materials, the distributions of oxygen mass fractions at permeate outlet for various membranes are presented in Figure 22. As shown in Figure 22, oxygen mass fractions at permeate outlet for Feng et al. [40] fiber membrane and for TR- PI-g-CD 450 membrane are much different while they have the same selectivity, this is due to the higher permeation in TR- PI-g-CD 450 case, thus, decreasing the O_2 partial pressure at the feed side will increasing N_2 partial pressure at the feed side then increase N_2 permeation. One can see that the highest O_2 mass fraction at permeate outlet (highest SF) and the lowest permeation flow rate (lowest stage cut) are obtained by the TR- PBO-co-PPL 28 membrane. This is because the TR- PBO-co-PPL 28 membrane has the highest selectivity and the lowest permeability of the considered three membranes, while the TR- PI-g-CD 450 membrane gives the highest permeation flow rate (highest stage cut) and the lowest O_2 mass fraction at permeate outlet (lowest SF). This can be attributed to the relatively high permeability and low selectivity of this membrane. The main considered hollow fiber membrane in this study, membrane by Feng et al. [40], gave moderate results regarding the permeation flow rate and O_2 mass fraction at permeate outlet as shown in Figure 22. So, depending on the required gas to be separated at required flow rate and concentration, a suitable polymeric membrane material can be selected.

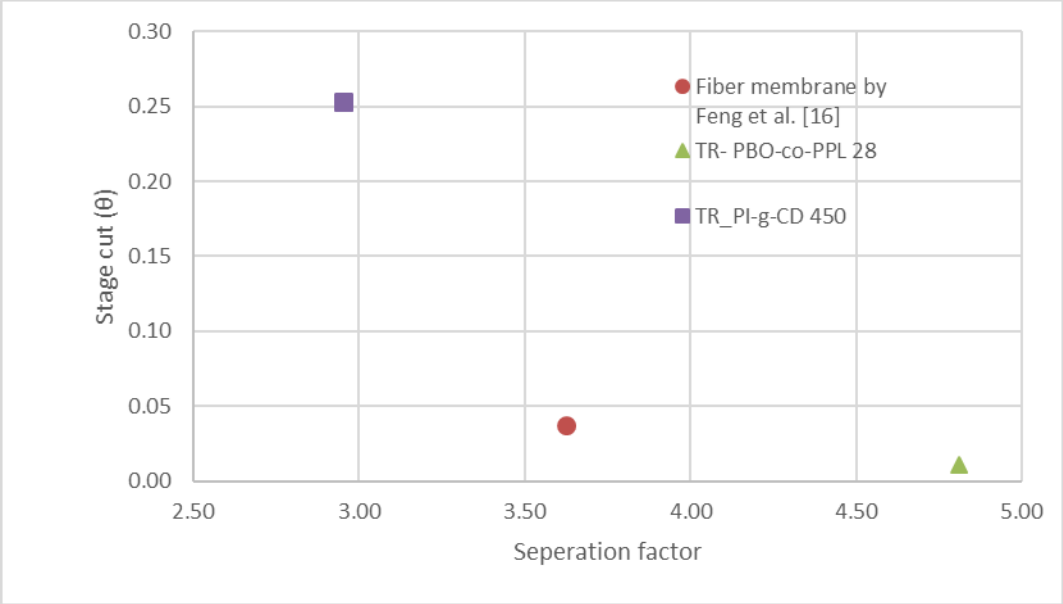

Figure 22: Stage cut against the separation factor at 6.8 atm feed pressure, 1 atm permeate pressure, 5.89×10^{-8} kg/s feed flow rate and zero sweep flow rate.

4.1.5 Multi-Stage Separation

The aim of using polymeric membranes for oxygen separation is to increase oxygen concentration in air for oxygen-enriched air combustion application. If a certain high oxygen concentration is targeted for a specific application, multi-stage separation using polymeric membrane units is required to achieve the necessary high oxygen concentration. In this case, oxygen-enriched air mixture leaving the first unit from the permeate side is introduced to the second unit as feed flow. In this study, multi-stage gas separation is performed numerically considering three stages as presented in Figure 23 at zero sweep gas flow rate. All considered fiber membranes in all stages are identical in terms of the size based on the design shown in figure 6. The first stage consists of two parallel multi-membranes units; each unit consists of 10 fiber membranes running in parallel. Air (with O_2 mass fraction of 0.228 and N_2 mass fraction of 0.772) is fed to the

first stage. The feed flow rate for each fiber membrane in the first stage is 5.89×10^{-8} kg/s at zero sweep flow rate. Numerical simulations of oxygen permeation across one fiber membrane showed oxygen mass fraction of 0.517 at permeate outlet of the first stage. The permeate flow at the outlet of each unit in the first stage, with O_2 mass concentration of 0.517 and N_2 mass concentration of 0.483, is supplied as the feed flow to another membrane unit in the second stage as shown in Figure 23. The second stage consists of two parallel membrane units; each unit consists of only one fiber membrane. The simulations at zero sweep gas flow rate of the second stage showed oxygen fraction of 0.8 at permeate outlet of the second stage. The final stage consists of one fiber membrane unit fed by the permeate flow out of the two parallel membrane units in the second stage. Calculations are performed considering zero sweep flow rate and the results showed oxygen fraction of 0.914 at permeate outlet of the third stage.

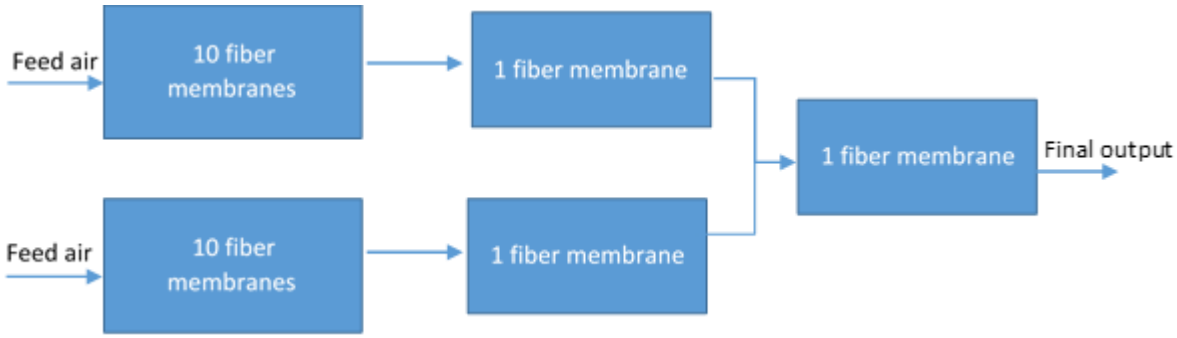

Figure 23: Configuration of the multi-stage separation unit.

For all simulations, only one fiber membrane is considered in each stage. Figure 24 shows the stage cut of one fiber membrane cell against the gained O_2 mass fraction at permeate outlet of one fiber membrane cell in each stage. Also, Figure 25 represents the feed flow rate against stage cut for one fiber membrane in each stage. However, each membrane cell in the first stage is fed by the highest feed gas flow rate as compared to

the flow rates in the second and the third stages (see Figure 25), the lowest O_2 permeation flux (lowest stage cut) is obtained in the first stage as shown in Figure 24. This can be attributed to the relatively low O_2 mass fraction in the feed side in the first stage as compared to the second and the third stage. Thus, the driving force for O_2 permeation is reduced and, accordingly, oxygen permeation flux is reduced. So, higher stage cut is gained in the third stage as shown in Figure 25 because of the high permeation flow rate relative to the feed flow. Better results can be obtained by recycling the retentate flows of the third and second stages to the feed side in the first stage as those retentate flows have higher O_2 mass fractions than normal air introduced in the first stage. A similar approach for recycling the retentate gases to the first stage was suggested by Katoh et al. [76].

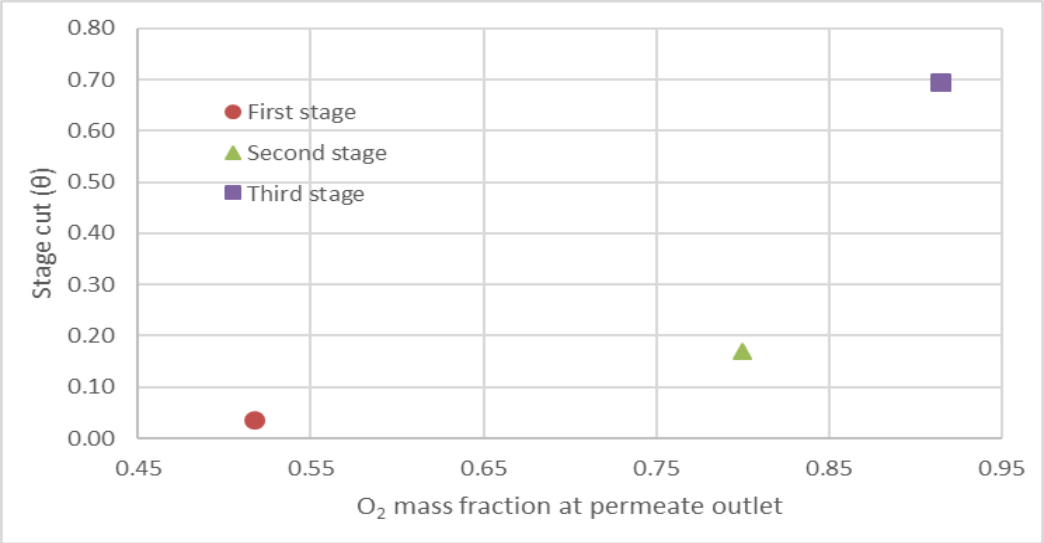

Figure 24: Stage cut versus O_2 mass fraction at permeate outlet for the series of the three stages at 6.8 atm feed pressure, 1 atm permeate pressure, zero sweep flow rate, and varying feed flow rates.

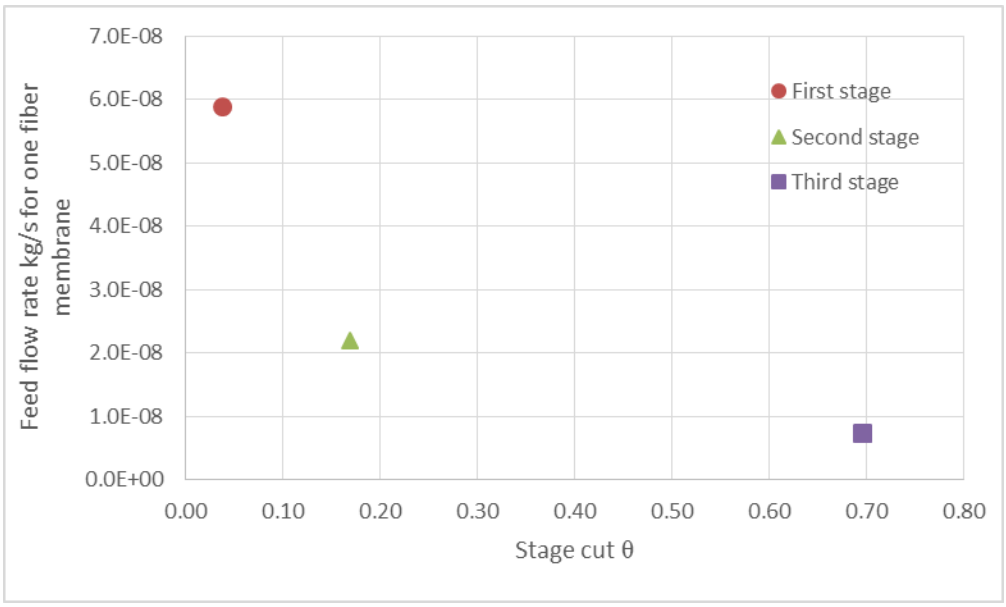

Figure 25: Stage cut against feed flow rate for series of the three stages at 6.8 atm feed pressure, 1 atm permeate pressure, zero sweep flow rate, and varying feed flow rates.

4.2 Hybrid System Simulation Results and Discussion

The outputs of the polymeric membrane model were used as inputs to the OTR to build the hybrid system. Table 7 shows the inputs and the outputs of one fiber polymeric membrane, which fed by atmospheric air; these outputs (oxygen enriched air) have been used as inputs to the OTR.

Table 7: Inputs and the outputs of one fiber polymeric membrane.

Polymeric membrane	Area (m^2)	Feed flow rate (kg/s)	Feed pressure	O_2 mass fraction at permeate outlet	Permeate flow rate (kg/s)
TR- PI-g-CD 450	1.26×10^{-4}	2.35×10^{-7}	10 atm	0.525	2.56×10^{-8}

Figure 26 shows the contours of temperature, O_2 mass fraction, and CH_4 mass fraction of the OTR; which fed (in this case) by oxygen enriched air (0.525 O_2 mass fraction) and

5.0×10^{-6} kg/s feed flow rate. The feed flow rate of this OTR is the permeate flow rate of more than one fiber polymeric membrane, where the permeate flow rate of one fiber membrane is 2.56×10^{-8} kg/s of oxygen enriched air (0.525 O_2 mass fraction). Temperature contours (Figure 26, a) show that the flame temperature reaches 2050 K, with an increase of 800 K from the inlet temperature. Moreover, because of the high thermal conductivity of the OTM, the outlet temperature for both the feed outlet and the sweep outlet are similar (around 1925 K). This high temperature capable to destroy the OTM, therefore lower temperature could be achieved by reducing the burned fuel amount as will illustrate subsequently. However, theoretically, the oxy fuel combustion process in the OTR is assumed to stand this relatively high temperature.

O_2 mass fraction (Figure 26, b) shows the oxygen depletion at the feed side, where O_2 mass fraction reduce from the oxygen enriched level (0.525 O_2 mass fraction) to oxygen depleted air (lower than 0.10 O_2 mass fraction). The reduction of O_2 mass fraction is a result of the oxygen permeation through the membrane, which increases as the partial pressure difference and the membrane temperature increase.

At the sweep side, CH_4 is consumed at the combustion zone, and its mass fraction is reduced from 0.25 to zero (Figure 26, c). While the oxygen is permeated through the membrane to react with the fuel, and the reaction products (H_2O and CO_2) keep a low level of oxygen partial pressure that also consumed during the combustion process. Downstream the flame region, because of the high membrane temperature and O_2 partial pressure difference of the oxygen across the membrane, still, the permeation through the membrane proceeds. As all CH_4 has been consumed by the reaction, the permeated O_2 will cause an increase of O_2 mass fraction at the sweep side (Figure 26, b). The existence

of oxygen at the sweep outlet is not preferable, because at oxy-fuel combustion applications CO_2 and H_2O should be at the exhaust only, and the presence of other gases will cause to an ineffective oxy-fuel combustion process.

To solve this issue, just the stoichiometric amount of O_2 should permeate to the sweep side, to establish for a complete combustion without any excess of O_2. If all fed oxygen will permeate from the feed side to the sweep side of the OTR, the stoichiometric ratio of CH_4 and O_2 reaction could be calculated as following:

$$OF = \frac{\dot{m}_{O_2}}{\dot{m}_{CH_4}} \quad \text{, where: } \dot{m}_{CH_4} = X_{CH_4}\dot{m}_{Sweep}, \quad \text{and } \dot{m}_{O_2} = X_{O_2}\dot{m}_{Feed} \tag{20}$$

Where OF is the oxygen to fuel ratio, and the stoichiometric oxygen to fuel ratio is equal to 4 in this reaction ($OF_{stoich} = 4$). For a known sweep flow rate, swept CH_4 mass fraction, and fed O_2 mass fraction, the stoichiometric oxygen flow rate will be as following:

$$\dot{m}_{O_2,stoich} = 4\dot{m}_{CH_4} \tag{21}$$

Moreover, the stoichiometric feed flow rate could be calculated as following:

$$\dot{m}_{Feed,stoich} = \frac{\dot{m}_{O_2,stoich}}{X_{O_2}} = \frac{4\dot{m}_{CH_4}}{X_{O_2}} = \frac{4X_{CH_4}\dot{m}_{Sweep}}{X_{O_2}} \tag{22}$$

This relation could enable to calculate the stoichiometric feed flow rate, that will feed the sweep side with the stoichiometric oxygen amount without any excess of O_2 at the exhaust, this if the whole fed O_2 will permeate through the membrane to the sweep side. Another value would be defined here to find the ratio between the feed flow rate and the stoichiometric feed flow rate (equivalence ratio) as following:

$$\phi = \frac{\dot{m}_{Feed}}{\dot{m}_{Feed,stoich}} \tag{23}$$

This equivalence ratio (ϕ) would give a view of how the feed flow rate is far or close to the stoichiometric feed flow rate.

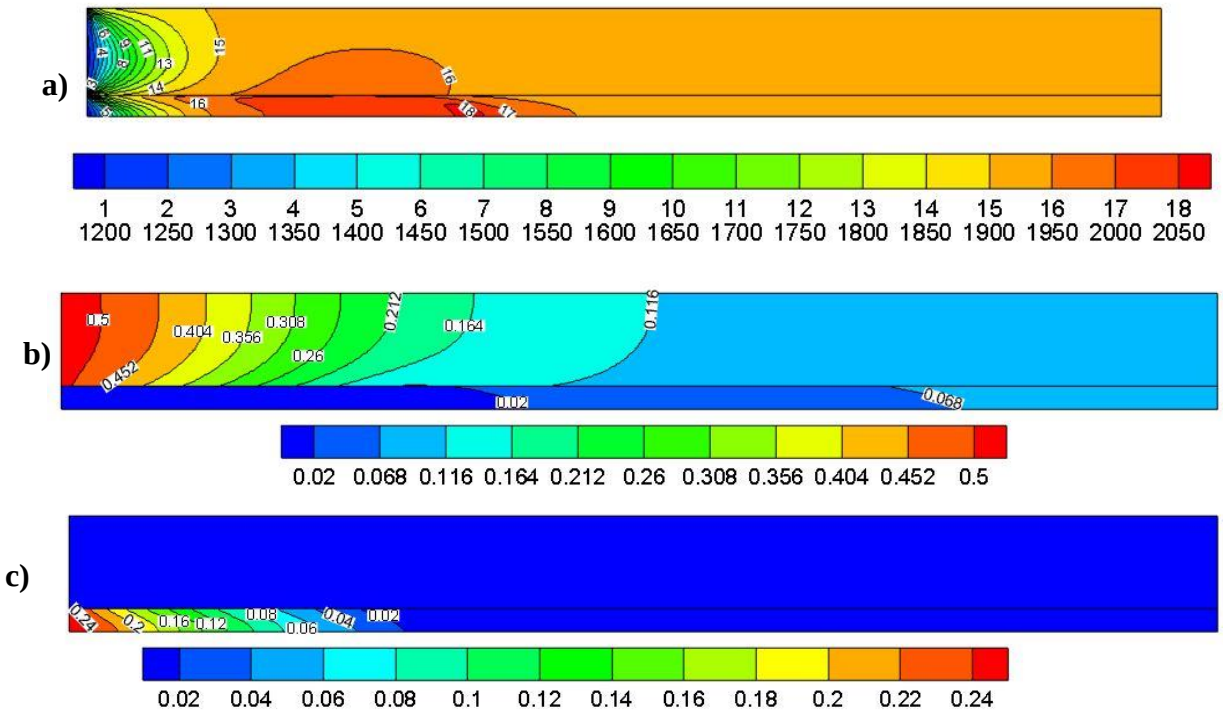

Figure 26: Contours of: a). Temperature (K), b). O_2 mass fraction, c). CH_4 mass fraction, at (5.0×10^{-6} kg/s feed flow rate with 0.525 O_2 mass fraction, 2.0×10^{-6} kg/s sweep flow rate with 0.25 CH_4 mass fraction and ϕ = 1.31).

Figure 27 shows a case with the same conditions of the previous case, but with stoichiometric feed flow rate (ϕ = 1.0). Stretched and lower temperature flame could be observed in this case, due to the lower permeation across the membrane comparing with the previous case. Figure 27, (b) shows that there is no excess of O_2 at both the sweep outlet and the feed outlet (less than 0.01 mass fraction). Also, complete combustion has been achieved, where all the CH_4 was burned. So, the solution of the exaggerate oxygen

at the sweep outlet could be solved by using stoichiometric feed flow rate (ϕ = 1.0). Another advantage of using this condition is the highly oxygen depleted air (higher than 0.95 N_2 mass fraction) at the feed outlet that could be used to produce high purity N_2.

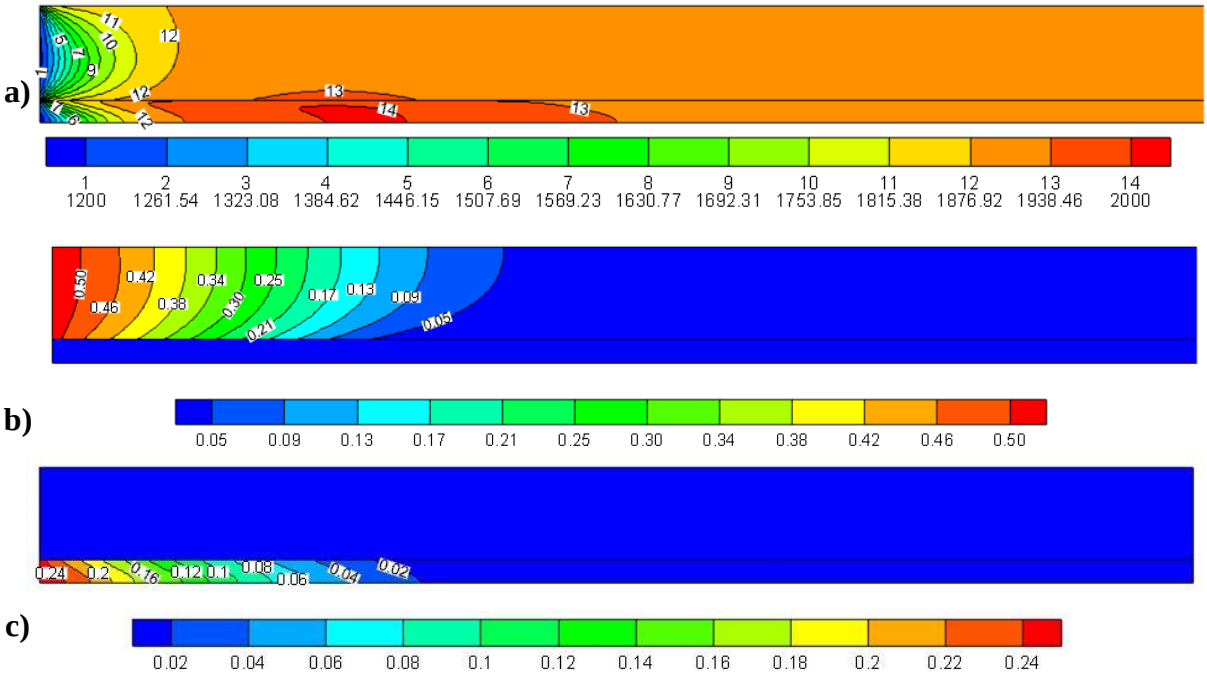

Figure 27: Contours of: a). Temperature, b). O_2 mass fraction, c). CH_4 mass fraction, at (3.81×10^{-6} kg/s feed flow rate with 0.525 O_2 mass fraction, 2.0×10^{-6} kg/s sweep flow rate with 0.25 CH_4 mass fraction, and ϕ = 1.0).

4.2.1 Effect of Fed O_2 Mass Fraction

The local permeations through the membrane length for different fed O_2 mass fractions are shown in Figure 28, (a). This distribution shows the various behaviors of the oxygen permeation with varying the fed O_2 mass fraction with same feed and sweep flow rates. 0.233 mass fraction (air) have the lower permeation level but with longer distribution along the membrane. While in 0.85 mass fraction, higher permeation was observed but

with shorter distribution. The increment decrease of permeation at a specific region of the membrane can be attributed to the increasing of the O_2 mass fraction at the sweep side after consuming all the CH_4. Figure 28, (b) shows O_2 mass fraction at the sweep side, 0.85 mass fraction fed O_2 has the higher permeation of O_2 through the membrane and the faster consumption of CH_4 (Figure 29, a), therefore the faster increasing of O_2 mass fraction at the sweep side (Figure 28, a). This increase of O_2 in the sweep side will increase the partial pressure at the sweep side then reduce the permeation through the membrane regarding the permeation equation (14).

The total permeation through the membrane for the same range of fed O_2 mass fractions is shown in Figure 30. The Higher flow rate has been achieved by increasing the fed O_2 mass fraction. This high permeation has two reasons. First, due to the higher O_2 partial pressure at the feed side, second, due to the higher membrane temperature of the 0.85 mass fraction (Figure 29, b). The increased membrane temperature as the fed O_2 fraction increase can be attributed to faster burned CH_4 with increasing O_2 permeation (at higher fed O_2 mass fraction) that will increase the flame temperature. Another reason for this higher temperature is the relatively higher specific heat of N_2 comparing with O_2 (figure 31), which will absorb more heat in the air case (higher N_2 mass fraction) comparing with the oxygen enriched air cases.

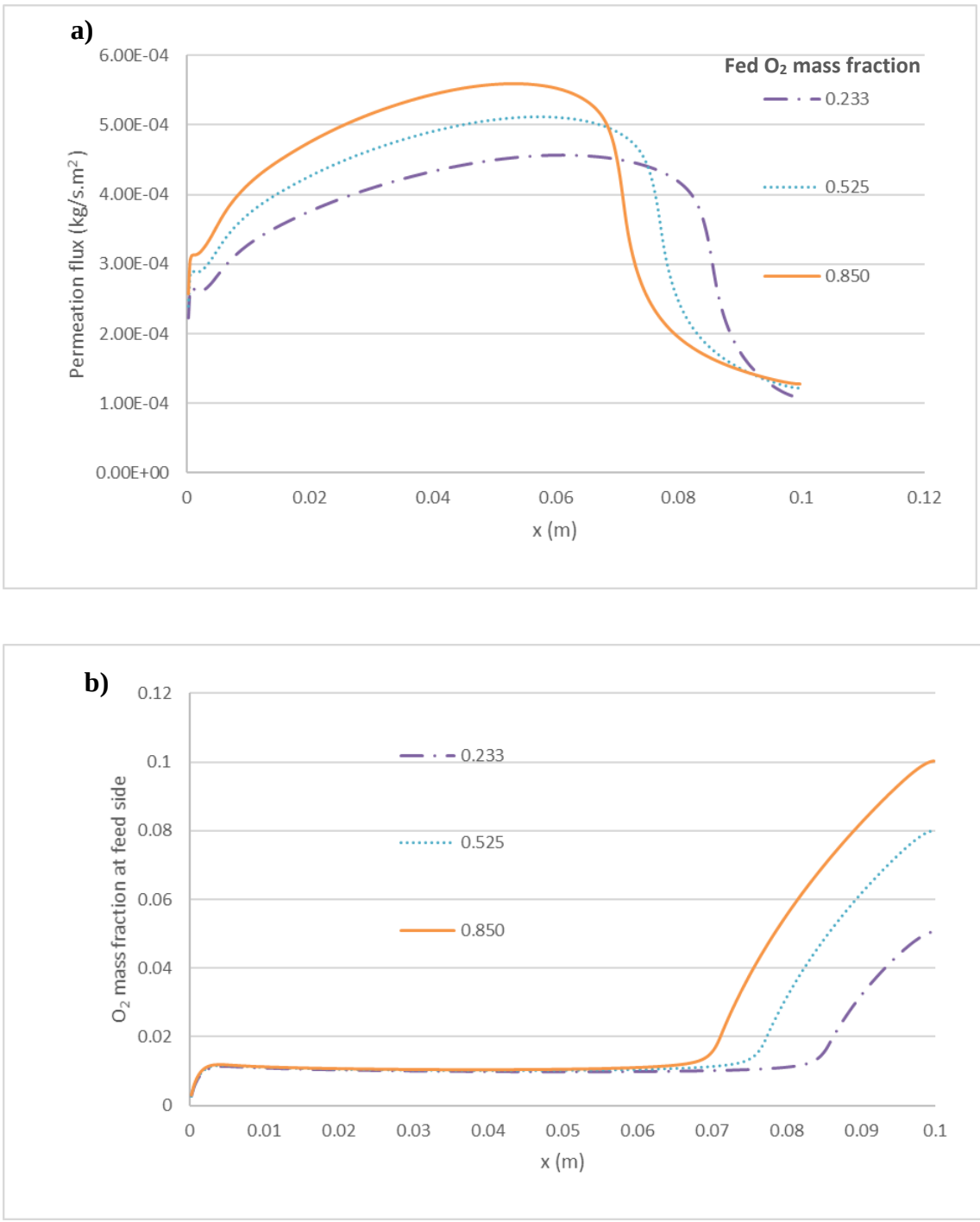

Figure 28: Distributions of a) permeate flux rates of O_2, and b) O_2 mass fraction at the feed side, over range of fed O_2 mass fractions at (5.0×10^{-6} kg/s feed flow rate, 2.0×10^{-7} sweep flow rate with 0.50 CH_4 mass fraction, and $\phi > 1.0$).

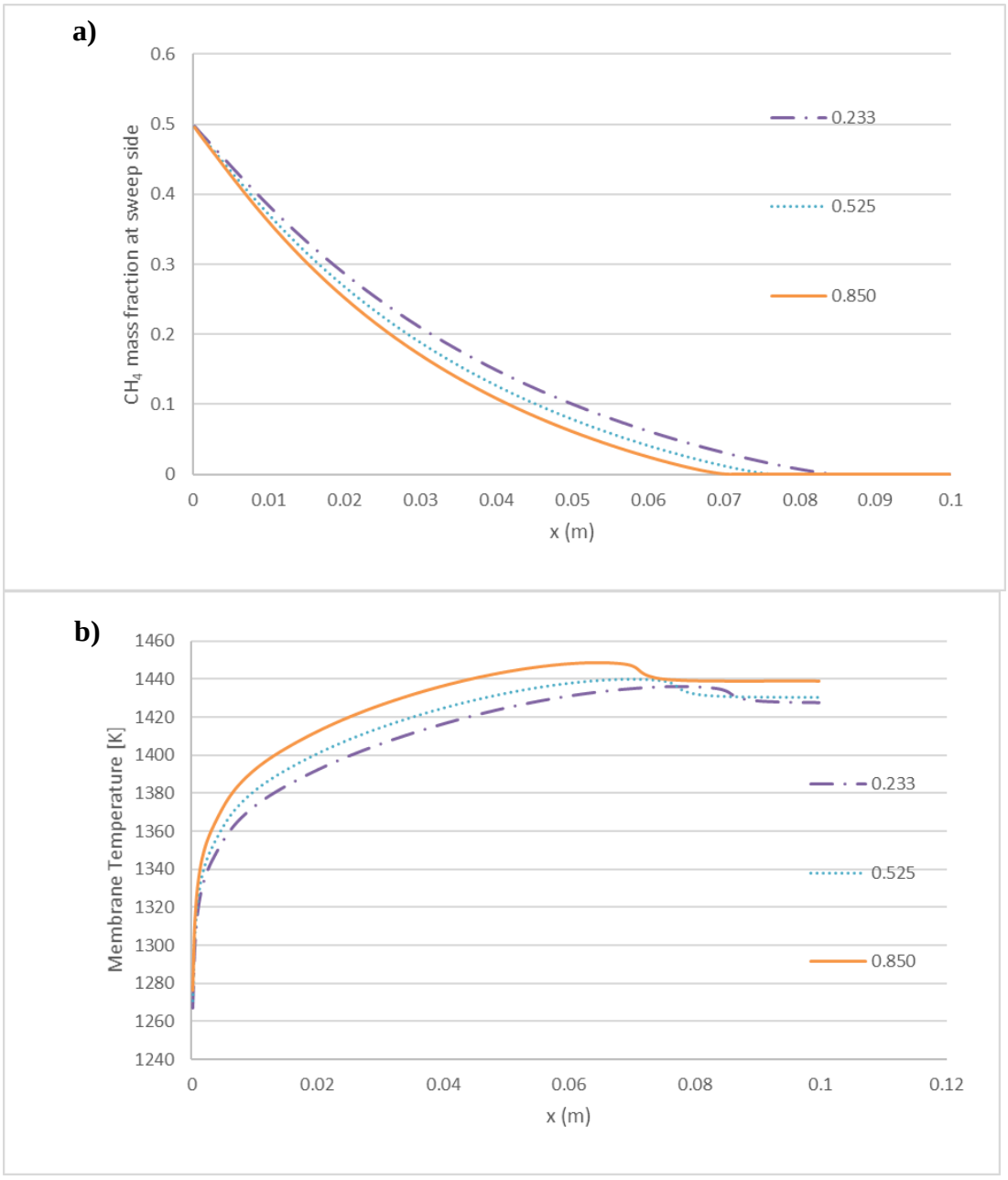

Figure 29: Distributions of a) CH_4 mass fraction at sweep side, and b) Membrane temperature, over range of Fed O_2 mass fractions at (5.0×10^{-6} kg/s feed flow rate, 2.0×10^{-7} sweep flow rate with 0.50 CH_4 mass fraction, and $\phi > 1.0$).

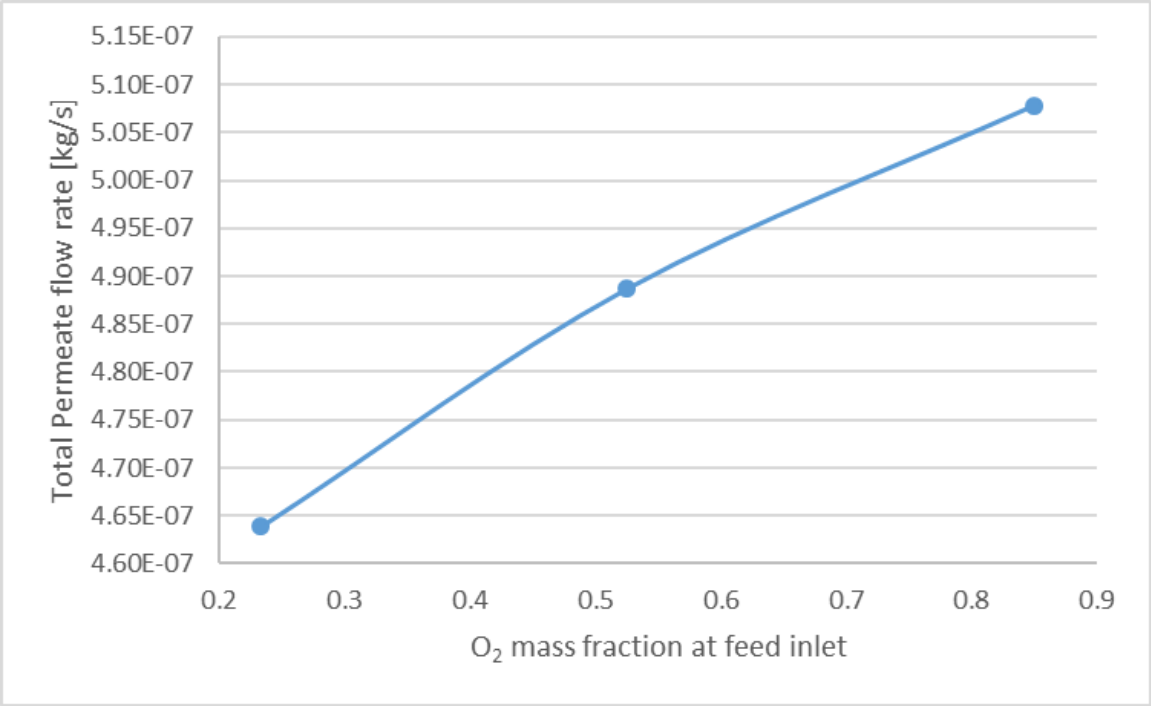

Figure 30: Distributions of total permeate flow rate of O_2 over a range of fed O_2 mass fractions at (5.0×10^{-6} kg/s feed flow rate, 2.0×10^{-7} sweep flow rate with 0.50 CH_4 mass fraction, and $\phi > 1.0$).

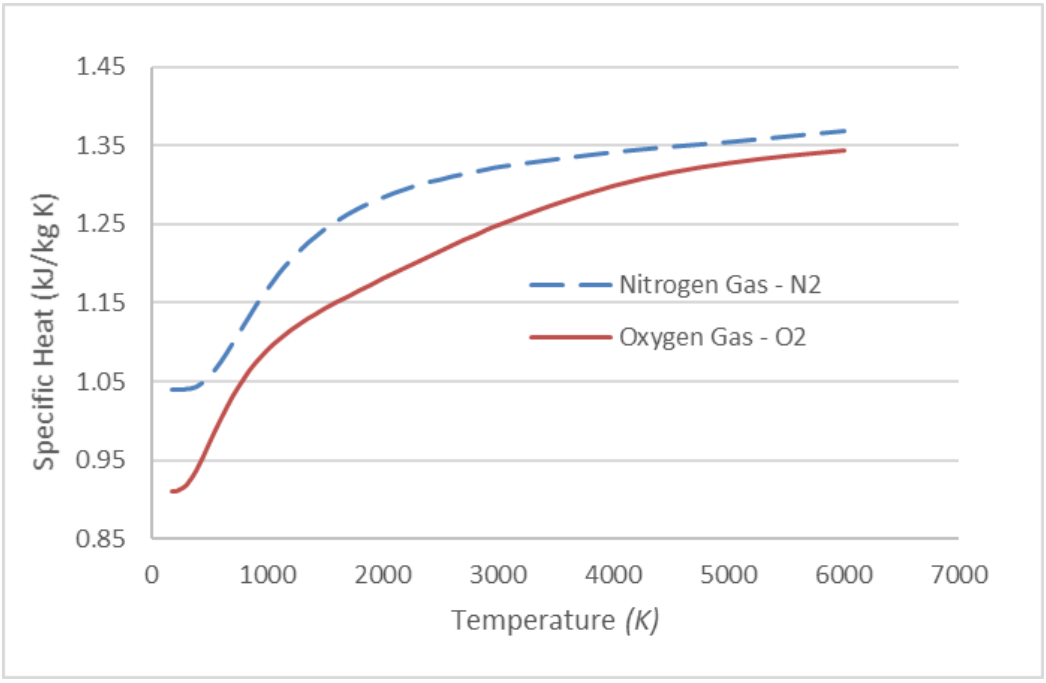

Figure 31: Specific heat of O_2 and N_2 at temperatures over a temperature range.

Comparing stoichiometric feed flow rate for both fed oxygen enriched air case and fed atmospheric air case could give an advantage of using the hybrid system. For example, for the same sweep flow rate and swept CH_4 mass fraction ($\dot{m}_{CH_4} = X_{CH_4}\dot{m}_{Sweep}$), and for 0.525 fed O_2 mass fraction ($\dot{m}_{O_2} = 0.525\dot{m}_{Feed}$), the stoichiometric feed flow rate could be calculated using equation (22); ($\dot{m}_{Feed,stoich} = 4\dot{m}_{CH_4} / 0.525$), This is the stoichiometric feed flow rate for 0.525 fed O_2 mass fraction. While if air (0.233 fed O_2 mass fraction) is fed instead of oxygen enriched air with the same sweep flow rate and swept CH_4 mass fraction; $\dot{m}_{Feed,stoich} = 4\dot{m}_{CH_4} / 0.233$.

So with the air fed case the feed flow should be higher than the oxygen enriched case by the ratio (0.525 / 0.233 = 2.25) to achieve the stoichiometric condition at the same CH_4 flow rate. This shows a major advantage of using oxygen enriched air in the feed side instead of the atmospheric air. Reducing the feed flow rate by using the oxygen-enriched air will reduce the pumping power of the feed stream, and the most important are reducing the preheating power consumed to heat the fed stream. Therefore, using the hybrid system would increase the cycle efficiency.

4.2.2 Effect of Swept CH_4 Mass Fraction

The fuel in oxy-fuel reaction could be diluted by CO_2 to prevent the high combustion temperature, which will be high with the absence of N_2 in the reaction. So, the effect of using CO_2 as dilute have been performed. Figure 32, (a) shows how the permeation increase with increasing the CH_4 mass fraction at constant total sweep flow rate

(increasing CH_4 flow rate; $\dot{m}_{CH_4} = X_{CH_4}\dot{m}_{sweep}$). This increase in the permeation flux is due to the higher membrane temperature (Figure 32, b) as the CH_4 fraction is increased. Higher CH_4 flux would reduce the flame length and increase its temperature, the reduction in flame length is due to the higher oxygen permeation that will consume all the fuel early (Figure 33, a) compared with the lower permeation cases (lower CH_4 fraction cases).

The rapid reduction of the permeation flux for the higher CH_4 mass fraction is attributed to the increase in the O_2 partial pressure at the sweep side; that permeated after the flame region. So, this permeated oxygen did not react with CH_4 because it has been consumed and will not transfer to CO_2 H_2O.

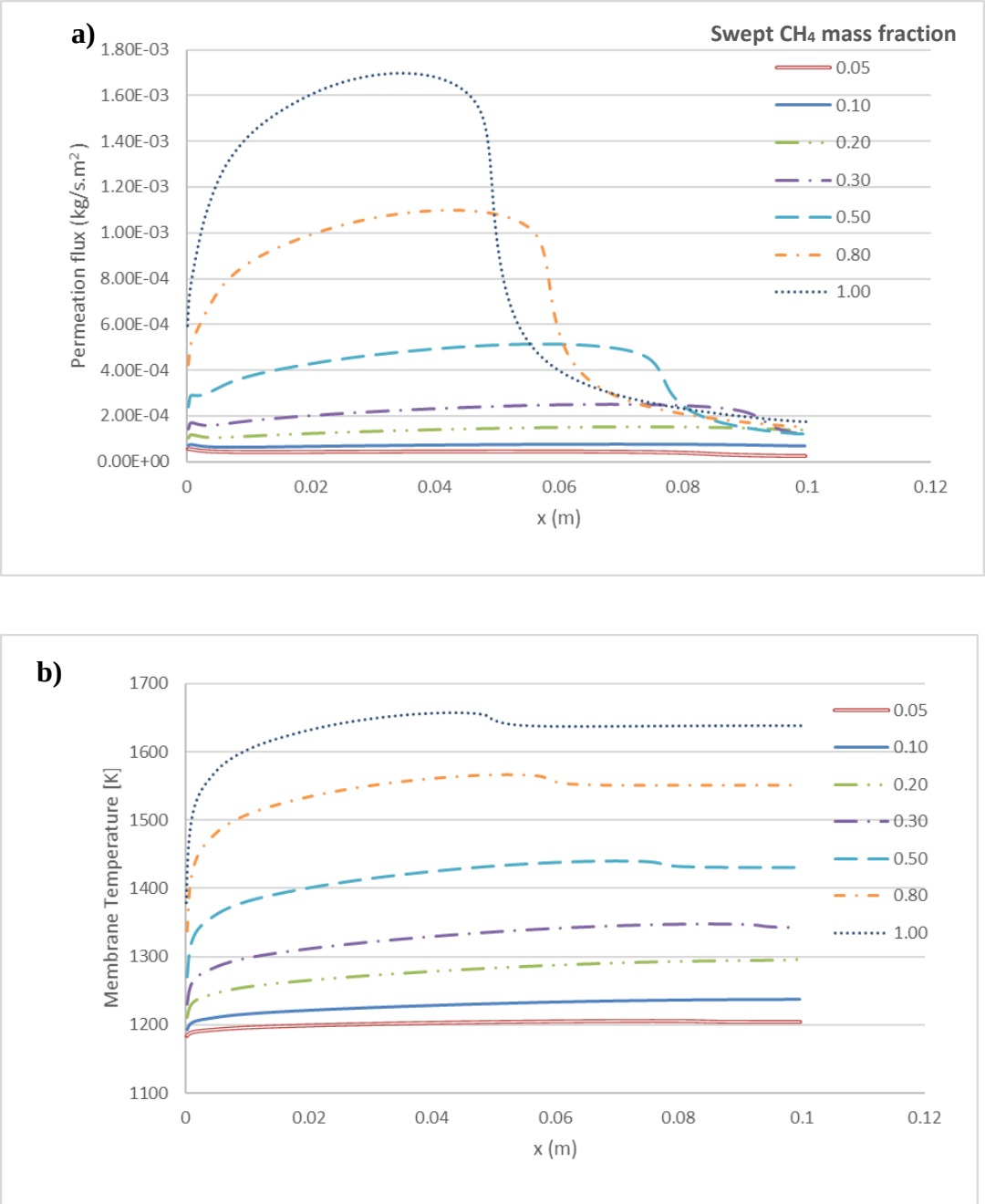

Figure 32: Distributions of a) permeate flux rates of O_2, and b) membrane temperature, over range of swept CH_4 mass fractions at (5.0×10^{-6} kg/s feed flow rate with 0.525 O_2 mass fraction, 2.0×10^{-7} kg/s sweep flow rate, and $\phi > 1.0$).

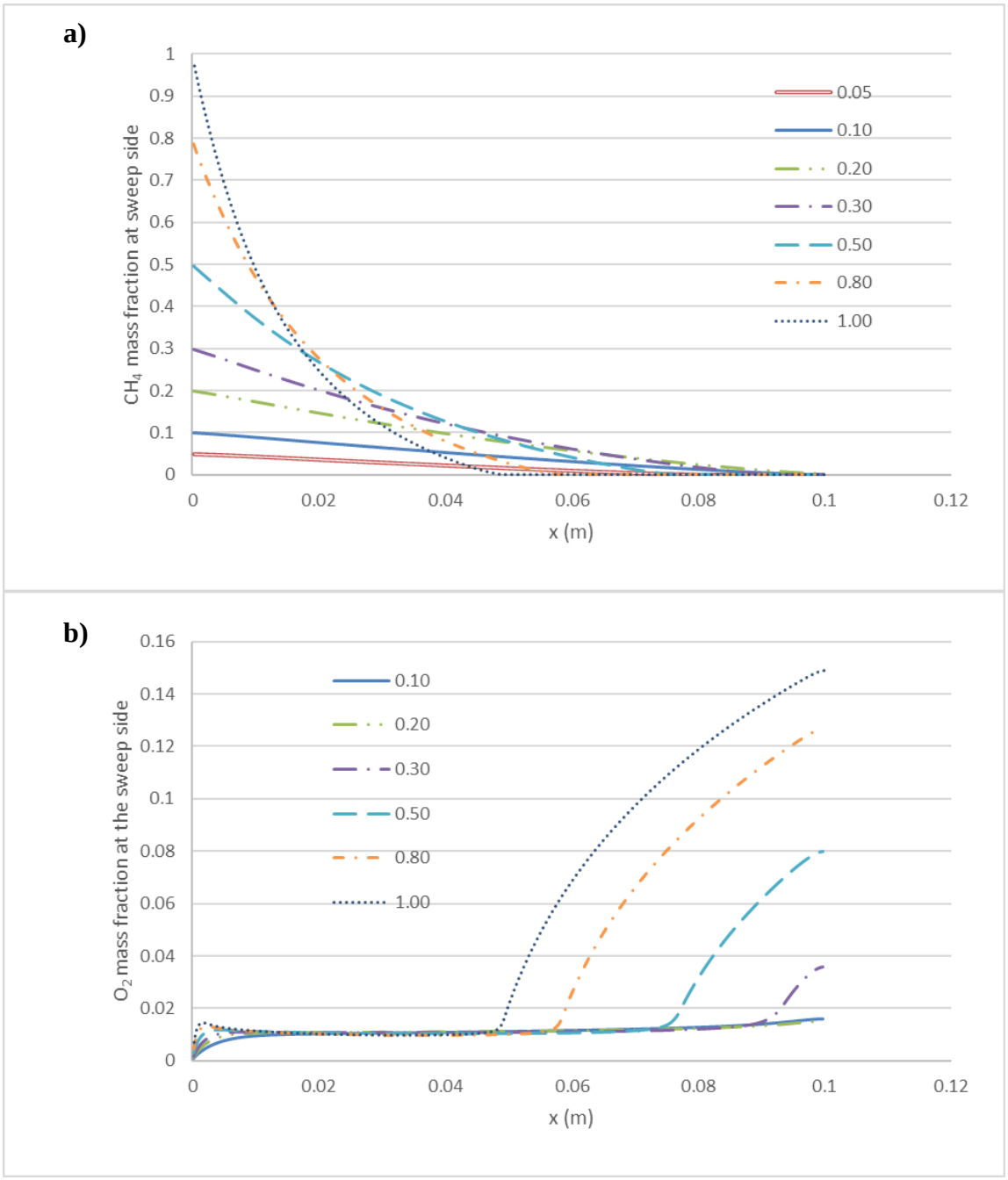

Figure 33: Distributions of a) CH_4 mass fraction, and b) O_2 mass fraction, at the sweep side, over range of over range of swept CH_4 mass fractions, at (5.0×10^{-6} kg/s feed flow rate with 0.525 O_2 mass fraction, 2.0×10^{-7} kg/s sweep flow rate, and $\phi > 1.0$).

Figure 34 shows the relation between the swept CH_4 mass fraction and the total permeated O_2 through the membrane. Increment increase of the total permeated O_2 could

be observed as the swept CH_4 increase. Each point of this plot is an integration of the area of a curve in Figure 32, (a). The disadvantage of using high CH_4 mass fraction is the very high temperature, which can damage OTR. Therefore, the swept CH_4 mass fraction could by diluted by CO_2 to reduce the combustion temperature to the safe side.

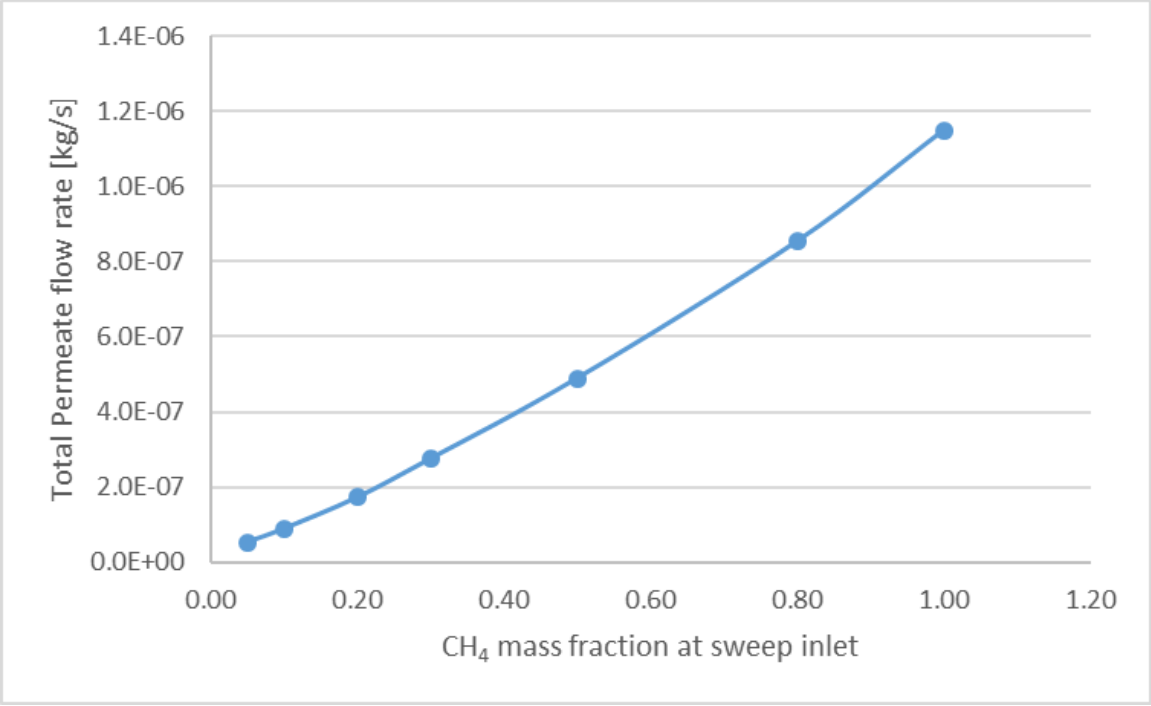

Figure 34: Distributions total permeate flow rates of O_2 over range of swept CH_4 mass fractions at (5.0×10^{-6} kg/s feed flow rate with 0.525 O_2 mass fraction and 2.0×10^{-7} kg/s sweep flow rate).

4.2.3 Effect of Feed Flow Rate

The fed oxygen enriched air could control the combustion products as described earlier. With low feed flow rates ($\phi < 1.0$) a rich combustion will take place, and fuel residual will be one of the reaction products, which is unacceptable in the oxy-fuel combustion process. Similarly, at the lean combustion ($\phi > 1.0$), the unreacted oxygen will be at the sweep outlet, which is undesirable in oxy-fuel combustion. To study the effect of lean

cases, and effect of superfluous feed flow rates, Figure 35 shows the local permeation flux through the membrane and the local membrane temperature for lean cases, higher temperatures are observed as reducing the feed flow rates; that will increase the local permeation. This higher temperature is due to the decrease of heat losses as the feed flow rate decrease. Figure 35, (a) shows that the higher permeation occurred with the lower feed flow rates at the reactor upstream, then it decreases sharply due to the completed combustion at the sweep side and increased O_2 mass fraction there (Figure 36). Incomplete combustion of the fuel at the cases of 1.05×10^{-5} kg/s and 1.2×10^{-5} kg/s feed flow rates (Figure 36, a) is observed, this because of the significant heat losses to these high feed flow rate, which cause to reduce the membrane temperature (Figure 35, a) and decrease the permeation of oxygen. Therefore, the lean combustion will persist as increasing the feed flow rate until reaching a point where the heat losses to the feed side prevent the complete combustion.

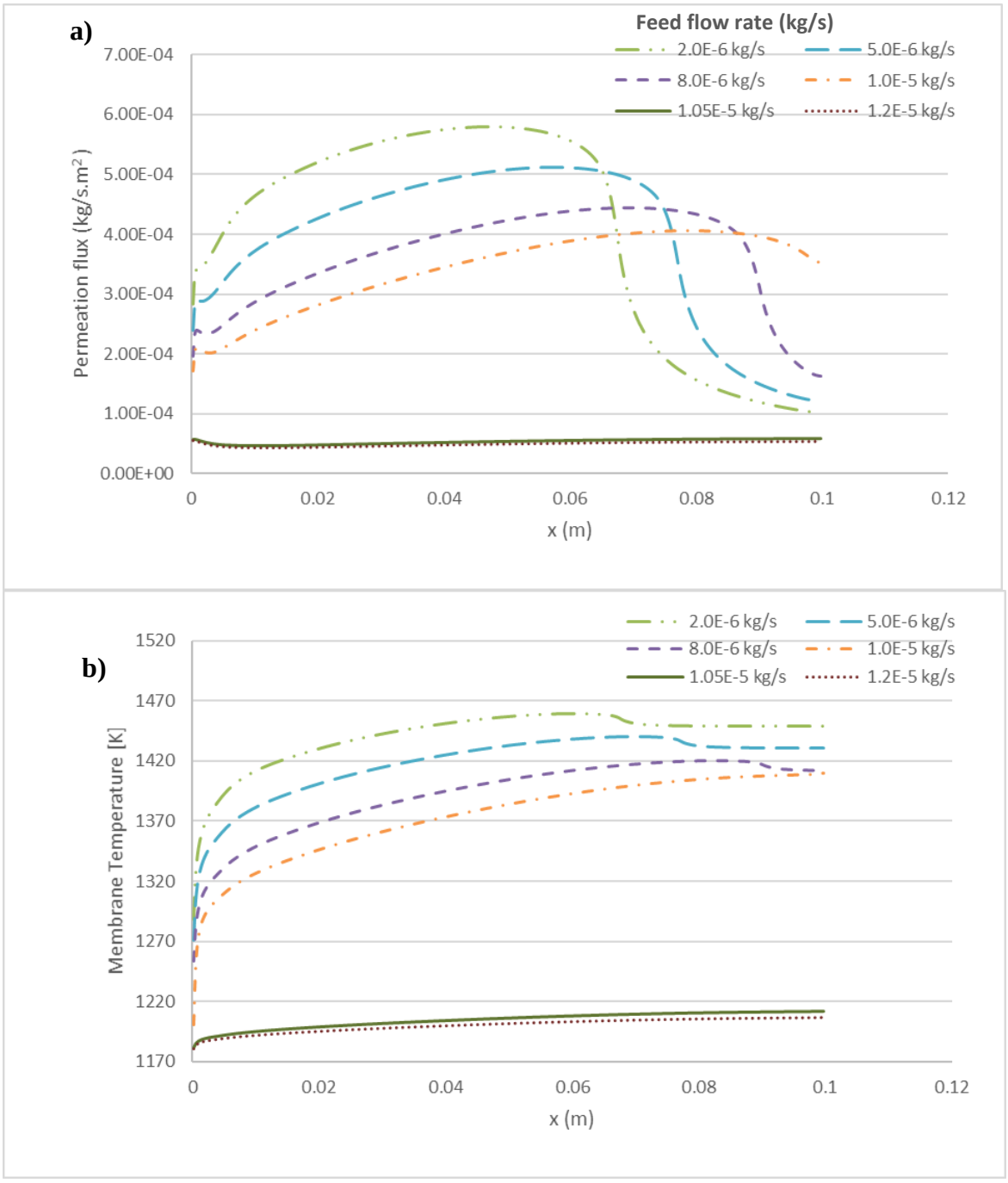

Figure 35: Distributions of a) permeate flux rates of O_2, and b) membrane temperature, over range of feed flow rates at (0.525 fed O_2 mass fraction, 2.0×10^{-7} kg/s sweep flow rate with 0.5 CH_4 mass fraction, and $\phi > 1.0$).

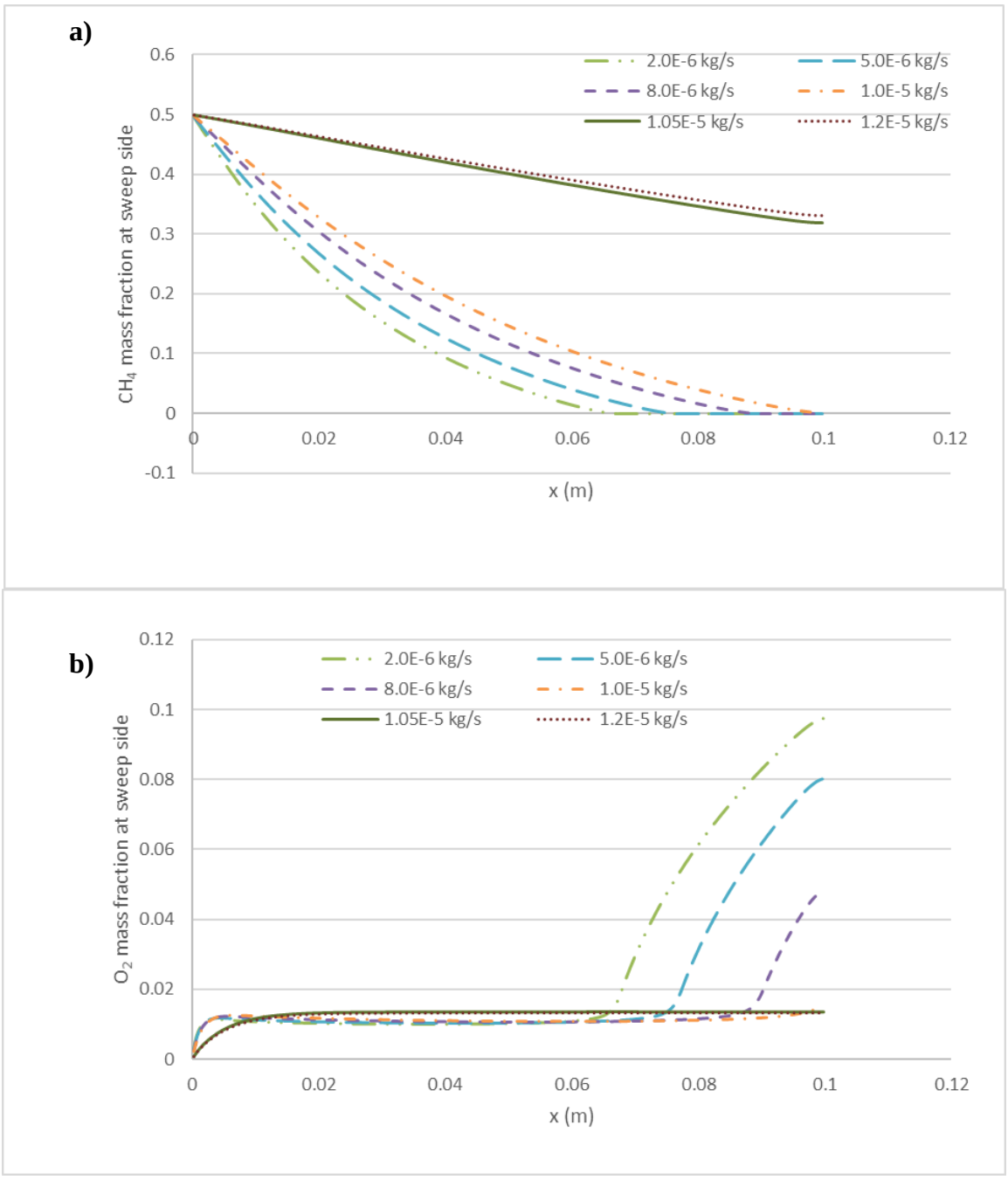

Figure 36: Distributions of a) CH_4 mass fraction, and b) O_2 mass fraction, at the sweep side, over range of feed flow rates at (0.525 fed O_2 mass fraction, 2.0×10^{-7} kg/s sweep flow rate with 0.5 CH_4 mass fraction, and $\phi > 1.0$).

As the produced flow rate from the polymer membrane is known (Table 7), and for specific feed flow rate, the total number of the fiber polymer membranes required to fed one tubular OTM could be calculated as following:

$$\mathrm{N} = \frac{\dot{m}_{Feed}}{2.56\times10^{-8}} \tag{24}$$

Where N is the required number of fiber polymer membrane to fed one tubular OTM, and one fiber polymer membrane production equal to 2.56-8 kg/s of oxygen enriched air (0.525 O_2 mass fraction). The ratio between the required fiber polymer membranes area to the OTM's area (R) could be defined as following:

$$R = \frac{N \times A_{polymer}}{A_{LCF}} = \frac{N \times 1.26\times10^{-4}}{1.26\times10^{-3}} = \frac{N}{10} \tag{25}$$

Where the area of one fiber polymer membrane is 1.26×10^{-4} m^2, While the area of one tubular OTM membrane area is 1.26×10^{-3} m^2. Therefore the total permeation of oxygen through the OTM could be distributed over a range of feed flow rates as shown in Figure 37). This distribution indicates that increasing the feed flow rates should reduce the total permeation gradually due to the heat losses until the permeation flux dropped suddenly at a flow rate between 1.0×10^{-5} and 1.05×10^{-5} kg/s. This abrupt drop of the oxygen permeation at very high feed flow rates can be attributed for the incomplete combustion at these higher flow rates. Therefore, using high feed flow rate will reduce the efficiency of this system by; requiring more fiber polymer membranes, and more preheating for the feed stream. So, using the stoichiometric feed flow rate is the only acceptable feed flow rate in this system.

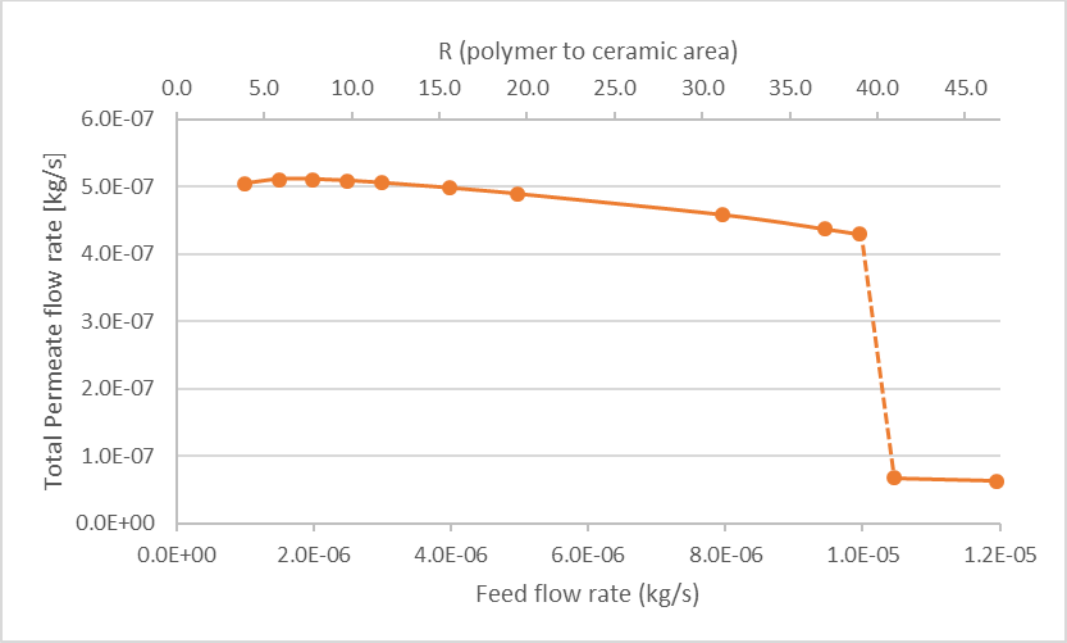

Figure 37: Distributions of total permeate flow rates of O_2 over range of feed flow rates at (0.525 fed O_2 mass fraction, 2.0×10^{-7} kg/s sweep flow rate with 0.5 CH_4 mass fraction, and $\phi > 1.0$).

4.2.4 Effect of Sweep Flow Rate

The local permeations through the membrane length for different sweep flow rates are shown in Figure 38, (a). This distribution shows the different behavior of the permeation with varying sweep flow rate while keeping the mass fraction of CH_4 and the other operation conditions constant. At low sweep flow rate, lower permeation level has been achieved but with longer distribution along the membrane. While with increasing the sweep flow rate, higher permeation was observed but with shorter distribution along the membrane. The increase in permeation as the sweep flow rate increases is attributed to the increase in the CH_4 flow rate that will burn at the sweep side. As the swept CH_4 flow

rate increase the flame temperature will increase (Figure 38, b), then the permeation will increase. The higher O_2 permeation will cause to burn the fuel earlier than the lower sweep rate cases (Figure 39, a). Another reason to the increase of O_2 permeation is the increase of the sweep flow rate itself, as the sweep flow rate increase the partial pressure of oxygen at the sweep side will decrease, then the permeation will increase depending on the permeation equation (14).

The sharp decrease of permeation at a specific region of the membrane (Figure 38, a) is attributed to the increased O_2 mass fraction at the sweep side (Figure 39, b) after consuming all CH_4. Figure 39, (b) shows O_2 mass fraction at the sweep side. Once can see that the higher sweep flow rates have the higher increase of the O_2 mass fraction at the sweep side, this happened due to the greater membrane temperature that allowed to permeate the oxygen to the sweep side until its partial pressure increase there and reduce the permeation rapidly.

The lower O_2 mass fraction is produced at the smaller sweep flow rate. However, as the sweep flow rate is reduced the power output will reduce because of decreasing the burned fuel. So, reducing the sweep flow rate is not a solution of the excess O_2 at the sweep outlet. The solution of this problem is by reducing the feed flow rate to the stoichiometric conditions while using the higher possible sweep flow rate.

Figure 40 shows the relation between the sweep flow rate and the total permeated O_2 through the membrane. Increment increase of the total permeated O_2 could be observed as the sweep flow rate increase. Each point of this plot is an integration of the area of a curve in Figure 38, (a). The main limitation of increasing the sweep gas flow rate is the

temperature rise as the sweep flow rate is increased. Thus, as the sweep flow rate can be increased more power would be produced (due to the increase of the burned CH_4), and this requires more stoichiometric feed flow rate ($\dot{m}_{Feed,stoich}$).

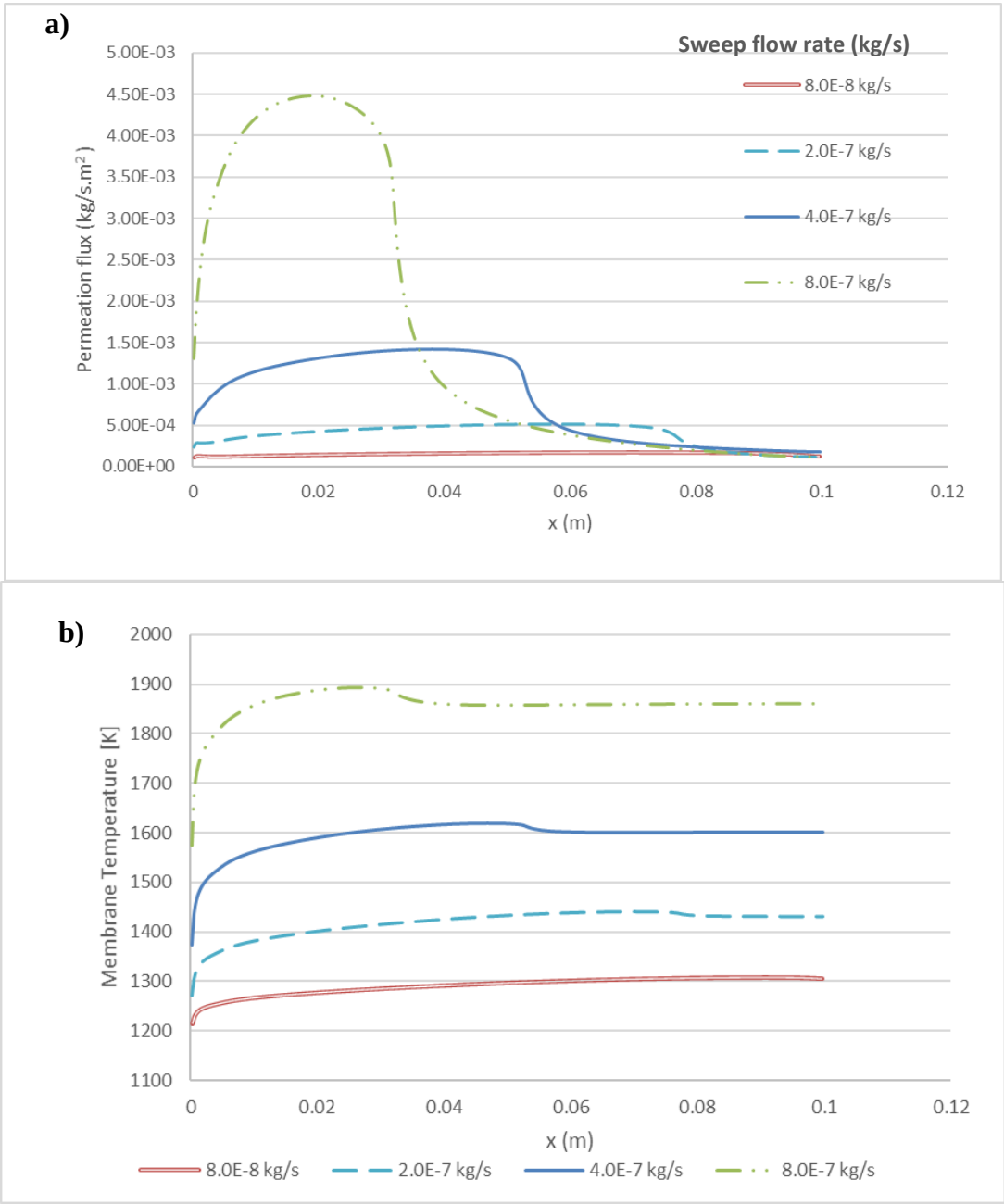

Figure 38: Distributions of: a) permeate flux rates of O_2, and b) membrane temperature, over range of sweep flow rates at (5.0×10^{-6} kg/s feed flow rate with 0.525 O_2 mass fraction, 0.50 CH_4 swept mass fraction, and $\phi > 1.0$).

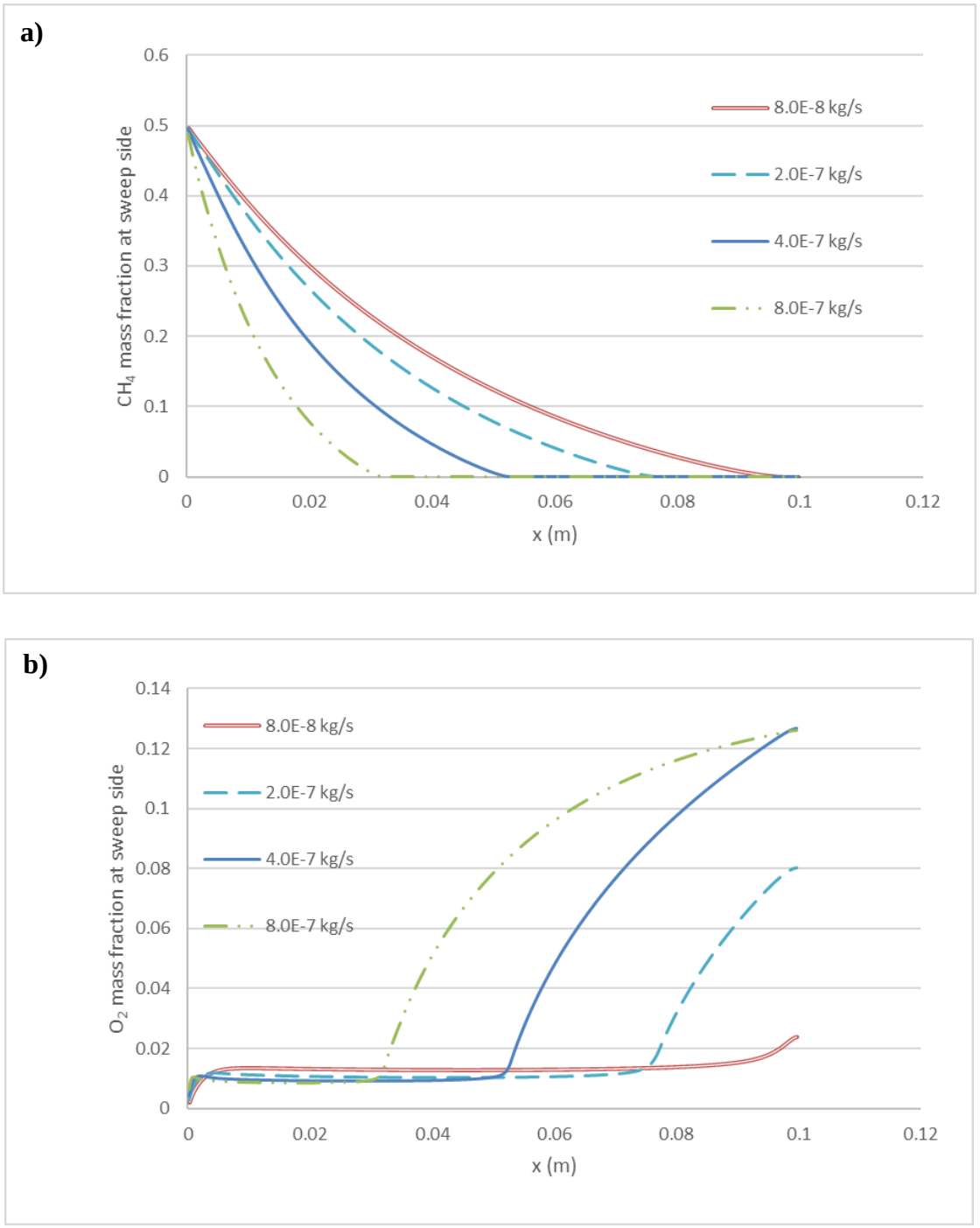

Figure 39: Distributions of: a) CH_4 mass fraction, and b) O_2 mass fraction, at the sweep side, over range of sweep flow rates at (5.0×10^{-6} kg/s feed flow rate with 0.525 O_2 mass fraction, 0.50 CH_4 swept mass fraction, and $\phi > 1.0$).

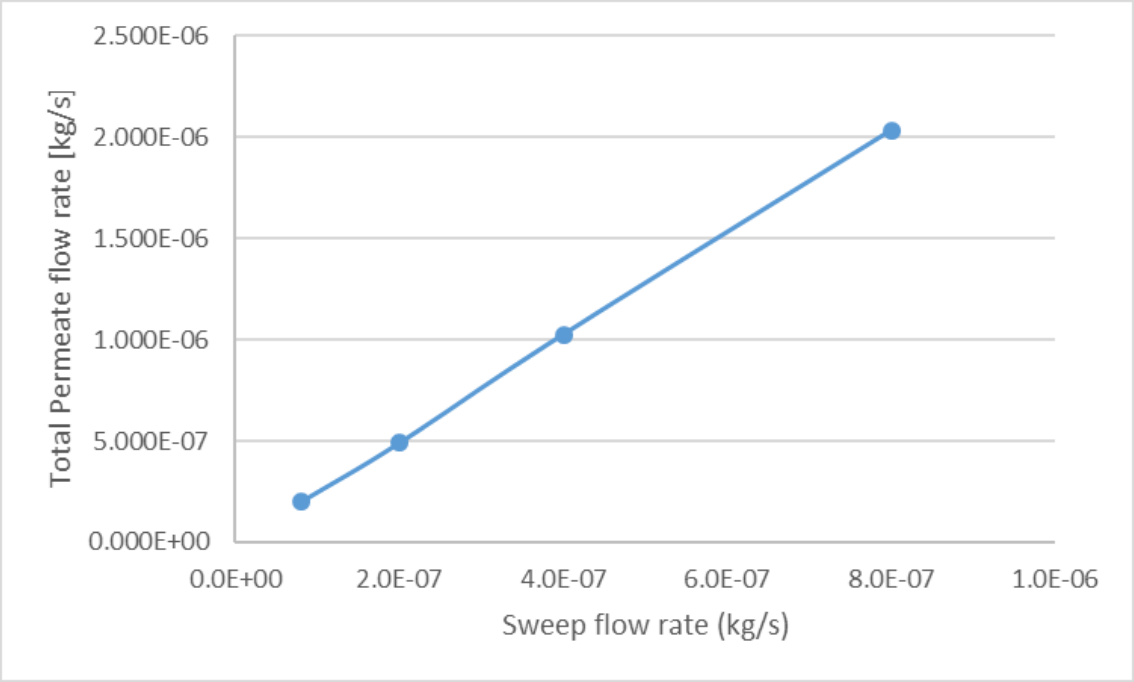

Figure 40: Distributions of total permeate flow rates of O_2 over range of sweep flow rates at (5.0×10^{-6} kg/s feed flow rate with 0.525 O_2 mass fraction, 0.50 CH_4 swept mass fraction, and $\phi > 1.0$).

Figure 41 shows the effect of the sweep gas flow rate on the oxygen permeation for different swept CH_4 mass fractions. Smaller swept CH_4 mass fractions produces lower flame temperature and increase the ability to use higher sweep flow rates. Therefore, lower permeation could be observed at the lower swept CH_4 cases, but comparing to the CH_4 mass flow rate, similar values of oxygen permeation were observed. Thus, lower membrane temperature can be realized by reducing the swept CH_4 mass fraction and increasing the sweep flow rate, in other word, keeping the same fuel flow rate and increasing the dilute flow rate.

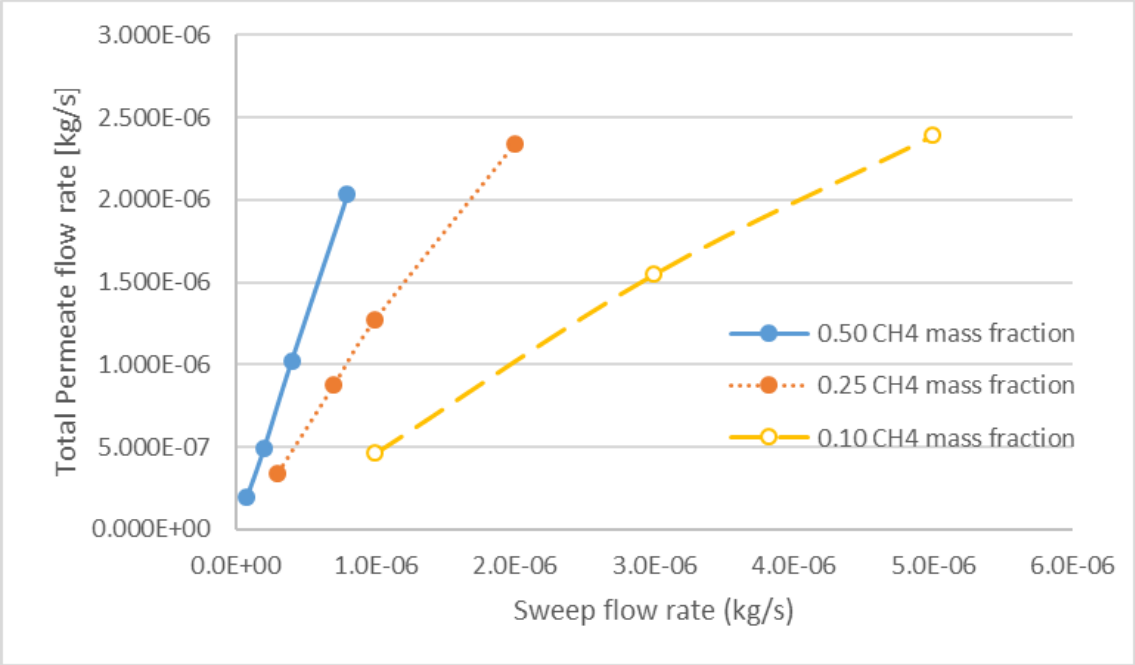

Figure 41: Distributions of total permeate flow rates of O_2 over range of sweep flow rates for different swept CH_4 mass fractions at (5.0×10^{-6} kg/s feed flow rate with 0.525 O_2 mass fraction, 0.50 CH_4 swept mass fraction, and $\phi > 1.0$).

4.2.5 Design and Energy Analysis

For stoichiometric cases, the ratio between the required polymer membrane area and the OTM membrane (R) could be calculated as following (using equations 22, 24 and 25):

$$R_{stoich} = \frac{4X_{CH_4}\dot{m}_{Sweep}}{X_{O_2}\,2.56\times10^{-7}} \tag{26}$$

The final relation for R shows that it is a function of the sweep gas flow rate, the swept CH_4 mass fraction, and the fed O_2 mass fraction. Figure 42 illustrates the relation between R and the sweep gas flow rate at (0.525 fed O2 mass fraction and 0.1 swept CH4 mass fraction). This linear relation shows how the area ratio will increase as increasing the sweep flow rate (Figure 42). As the sweep flow rate increase the stoichiometric feed

flow rate will increase, this will require more polymer membrane and increase the area ratio (R).

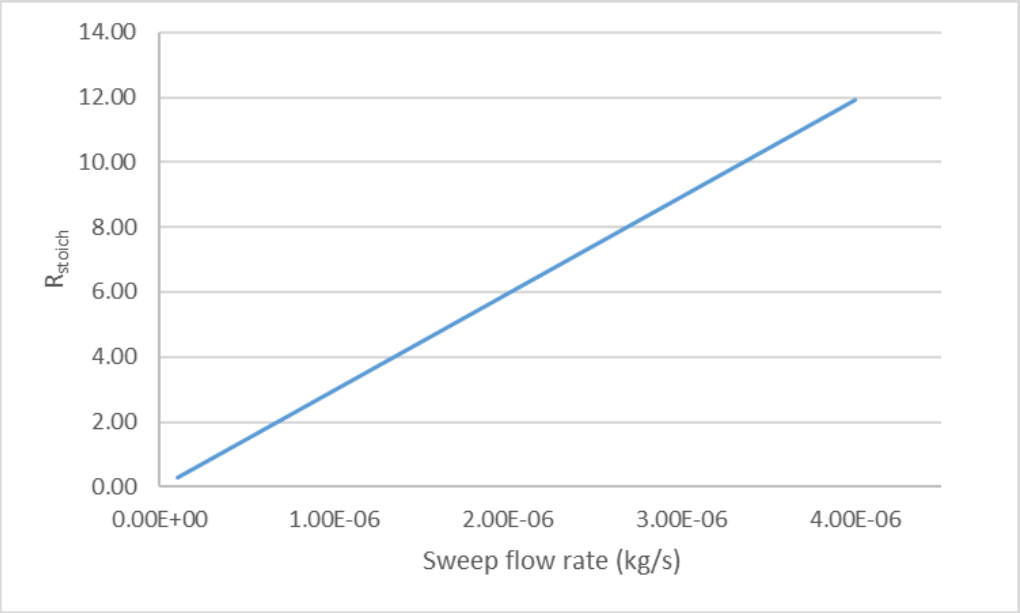

Figure 42: The relation between R and the sweep flow rate at (0.525 fed O_2 mass fraction, 0.1 swept CH_4 mass fraction, and $\phi = 1.0$)

Regarding the energy analysis, the power output per 0.35 thermal efficiency and including the preheat requirements could be calculated as following:

$$Power\ output = 0.35 HV_{CH_4} \dot{m}_{CH_4} - preheat\_load \quad (27)$$

Where: HV_{CH4} is the methane heat of combustion = 55.688 MJ/kg

Moreover, the required power to heat the feed and the sweep streams could be calculated as following:

$$preheat\_load = \Delta T\,(\dot{m}_{CH_4} c_{p,CH_4} + \dot{m}_{O_2} c_{p,O_2} + \dot{m}_{N_2} c_{p,N_2} + \dot{m}_{CO_2} c_{p,CO_2}) \quad (28)$$

Where (ΔT= 1123 K– 673 K = 450 K), and the specific heat (c_p) have been taken at the average temperature (900K). The preheat load is the required power to heat the sweep and the feed streams from 673 K to the inlet streams operation temperatures (1123 K). 673 K is the temperature of the preheated streams (feed and sweep streams) at the inlet of the second preheating stage; where the first stage is a heating recovery from the exhaust of this system, and it will rise the temperature of the sweep and feed streams from the ambient temperature to 673 K.

All species flow rates can be stated by the sweep flow rate ($\dot{m}_{sweep}$), where O_2 and N_2 will be expressed by the stoichiometric feed flow rate firstly then by the sweep flow rate (equation 22). So, the power outlet of this system could be expressed as function of the sweep flow rate, the fed O_2 mass fraction, and the swept CH_4 mass fraction as following:

$$Power\ \ output = \dot{m}_{sweep}\left[0.35HV_{CH_4}X_{CH_4} - \Delta T\left(X_{CH_4}c_{p,CH_4} + (1-X_{CH_4})c_{p,CO_2} + c_{p,N_2}\frac{4(1-X_{O_2})X_{CH_4}}{X_{O_2}} + 4X_{CH_4}c_{p,O_2}\right)\right] \quad (29)$$

Using this equation, the power output of this system (one OTM) could be calculated for known sweep flow rate, fed O_2 mass fraction, and swept CH_4 mass. Linear relation between the power output and (the sweep flow rate, and the swept CH_4 mass fraction) could be observed, while the non-linear relation between the power output and the fed O_2 mass fraction could be observed.

Therefore, the power output, the preheat load, and the stoichiometric feed flow rate, have been calculated for both oxygen enriched air case and for the atmospheric air case at (1.5×10^{-6} kg/s sweep flow rate with 0.1 swept CH_4 mass fraction) as shown in Table 8.

Table 8: Simulation inputs and outputs for both oxygen enriched air case and the atmospheric air case for one OTR based on (1.5×10^{-6} kg/s sweep flow rate with 0.1 swept CH_4 mass fraction, and $\phi = 1.0$).

Fed O_2 mass fraction	Stoichiometric feed flow rate (kg/s)	Number of fiber polymers	R_{stoich}	Preheat load (W)	$0.35HV_{CH_4}\dot{m}_{CH_4}$ (W)	Power output (W)
0.525	1.14×10^{-6}	44.6	4.46	1.59	2.92	1.33
0.233	2.58×10^{-6}	-	-	2.33	2.92	0.59

From this table, using the oxygen enriched air as the feed gas enhance the power output by raising it from 0.59 W to 1.33 W, that achieved by reducing the preheat load that will increase the power output. Figure 43 shows the sweep flow rate effect on the power output of one OTM for both 0.525 and 0.233 fed O_2 mass fractions. The linear relation in previous equation (29) appears in this figure. Higher values of the power outputs could be observed from this figure for oxygen enriched case; 2.255 ratio of the power outputs (0.525 fed O_2 mass fraction power output / 0.233 fed O_2 mass fraction power output) is remained constant with increasing the sweep flow rate.

The effect of the fed O_2 mass fraction could be observed by plotting the relation between it and the Power output (Figure 44). This figure shows the nonlinear relation between the fed O_2 mass fraction; this nonlinear relation was expected from equation (29). The increase of the power output would indicate to use the higher possible fed O_2 mass fraction. Figure 45 shows the linear relation between the swept CH_4 mass fraction and the power output. The increase of the swept CH_4 mass fraction will increase the power output. The power enhancement of using 0.525 fed O_2 mass fraction instead of 0.233 fed O_2 mass fraction (atmospheric air) is more than 1.5 ratio along the different swept CH_4

mass fractions. The limitation of using higher CH_4 mass fraction is the higher temperature associated with rising CH_4 concentrations.

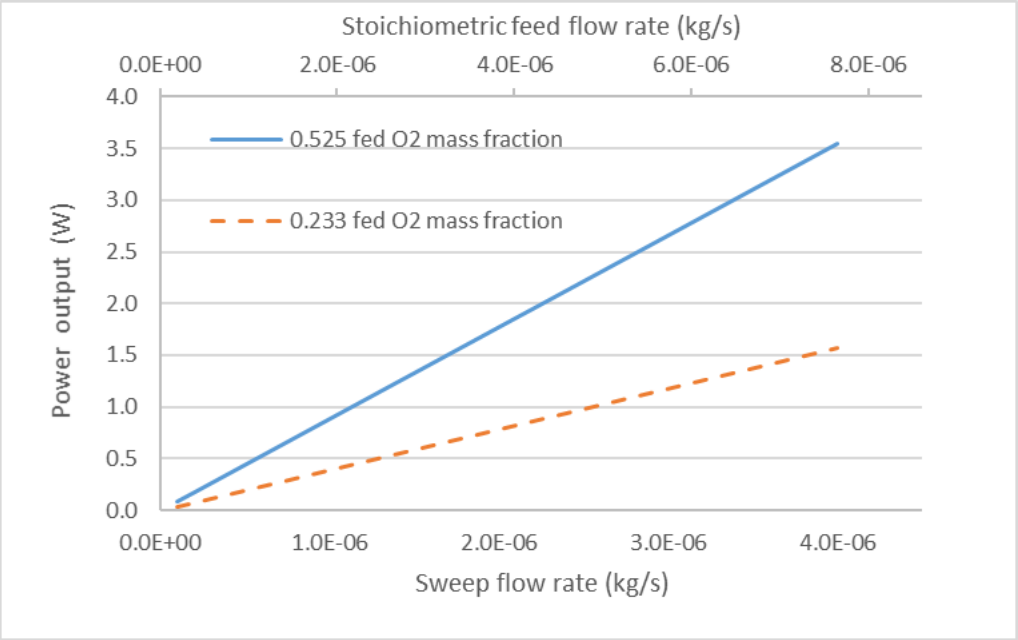

Figure 43: The sweep flow rate effect on the power output of one OTR at (0.1 swept CH_4 mass fraction, and $\phi = 1.0$).

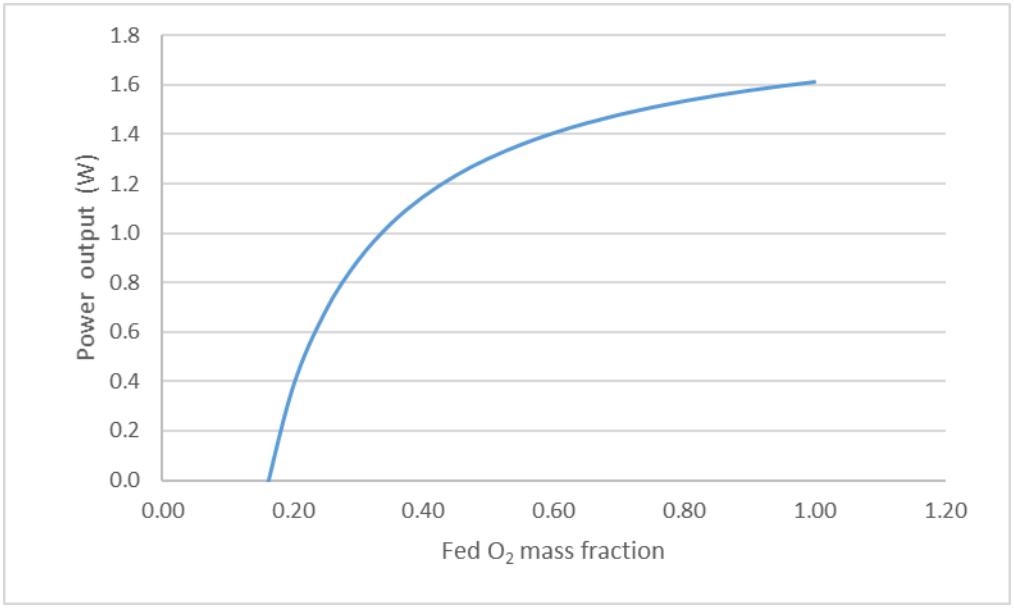

Figure 44: The effect of the fed O_2 mass fraction on the power output of one OTR at (1.5×10^{-6} kg/s sweep flow rate and 0.1 swept CH_4 mass fraction, and $\phi = 1.0$).

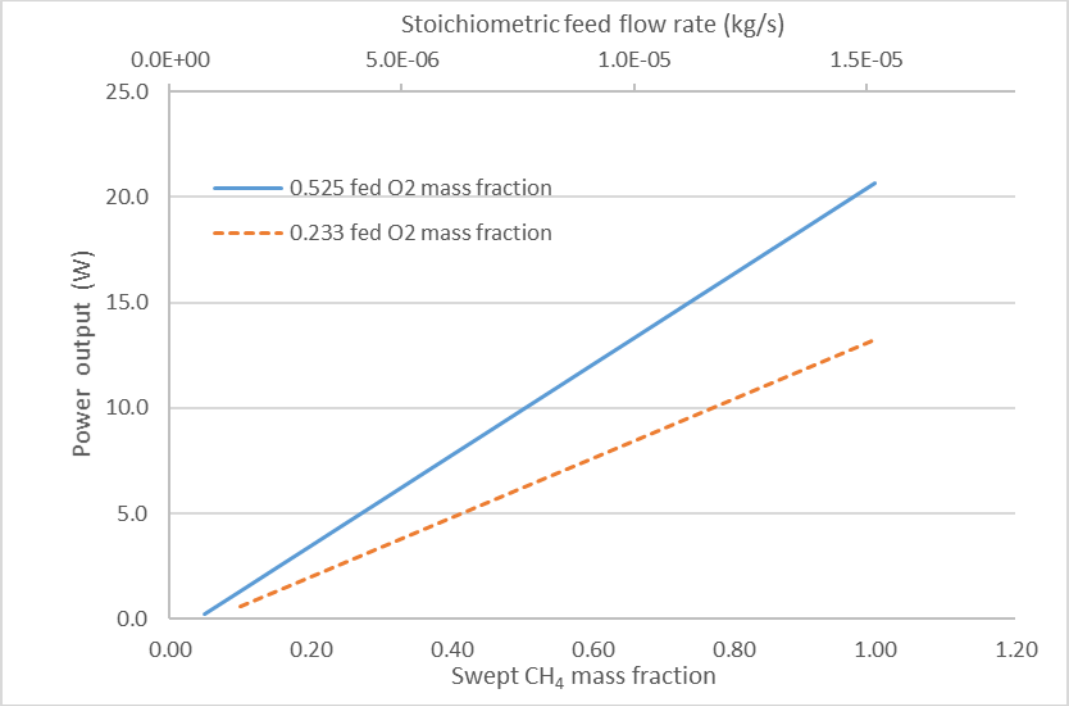

Figure 45: The effect of the swept CH_4 mass fraction on the power output of one OTR at (1.5×10^{-6} kg/s sweep flow rate, and ϕ = 1.0).

A proposed hybrid system is conducted to brief the inputs and outputs of this scheme. The case of (1.5×10^{-6} kg/s sweep flow rate with 0.1 swept CH4 mass fraction, 1.14×10^{-6} kg/s stoichiometric feed flow rate with 0.525 fed O_2 mass fraction, 1123 K streams inlet temperatures, and ϕ = 1.0) was considered in this design due to its highest possible consumed fuel per unit and its acceptable operating temperature. The contours of temperature and species mass fraction for this case are shown in Figure 46. Credible temperature could be observed in this case, the lower inlet temperature of the sweep and feed streams (1123 K) and the lower CH_4 flow rate distribute the flame along the membrane length, that will reduce the membrane temperature and distribute the oxygen flux along the membrane, as shown in Figure 47. While the contours of O_2 and CH_4 shows the gradual permeation of O_2 to the sweep side that causes to slow down the fuel

consumption (Figure 46, b and c). The feed inlet of this case have been extended 5 mm downstream to make sure that the high gradient at the inlet will not affect the feed combustion.

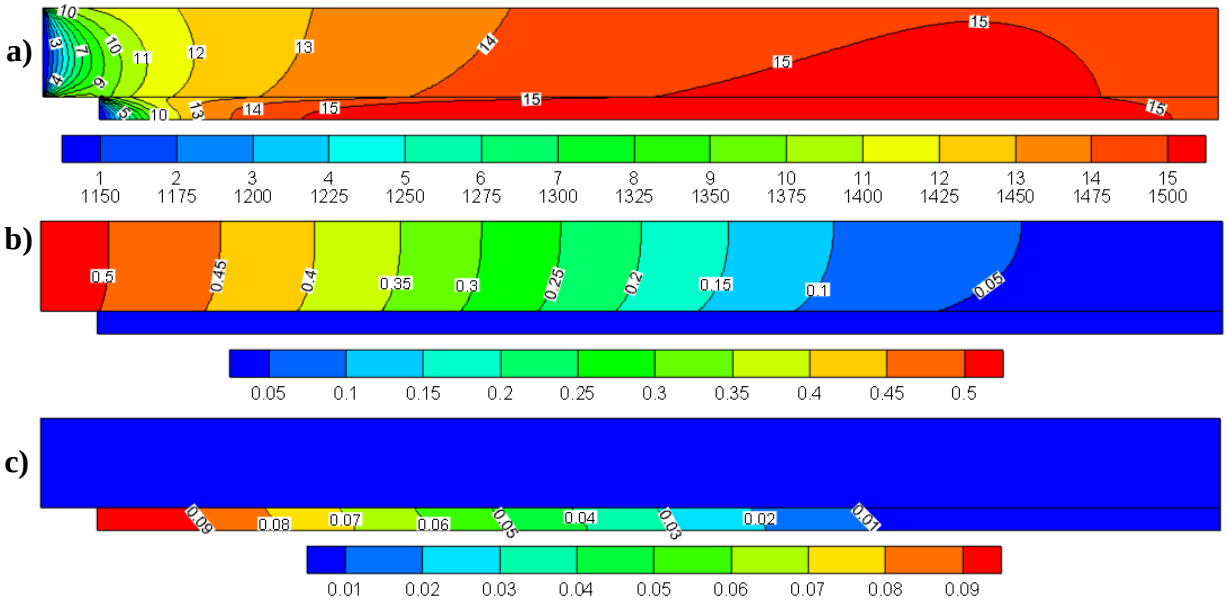

Figure 46: Contours of: a). Temperature (K), b). O_2 mass fraction, c). CH_4 mass fraction, at (1.14×10^{-6} kg/s feed flow rate with 0.525 O_2 mass fraction, 1.5×10^{-6} kg/s sweep flow rate with 0.1 CH_4 mass fraction, and ϕ = 1.0).

Inputs and outputs for the case at Table 7 were considered for the fiber polymer membrane in the hybrid system. The geometry of the fiber polymeric membrane and the OTM in Figures 6 and 10 respectively were taken up at this suggested design. 29 OTM's are proposed to be collected at one shell, while 325 fiber polymer membranes are suggested to be at one shell [40]. The outputs of a single OTM shell system is illustrated in Table 9. A schematic diagram could brief the expected configuration of the suggested hybrid polymer/ceramic oxy-fuel combustor system (Figure 48). This figure shows the inputs and the outputs of the designed hybrid system, and it shows a cross sectional view of the OTM shell, the diameter of the was calculated based on the simulated shell size.

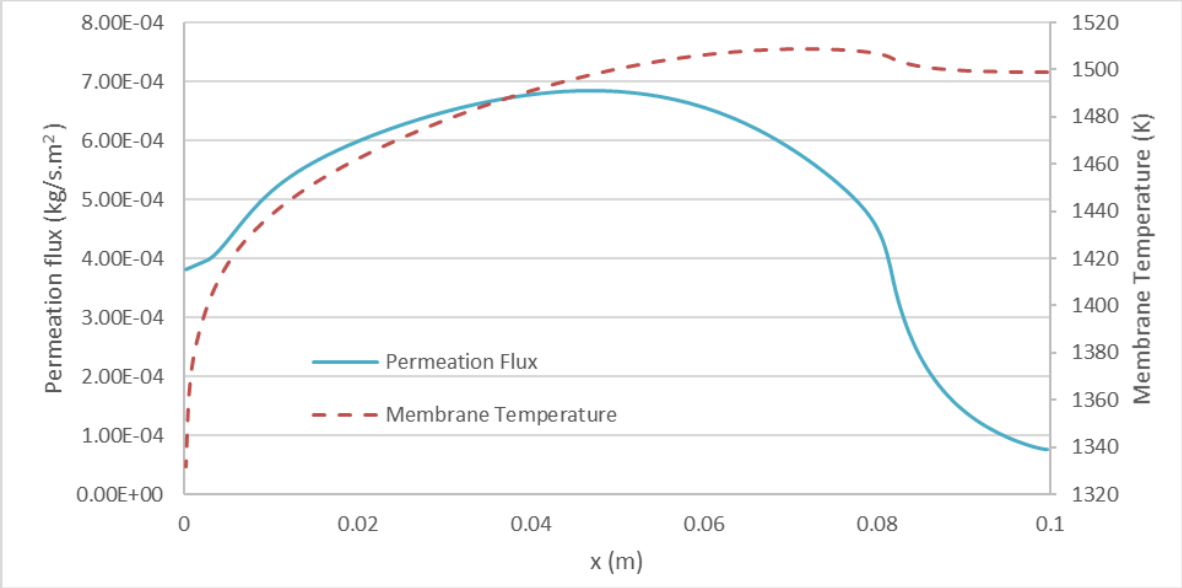

Figure 47: Permeation flux along the membrane length and membrane temperature for the proposed design case At (1.14×10^{-6} kg/s feed flow rate with 0.525 O_2 mass fraction, 1.5×10^{-6} kg/s sweep flow rate with 0.1 CH_4 mass fraction, and ϕ = 1.0).

Table 9: Proposed single OTM shell and its requirements and power.

Number of OTM's per shell	Number of fiber polymers	Number of fiber polymers per polymer shell	Number of fiber polymeric shells	Power output (W)
29	1300	325	4	38.57

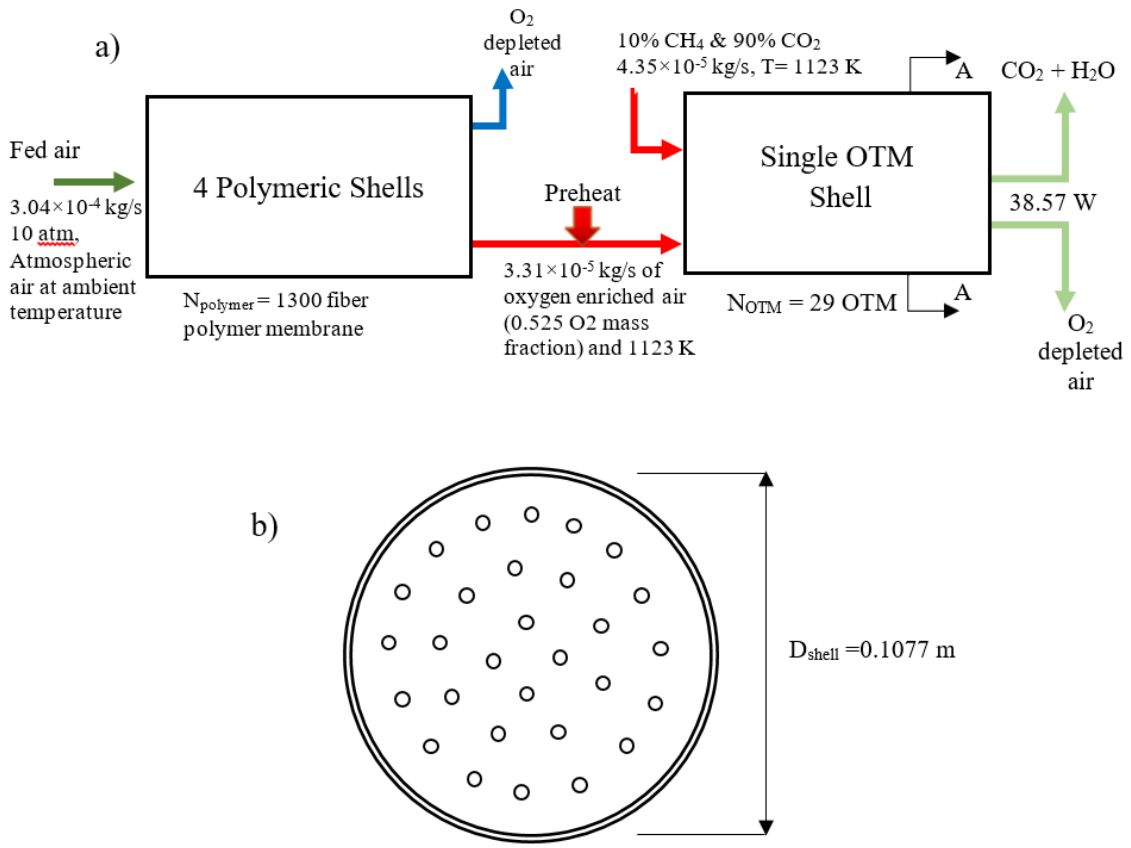

Figure 48: a) Schematic diagram of the proposed hybrid system configuration, b) Side view at section (A-A).

The species mass fractions along the OTM for this case are shown in Figure 49. CH_4 is consumed totally in the stoichiometric conditions. A slight amount of O_2 is observed at the sweep and feed outlet, due to the little higher feed flow rate above the stoichiometric flow rate (ϕ=1.00013), so, one can say this is a stoichiometric case. CO_2 mass fraction decreases with the combustion, due to the increase in the H_2O mass fraction, but still the mass flow rate of CO_2 increases (as the sweep flow rate increases due to the oxygen permeation). N_2 mass fraction at the feed side increases because of the oxygen permeation that causes a reduction of O_2 mass fraction on the feed side. The growth O_2 mass fraction at x=0.08 m is attributed to the terminated reaction while still the

permeation of the oxygen is continuous from the feed side. Table 9 shows feed and sweep outlets compositions and flow rates. The high N_2 mass fraction at the feed outlet could be observed; that can be used to produce higher N_2 purity. Sweep flow rate outlet records an increase while feed flow rate decreased due to the high permeation from the feed side to the sweep side. Regarding the flow rates outlets, both sweep and feed streams outlets should be used to produce the required power, but without any mixing.

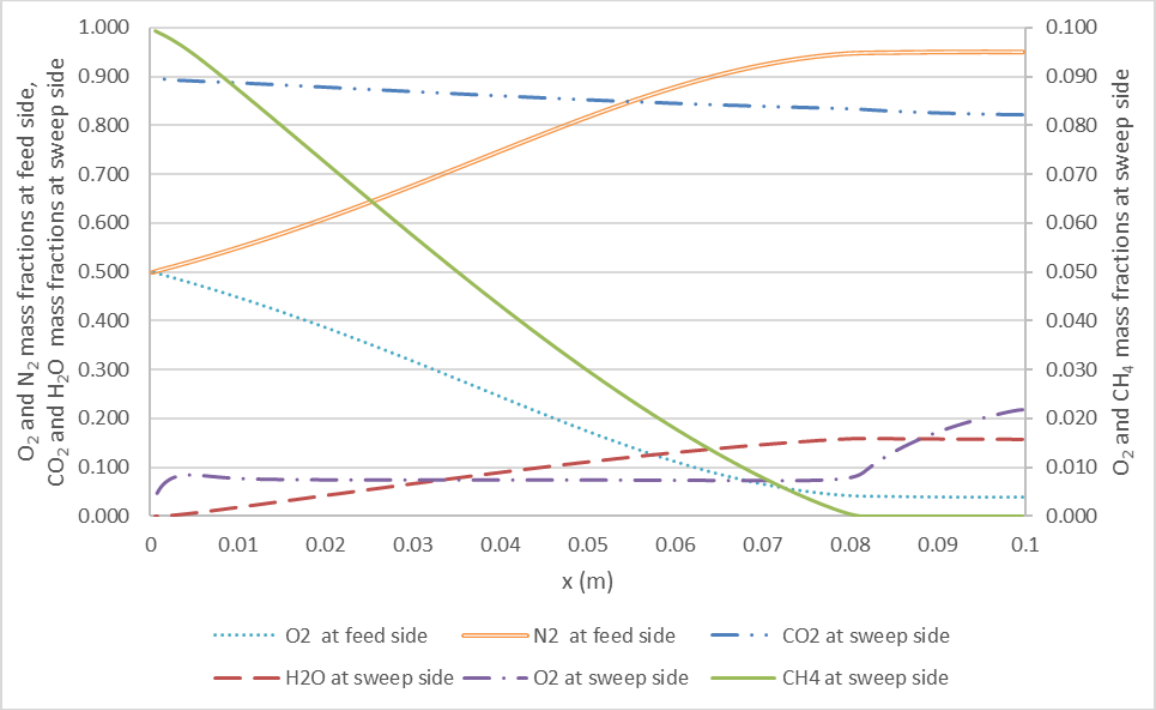

Figure 49: Distributions of species mass fractions at sweep and feed sides along the OTR length. At (1.14×10^{-6} kg/s feed flow rate with 0.525 O_2 mass fraction, 1.5×10^{-6} kg/s sweep flow rate with 0.1 CH_4 mass fraction, and ϕ = 1.0).

Table 10: Feed and sweep outlets compositions and flow rates for the proposed design case.

CH_4 at sweep outlet	O_2 at sweep outlet	H_2O at sweep outlet	CO_2 at sweep outlet	O_2 at feed outlet	N_2 at feed outlet	Sweep outlet flow rate (kg/s)	Feed outlet flow rate (kg/s)
Zero	0.022	0.157	0.821	0.038	0.949	2.151×10^{-6}	4.923×10^{-7}

CHAPTER 5

CONCLUSIONS AND RECOMMENDATIONS

5.1 Polymeric Membrane

A numerical study has been performed on the characteristics of air separation using polymeric membranes to be the first stage of developing a hybrid polymeric/ceramic membrane unit. An asymmetric hollow fiber polymeric membrane unit has been utilized. Gambit software was used to develop the mesh to be introduced to the Fluent software. User defined functions (UDFs) were coupled and hooked to the Fluent 12.1 software to account for the transfer of O_2 and N_2 across the membrane. Grid independence study has been performed to exclude the effect of cell size on calculated results. The model has been validated against the available experimental data in the literature.

Effects of the sweep and the feed gas flow rates on permeation fluxes and concentrations of O_2 and N_2 have been investigated. The results showed significant improvements in O_2 and N_2 permeation fluxes while increasing the sweep flow rate from zero up to 5.74×10^{-8} kg/s, and any further increase in sweep flow rate resulted in insignificant increase in permeation fluxes. Increasing the feed gas flow rate at zero sweep flow rate resulted in increase in O_2 permeation flux and reduction in N_2 permeation flux due to the changes in their partial pressure distributions in feed side associated with flow field modifications

due to the increase in feed flow rate. Approximately linear relations between feed pressure and O_2 and N_2 permeation fluxes have been reported.

Different polymer types including TR- PBO-co-PPL 28 and TR- PI-g-CD 450 have been considered to show the effect of membrane material on O_2 and N_2 permeation fluxes. Due to its high selectivity and lower permeability, the highest O_2 mass fraction at permeate outlet and the lowest permeation flow rate are obtained by the TR- PBO-co-PPL 28 membrane. Multi-stage gas separation has been investigated targeting higher O_2 concentrations at permeate outlet. Higher stage cut ratio is gained in the third stage as compared to preceding stages because of the higher permeation flow rate relative to the feed flow. The obtained O_2 mass concentrations at permeate outlets of first, second and third stages are 0.517, 0.8 and 0.914. Higher O_2 flux at higher outlet concentrations can be obtained by recycling the retentate flows of the third and second stages to the feed side in the first stage as those retentate flows have higher O_2 mass fractions than normal air introduced in the first stage.

5.2 Hybrid System

Ceramic oxygen transport reactor (OTR) has been integrated numerically with the polymeric membrane to form the hybrid polymeric/ceramic membrane unit for oxy-fuel combustion. A tubular oxygen transport membrane (OTM) has been utilized to perform the numerical simulations of the oxy-fuel combustion. Gambit software was used to prepare the mesh to be introduced to the Fluent software. User defined function (UDF) was coupled and hooked to the Fluent 16.1 software to account for the transfer of O_2 across the membrane. Grid independence study has been performed to exclude the effect

of cell size on calculated results. The model has been validated against the available experimental data in the literature.

The numerical results of the polymeric membrane have been utilized as inputs to the OTR unit. Stoichiometric feed flow rate has been defined to perform stoichiometric oxy-fuel combustion process without any excess of oxygen at the sweep outlet. Effect of the fed O_2 mass fraction have been studied, higher membrane temperature and flux were observed with increasing the fed O_2 mass fraction. It is noted that higher feed flow rate of the ambient air fed case (comparing with the oxygen enriched air case) is required to achieve stoichiometric oxy-fuel combustion with the same fuel flow rates. The effect of the swept CH_4 mass fraction has been investigated, higher temperatures and permeations were recorded as the swept CH_4 mass fraction increases.

Effects of the sweep and the feed gas flow rates on permeation flux, species concentrations, and the OTM temperature have been investigated. The results showed a significant rise in O_2 permeation flux, and OTM temperature while increasing the sweep flow rate from 8.0×10^{-8} kg/s up to 8.0×10^{-7} kg/s. Higher sweep flow rate could be utilized with the lower swept CH_4 mass fraction to procure similar permeation of the higher swept CH_4 mass fraction. Increasing the feed flow rate resulted in a decrease in O_2 permeation flux and membrane temperature, at a further increase in the feed flow rate, incomplete combustion and sharply reduction in the total permeation were reported. The number of the required polymer membranes to feed an OTM and ratio between the required fiber polymer membranes area to the OTM's area have been related to the stoichiometric feed flow rate.

The power output of the hybrid system has been calculated for one OTM fed by 45 fiber polymer membranes at stoichiometric conditions. The results have been compared with ambient air fed case, 1.33 W power output from the hybrid single OTM unit was reported while 0.59 W power output was gained from the ambient air fed unit. The enhancement of using the hybrid system have been investigated at different operation conditions, an enhancement ratio of 2.255 of the power output was observed (0.525 fed O_2 mass fraction power output / 0.233 fed O_2 mass fraction power output) with varying the sweep flow rate and keeping the other variables constant. The effect of the fed O_2 mass fraction on the OTR power output was investigated; growing of the power output was reported with increasing the fed O_2 mass fraction. The main advantage of the using the hybrid system is realized; higher power output could be produced comparing with ambient air fed system by reducing the preheat load.

A proposed hybrid system design is conducted; 4 shells of the polymeric membranes have been connected to one OTM shell to produce 38.57 W power output at stoichiometric conditions; where one polymeric shell consists of 325 fiber polymeric membranes while the single OTM shell contains 29 OTM's. The species inside the OTM and at the outputs of the proposed hybrid system have been reported, highly depleted O_2 air was produced from both the polymeric and ceramic sections of this system, while CO_2 and H_2O were generated as the oxy-fuel combustion outlets.

5.3 Recommendations

- More experimental studies could be conducted to explore and correlate the effect of the pressure, temperature and species consternations on the polymeric and ceramic membranes gases permeation.
- Further research on ITM can still be conduct to improve oxygen permeation potential of ion transport membranes.
- Multi-step reaction can give a higher accuracy of the oxy-fuel combustion process.
- Additional calculations of the pumping power of the hybrid system and the conventional system could be included in the power calculations.
- The hybrid system could be tested experimentally, to investigate the high temperature combustion effects on the system.
- Parallel arrangement hybrid system could be studied; where the polymeric membrane permeates oxygen enriched air directly to the OTM in one package.
- The retentate flow power could be used to generate power or to help in other streams compression.

NOMENCLATURE

A	Membrane area (m^2)
B	Constant
c_p	heat capacity (J/kg.K)
D	Diffusion coefficient (m^2/s)
$D_{i,m}$	Diffusion coefficient of mixture species i (m^2/s)
D_V	Diffusion coefficient of oxygen vacancy
E	Activation energy (J/mol)
FFV	Fractional free volume
GPU	Gas permeation unit ($1x10^{-6}$ cm^3/cm^2.s.cmHg)
HV_{CH4}	Methane heat of combustion MJ/kg
I	Intensity (W/m^2)
ITM	Ion Transport Membrane
J	Permeation flux (mole/m^2 s)
k_f	Fluid thermal conductivity (W/m.K)
K_f	Forward reaction rate (cm $atm^{-0.5}sec^{-1}$)
K_r	Reverse reaction rate mol/cm^2sec
L	Membrane thickness (m)
LCF	$La_{0.9}Ca_{0.1}FeO_{3-\delta}$ membrane

$\dot{m}$	Flow rate (kg/s)
MW	Molecular waight (g/mol)
N	Number of the fiber polymer membranes required to fed one OTM
OTM	Oxygen Transport Membrane
OTR	Oxygen Transport Reactor
P	Permeability (barrer)
p	Pressure (atm)
p'	Partial pressure in the feed side (atm)
p''	Partial pressure in the permeate side (atm)
R	Ideal gas constant J/mol K, or polymer to OTM area ratio
$\vec{s}$	Direction vector
S_i	Source/sink term (kg/m^3.s)
SP	Separation factor
T	Temperature (K)
TR	Thermally rearranged
TR- PBO-co-PPL-28	Thermally rearranged poly (benzoxazole-co-pyrrolone)
TR- PI-g-CD-450	Thermally rearranged cross-linkable polyimides grafted with thermal liable side beta-cyclodextrin (CD)
U	Velocity (m/s)
V	Measured volume (m^3)
V_0	Dense volume (m^3)

V_{cell}	Volume of cell (m)
X_i	Mass fraction of species *i*
y_i	Mole fraction of species *i*
α	Selectivity
ϕ	Equivalence ratio
μ	Dynamic viscosity (N.s/m^2)
ρ	Density (kg/m^3)
σ	Stefan-Boltzmann constant (W/m^{2}K^{-4})
Θ	Stage cut
$_{stoich}$	Stoichiometric conditions

REFERENCES

[1] Abdulhameed MA, Othman MHD, Ismail AF, Matsuura T, Harun Z, Rahman MA, Puteh MH, Jaafar J, Rezaei M, Hubadillah SK, "Carbon dioxide capture using a superhydrophobic ceramic hollow fiber membrane for gas-liquid contacting process.," *Journal of Cleaner Product,* vol. 140, pp. 1731-1738, 2017.

[2] Rajab Khalilpour, Kathryn Mumford, Haibo Zhai, Ali Abbas, Geoff Stevens, Edward S. Rubin, "Membrane-based carbon capture from flue gas: a review," *Journal of Cleaner Production,* vol. 103, pp. 286-300, 2015.

[3] Z. Z, "Comparisons of various absorbent effects on carbon dioxide capture in membrane gas absorption (MGA) process," *Journal of Natural Gas Science and Engineering,* pp. 589-595, 2016.

[4] Barba FC, Sánchez GM, Seguí BS, Darabkhani HG, Anthony EJ, "A technical evaluation, performance analysis and risk assessment of multiple novel oxy-turbine power cycles with complete CO2 capture.," *Journal of Cleaner Production* , vol. 133, pp. 971-985, 2016.

[5] Metz, B., Davidson, O., De Coninck, H., Loos, L., and Meyer, L., Carbon dioxide capture and storage, 2005.

[6] Anheden, M., Yan, J. and De Smedt, G., "Denitrogenation (or oxyfuel concepts," *Oil & gas science and technology 60.3,* pp. 485-495, 2005.

[7] Smith, A.R. and Klosek, J., "A review of air separation technologies and their integration with energy conversion processes," *Fuel Processing Technology 70.2,* pp. 115-134, 2011.

[8] Augelletti R, Conti M, Annesini MC, "Pressure swing adsorption for biogas upgrading. A new process configuration for the separation of biomethane and carbon dioxide.," *Journal of Cleaner Production ,* vol. 140, pp. 1390-1398, 2017.

[9] Matteucci, S., Yampolskii, Y., Freeman, B.D. and Pinnau, I., "Transport of gases and vapors in glassy and rubbery polymers," in *Materials science of membranes for gas and vapor separation,* 2006.

[10] Park, J. Y., and D. R. Paul, "Correlation and prediction of gas permeability in glassy polymer membrane materials via a modified free volume based group contribution method," *Journal of Membrane Science,* 1997.

[11] Maeda, Y., and D. R. Paul, "Effect of antiplasticization on selectivity and productivity of gas separation membranes," *Journal of membrane science,* 1987.

[12] Robeson, L.M., "The upper bound revisited," *Journal of Membrane Science,* 2008.

[13] Gambini, M. and Vellini, M., "Oxygen Transport Membranes for Ultra-Supercritical (USC) Power Plants With Very Low CO2 Emissions," *Journal of Engineering for*

Gas Turbines and Power, 2012.

[14] Xu, S.J. and Thomson, W.J, "Oxygen permeation rates through ion-conducting perovskite membranes," *Chemical Engineering Science,* vol. 54(17), pp. 3839-3850, 1999.

[15] Habib, M. A., Ahmed, P., Ben-Mansour, R., Badr, H. M., Kirchen, P., & Ghoniem, A. F., "Modeling of a combined ion transport and porous membrane reactor for oxy-combustion," *Journal of membrane science,* vol. 446, pp. 230-243, 2013.

[16] Ghoniem, A.F., Mitsos, A., Shao-Horn, Y., Habib, M.A., Mezghani, K. and Ben-Mansour, R., "Integrated polymeric-ceramic membrane based oxy-fuel combustor". U.S. Patent 9,004,909, 14 Aprol 2015.

[17] Simpson, A.P. and Simon, A.J., "Second law comparison of oxy-fuel combustion and post-combustion carbon dioxide separation," *Energy Conversion and Management*, 2007.

[18] Burdyny, T. and Struchtrup, H., "Hybrid membrane/cryogenic separation of oxygen from air for use in the oxy-fuel process," *Energy 35.5*, pp. 1884-1897, 2010.

[19] Pfaff, I. and Kather, A., "Comparative thermodynamic analysis and integration issues of CCS steam power plants based on oxy-combustion with cryogenic or membrane based air separation," *Energy Procedia*, 2009.

[20] Yörük, C.R., Meriste, T., Trikkel, A. and Kuusik, R., "Oxy-fuel Combustion of

Estonian Oil Shale: Kinetics and Modeling," *Energy Procedia*, 2016.

[21] Gao, Y., Tahmasebi, A., Dou, J. and Yu, J., "Combustion characteristics and air pollutant formation during oxy-fuel co-combustion of microalgae and lignite," *Bioresource technology*, 2016.

[22] Niu, S., Chen, M., Li, Y. and Xue, F., "Evaluation on the oxy-fuel combustion behavior of dried sewage sludge," *Fuel*, 2016.

[23] Chen, L., Yong, S.Z. and Ghoniem, A.F., "Oxy-fuel combustion of pulverized coal: Characterization, fundamentals, stabilization and CFD modeling," *Progress in Energy and Combustion Science*, 2012.

[24] Habib, M. A., Badr, H. M., Ahmed, S. F., Ben-Mansour, R., Mezghani, K., "A review of recent developments in carbon capture utilizing oxy-fuel combustion in conventional and ion transport membrane systems," *International Journal of Energy Research, 35(9)*, 2011.

[25] Mardani, A. and Ghomshi, A.F., "Numerical study of oxy-fuel MILD (moderate or intense low-oxygen," *Energy*, 2016.

[26] Bhuiyan, A.A. and Naser, J., "CFD modelling of co-firing of biomass with coal under oxy-fuel combustion in a large scale power plant," *Fuel*, 2015.

[27] Adamczyk, W.P., Kozołub, P., Klimanek, A., Białecki, R.A., Andrzejczyk, M. and Klajny, M., "Numerical simulations of the industrial circulating fluidized bed boiler

under air-and oxy-fuel combustion," *Applied Thermal Engineering,* 2015.

[28] Kutne P, Kapadia BK, Meier W, Aigner M, "Experimental analysis of the combustion behaviour of oxyfuel flames in a gas turbine model combustor," *Proceedings of the Combustion Institute,* vol. 33(2), pp. 3383-3390, 2011.

[29] Nemitallah MA, Habib MA, "Experimental and numerical investigations of an atmospheric diffusion oxy-combustion flame in a gas turbine model combustor," *Applied energy,* vol. 111, pp. 401-415, 2013.

[30] Liu CY, Chen G, Sipöcz N, Assadi M, Bai XS, "Characteristics of oxy-fuel combustion in gas turbines," *Applied Energy,* vol. 89(1), pp. 387-394, 2012.

[31] Park, H.B., Han, S.H., Jung, C.H., Lee, Y.M. and Hill, A.J., "Thermally rearranged (TR) polymer membranes for CO 2 separation," *Journal of Membrane Science,* 2010.

[32] Woo, K.T., Dong, G., Lee, J., Kim, J.S., Do, Y.S., Lee, W.H., Lee, H.S. and Lee, Y.M., "Ternary mixed-gas separation for flue gas CO 2 capture using high performance thermally rearranged (TR) hollow fiber membranes," *Journal of Membrane Science,* 2016.

[33] Liu, Q., Paul, D.R. and Freeman, B.D., "Gas permeation and mechanical properties of thermally rearranged (TR) copolyimides," *Polymer,* 2016.

[34] Jo, HJ., Soo, CY., Dong, G., Do, YS., Wang, HH., Lee, MJ., Quay, JR., Murphy, MK., Lee, YM., "Thermally Rearranged Poly (benzoxazole-co-imide) Membranes

with Superior Mechanical Strength for Gas Separation Obtained by Tuning Chain Rigidity.," *Macromolecules,* vol. 48(7), pp. 2194-2202, 2015.

[35] Calle, M., Lozano, A.E. and Lee, Y.M., "Formation of thermally rearranged (TR) polybenzoxazoles: Effect of synthesis routes and polymer form.," *European Polymer Journal,* 2012.

[36] Sanders, D.F., Smith, Z.P., Guo, R., Robeson, L.M., "Energy-efficient polymeric gas separation membranes for a sustainable future: A review," *Polymer,* vol. 54, pp. 4729-4761, 2013.

[37] Jiang, X. and Kumar, A, "Performance of silicone-coated polymeric membrane in separation of hydrocarbons and nitrogen mixtures," *Journal of membrane science 254.1,* pp. 179-188, 2005.

[38] Coombe, H.S. and Nieh, S., "Polymer membrane air separation performance for portable oxygen enriched combustion applications," *Energy Conversion and Management 48.5,* pp. 1499-1505, 2007.

[39] Alsari, A., Kruczek, B., & Matsuura, T., "Effect of pressure and membrane thickness on the permeability of gases in dense polyphenylene oxide (PPO) membranes: thermodynamic interpretation," *Separation Science and Technology,* vol. 42(10), pp. 2143-2155, 2007.

[40] Feng, X., Ivory, J., and Rajan, V.S, "Air separation by integrally asymmetric hollow-fiber membrane," *AIChE journal,* vol. 45.10, pp. 2142-2152, 1999.

[41] Dixon-Garrett, S.V., Nagai, K. and Freeman, B.D., "Sorption, Diffusion, and Permeation of Ethylbenzene in Poly(1-trimethylsilyl-1-propyne)," *Journal of Polymer Science,* vol. 38, p. 1078–1089, 2000.

[42] Ahmad, F., Lau, K.K., Shariff, A.M. and Murshid, G., "Process simulation and optimal design of membrane separation system for CO 2 capture from natural gas.," *Computers & Chemical Engineering,* pp. 119-128, 2012.

[43] Zhao, L., Riensche, E., Menzer, R., Blum, L. and Stolten, D., "A parametric study of CO 2/N 2 gas separation membrane processes for post-combustion capture," *Journal of membrane science,* vol. 325, pp. 284-294, 2008.

[44] Kawachale, N., Kumar, A. and Kirpalani, D., "Numerical investigation of hydrocarbon enrichment of process gas mixtures by permeation through polymeric membranes," *Chemical engineering& technology 31.1,* pp. 58-65, 2008.

[45] Binns, M., Lee, S., Yeo, Y.K., Lee, J.H., Moon, J.H., Yeo, J.G. and Kim, J.K., "Strategies for the simulation of multi-component hollow fibre multi-stage membrane gas separation systems," *Journal of Membrane Science,* 2016.

[46] Dong, G., Woo, K.T., Kim, J., Kim, J.S. and Lee, Y.M., "Simulation and feasibilitystudyofusingthermally rearranged polymeric hollow fiber membranes for various industrial gas separation applications," *Journal ofMembraneScience,* 2015.

[47] Zhang Z, Yan Y, Wood DA, Zhang W, Li L, Zhang L, and Van der Bruggen B, "Influence of the Membrane Module Geometry on SO2 Removal: A Numerical

Study.," *Industrial and engineering chemistry research* , vol. 54, pp. 11619-11627, 2015.

[48] Wook Choi, Pravin G. Ingole, Hui Li, Jong-Hak Kim, Hyung-Keun Lee, Il-Hyun Baek, "Preparation of facilitated transport hollow fiber membrane for gas separation using cobalt tetraphenylporphyrin complex as a coating material," *Journal of Cleaner Production* , vol. 133, pp. 1008-1016, 2016.

[49] "ANSYS® Academic Research," vol. Release 12.1..

[50] Wang, B., Song, J., Tan, X., Meng, B., Liu, J. and Liu, S., "Reinforced perovskite hollow fiber membranes with stainless steel as the reactive sintering aid for oxygen separation," *Journal of Membrane Science*, 2016.

[51] Islam, Q.A., Raja, M.W. and Basu, R.N., "La x Sr 1-x Co 0.35 Bi 0.2 Fe 0.45 O 3-δ (x= 0.5 to 0.8): A new series of oxygen separation membrane," *International Journal of Hydrogen Energy*, 2016.

[52] He, B., Ding, D., Ling, Y., Xu, J. and Zhao, L., "Efficient modification for enhancing surface activity of Ba 0.5 Sr 0.5 Co 0.8 Fe 0.2 O 3− δ oxygen permeation membrane," *Journal of Membrane Science*, 2015.

[53] Wang, R., Meng, B., Meng, X., Tan, X., Sunarso, J., Liu, L. and Liu, S., "Highly stable La 0.6 Sr 0.4 Co 0.2 Fe 0.8 O 3− δ hollow fibre membrane for air separation swept by steam or steam mixture," *Journal of Membrane Science*, 2015.

[54] Chen, W., Chen, C.S., Bouwmeester, H.J., Nijmeijer, A. and Winnubst, L., "Oxygen-selective membranes integrated with oxy-fuel combustion," *Journal of membrane science*, 2014.

[55] Wang, Z., Kathiraser, Y., Soh, T. and Kawi, S., "Ultra-high oxygen permeable BaBiCoNb hollow fiber membranes and their stability under pure CH 4 atmosphere," *Journal of Membrane Science*, 2014.

[56] Wang, H., Kölsch, P., Schiestel, T., Tablet, C., Werth, S. and Caro, J, "Production of high-purity oxygen by perovskite hollow fiber membranes swept with steam," *Journal of membrane science*, 2006.

[57] Kirchen, P., Apo, D.J., Hunt, A. and Ghoniem, A.F, "A novel ion transport membrane reactor for fundamental investigations of oxygen permeation and oxy-combustion under reactive flow conditions," *Proceedings of the Combustion Institute*, 2012.

[58] Yantovski, E., Gorski, J., Smyth, B., & Ten Elshof, J, "Zero-emission fuel-fired power plants with ion transport membrane," *Energy, 29(12)*, pp. 2077-2088, 2004.

[59] Chen, W., van der Ham, L., Nijmeijer, A. and Winnubst, L.,, "Membrane-integrated oxy-fuel combustion of coal: Process design and simulation," *Journal of membrane science*, 2015.

[60] Habib, M.A., Salaudeen, S.A., Nemitallah, M.A., Ben-Mansour, R. and Mokheimer, E.M., "Numerical investigation of syngas oxy-combustion inside a LSCF-6428

oxygen transport membrane reactor," *Energy,* vol. 96, pp. 654-665, 2016.

[61] Hong, J., Kirchen, P. and Ghoniem, A.F., "Numerical simulation of ion transport membrane reactors: oxygen permeation and transport and fuel conversion," *Journal of membrane science,* vol. 407, pp. 71-85, 2012.

[62] Habib, M.A., Ahmed, P., Ben-Mansour, R., Mezghani, K., Alam, Z., Shao-Horn, Y. and Ghoniem, A.F., "Experimental and Numerical Investigation of La2NiO4 Membranes for Oxygen Separation: Geometry Optimization and Model Validation," *Journal of Energy Resources Technology*, 2015.

[63] Nemitallah, M.A., Habib, M.A. and Mansour, R.B., "Investigations of oxy-fuel combustion and oxygen permeation in an ITM reactor using a two-step oxy-combustion reaction kinetics model," *Journal of Membrane Science,* vol. 432, pp. 1-12, 2013.

[64] Ahmed, P., Habib, M.A., Ben-Mansour, R., Kirchen, P. and Ghoniem, A.F., "CFD (computational fluid dynamics) analysis of a novel reactor design using ion transport membranes for oxy-fuel combustion," *Energy*, 2014.

[65] Coroneo, M., Montante, G., Baschetti, M.G. and Paglianti, A., "CFD modelling of inorganic membrane modules for gas mixture separation," *Chemical Engineering Science,* 2009.

[66] Hong, J., Kirchen, P. and Ghoniem, A.F., "Laminar oxy-fuel diffusion flame supported by an oxygen-permeable-ion-transport membrane," *Combustion and*

Flame, 2013.

[67] Nemitallah, M.A., Habib, M.A. and Mansour, R.B, "Investigations of oxy-fuel combustion and oxygen permeation in an ITM reactor using a two-step oxy-combustion reaction kinetics model.," *Journal of membrane science,* vol. 432, pp. 1-12, 2013.

[68] Nemitallah, M.A., Habib, M.A., Ben-Mansour, R. and Ghoniem, A.F, "Design of an ion transport membrane reactor for gas turbine combustion application.," *Journal of membrane science,* vol. 450, pp. 60-71, 2014.

[69] Habib, M.A. and Nemitallah, M.A, "Design of an ion transport membrane reactor for application in fire tube boilers.," *Energy,* vol. 81, pp. 787-801, 2015.

[70] S. Patankar, Numerical heat transfer and fluid flow, Washington D.C : Hemisphere publishing corporation, 1980.

[71] Hunt A, Dimitrakopoulos G, Kirchen P, Ghoniem AF, "Measuring the oxygen profile and permeation flux across an ion transport (La0. 9Ca0. 1FeO3− δ) membrane and the development and validation of a multistep surface exchange model," *Journal of Membrane Science,* vol. 468, pp. 62-72, 2014.

[72] Tan X, Li K, "Modeling of air separation in a LSCF hollow-fiber membrane module," *AIChE journal,* vol. 48(7), pp. 1469-1477, 2002.

[73] Li, W., Liu, J.J. and Chen, C.S., "Hollow fiber membrane of yttrium-stabilized zirconia and strontium-doped lanthanum manganite dual-phase composite for

oxygen separation," *Journal of Membrane Science,* no. 2009, 2009.

[74] Choi, J.I., Jung, C.H., Han, S.H., Park, H.B. and Lee, Y.M., "Thermally rearranged (TR) poly (benzoxazole-co-pyrrolone) membranes tuned for high gas permeability and selectivity," *Journal of Membrane Science 349,* pp. 358-368, 2010.

[75] Xiao, Y. and Chung, T.S, "Grafting thermally labile molecules on cross-linkable polyimide to design membrane materials for natural gas purification and CO 2 capture," *Energy & Environmental Science,* vol. 4, 2011.

[76] Katoh, T., Tokumura, M., Yoshikawa, H. and Kawase, Y, "simulation of multicomponent gas separation by hollow-fiber membrane module: Nonideal mixing flows in permeate and residue sides using the tanks-in-series model," *Separation and purification technology,* no. 2011.

APPENDIX

To calculate the required units to generate as specific power, following example shows the required units to generate 1 MW power. The data in this table were used to calculate the required OTM's and polemics membranes, which have the known sweep flow rate and swept CH_4 mass fraction. Table 11 shows the results.

Table 11: The required OTM's and polemics membranes to produce 1.0MW power. At (1.14×10^{-6} kg/s feed flow rate with 0.525 O_2 mass fraction, 1.5×10^{-6} kg/s sweep flow rate with 0.1 CH_4 mass fraction, and ϕ = 1.0).

Power output (MW)	Number of OTM shells	Number of fiber polymeric shells	Air feed flow rate (kg/s)	Methane flow rate (kg/s)
1.0	25926.0	103707.0	7.92	0.1128

Vitae

Name : Dia’ Al-deen Omar Afaneh

Nationality : Jordanian

Date of Birth :11/28/1990

Email : Diaa.Afaneh@gmail.com

Address : Jarash, Jordan.

Academic Background :

- Master of Science in Mechanical Engineering, January 2017, King Fahd University of Petroleum and Minerals, Dhahran, Saudi Arabia.
- Bachelor’s in Mechanical Engineering, June 2012, The Hashemite University, Jordan.

Journal Publications and Conference Presentations:

- Habib MA, Nemitallah MA, Afaneh D, Mezghani K., "Characteristic of air separation in hollow-fiber polymeric membrane for oxygen enriched air clean combustion applications," *Journal of Cleaner Production*, vol. 143, pp. 960-972, 2017.